THE AERONAUTICAL QUARTERLY VOL. XII FEBRUARY 1961

THE AERONAUTICAL QUARTERLY

A Journal devoted to Aeronautics and the Allied Sciences

Volume XII FEBRUARY 1961 Part 1

CONTENTS

The Influence of Biaxial Mean Stresses on Failure of Tubes by Fatigue — *H. L Cox and N. B. Owen*

The Vibration of Air in a Duct with a Subsonic Mean Flow — *D. S. Whitehead*

The Effect of Fuel Distribution on Reaction Rates — *M. V. Herbert*

The Behaviour of a Clamped Circular Plate in Compression — *A. N. Sherbourne*

The Design of Wing Plan Forms for Transonic Speeds — *R. C. Lock*

Review of "Turbulent Flows and Heat Transfer," edited by C. C. Lin — *G. K. Batchelor*

LONDON

ROYAL AERONAUTICAL SOCIETY

4 HAMILTON PLACE W1

15/-

THE AERONAUTICAL QUARTERLY

Editorial Board

Dr. A. M. BALLANTYNE, T.D., B.Sc., Ph.D., F.R.Ae.S., Hon.F.C.A.I. F.I.A.S. (*Chairman*)

Mr. HAYNE CONSTANT, C.B., C.B.E., M.A., F.R.S., F.R.Ae.S.

Sir HAROLD ROXBEE COX, D.Sc., D.I.C., Ph.D., F.R.Ae.S., F.I.A.S.

Sir WILLIAM FARREN, C.B., M.B.E., M.A., D.Sc., F.R.S. Hon.F.R.Ae.S., Hon.F.I.A.S.

Sir ARNOLD HALL, M.A., F.R.S., F.R.Ae.S.

Sir ALFRED PUGSLEY, O.B.E., D.Sc., F.R.S., F.R.Ae.S.

Sir GEOFFREY TAYLOR, M.A., D.Sc., F.R.S., Hon.F.R.Ae.S.

Dr. P. B. WALKER, C.B.E., M.A., F.R.Ae.S.

Editor—E. C. PIKE, M.A., A.F.R.Ae.S.

Editorial Referees

Aerodynamics

(a) General

Sir LEONARD BAIRSTOW
Mr. D. KEITH-LUCAS
Prof. W. A. MAIR
Mr. L. F. NICHOLSON
Dr. R. C. PANKHURST
Mr. E. F. RELF
Prof. E. J. RICHARDS
Dr. B. THWAITES

(b) Fluid Motion

Dr. G. K. BATCHELOR
Mr. A. FAGE
Dr. D. W. HOLDER
Prof. L. HOWARTH
Dr. W. P. JONES
Dr. J. W. MACCOLL
Prof. J. H. PRESTON
Prof. H. B. SQUIRE
Prof. G. TEMPLE
Prof. G. N. WARD
Prof. A. D. YOUNG

(c) Stability and Control

Mr. L. W. BRYANT
Mr. S. B. GATES
Mr. G. H. LEE
Mr. M. B. MORGAN
Mr. H. H. B. M. THOMAS

Helicopters and Propellers

Prof. J. A. J. BENNETT
Mr. P. BRETT
Mr. L. G. FAIRHURST
Mr. R. HAFNER
Dr. G. S. HISLOP
Capt. R. N. LIPTROT

Instruments and Electrical Equipment

Dr. G. E. BAIRSTO
Sir GEORGE GARDNER
Dr. C. S. HUDSON
Mr. C. N. JAQUES
Mr. F. W. MEREDITH

Aircraft Design

Mr. R. BOORMAN
Mr. R. M. CLARKSON
Mr. A. N. CLIFTON
Mr. H. H. GARDNER
Mr. H. KNOWLER
Mr. F. H. POLLICUTT
Dr. A. E. RUSSELL
Mr. R. S. STAFFORD
Mr. W. H. STEPHENS

Radio and Radar

Mr. J. F. ATHERTON
Mr. B. G. GATES
Dr. R. L. SMITH ROSE
Dr. A. M. UTTLEY
Sir ROBERT WATSON-WATT

Aviation Medicine

Dr. K. G. BERGIN
Dr. A. BUCHANAN BARBOUR

Meteorology

Sir DAVID BRUNT
Mr. J. K. HARDY
Prof. P. A. SHEPPARD

Sound

Mr. W. MAKINSON
Mr. F. B. GREATREX
Mr. N. FLEMING

Aircraft Propulsion

Mr. A. D. BAXTER
Mr. A. V. CLEAVER
Sir A. H. ROY FEDDEN
Dr. S. HOOKER
Mr. A. R. HOWELL
Mr. W. H. LINDSEY
Mr. P. LLOYD
Prof. A. W. MORLEY
Dr. E. S. MOULT
Mr. N. S. MUIR
Mr. F. NIXON
Mr. F. M. OWNER
Mr. H. PEARSON
Mr. H. SAMMONS
Prof. O. A. SAUNDERS
Prof. A. G. SMITH

Air Transport

Mr. A. C. CAMPBELL ORDE
Mr. P. G. MASEFIELD
Mr. N. E. ROWE
Mr. B. S. SHENSTONE
Mr. W. TYE

Aircraft Accessories

Mr. A. E. BINGHAM
Mr. W. C. CLOTHIER
Mr. H. G. CONWAY
Sir GEORGE DOWTY
Mr. R. GRAHAM
Mr. C. D. HOLLAND

Performance

Mr. H. DAVIES
Mr. D. R. NEWMAN
Mr. A. H. YATES

Flight Testing

Mr. R. R. DUDDY
Mr. P. A. HUFTON
Mr. S. SCOTT HALL
Mr. H. L. STEVENS

Structures

Prof. J. H. ARGYRIS
Mr. A. J. BARRETT
Mr. A. C. BROWN
Mr. H. L. COX
Mr. D. J. FARRAR
Prof. W. S. HEMP
Prof. R. HILL
Mr. H. B. HOWARD
Col. H. T. JESSOP
Mr. E. D. KEEN
Mr. F. A. KERRY
Dr. D. M. A. LEGGETT
Mr. R. L. LICKLEY
Prof. A. J. SUTTON PIPPARD
Prof. S. C. REDSHAW
Mr. R. H. SANDIFER
Sir RICHARD SOUTHWELL

Fuels and Oils

Mr. E. L. BASS
Dr. J. W. DRINKWATER
Prof. F. H. GARNER
Prof. W. E. GARNER
Dr. K. E. W. RIDLER
Dr. C. G. WILLIAMS

Materials

Dr. L. AITCHISON
Dr. N. P. ALLEN
Mr. G. FORREST
Prof. N. F. MOTT
Mr. L. ROTHERHAM
Dr. H. SUTTON
Dr. C. SYKES

Vibration and Flutter

Mr. E. G. BROADBENT
Prof. A. R. COLLAR
Mr. H. TEMPLETON
Mr. M. O. W. WOLFE

The Influence of Biaxial Mean Stresses on the Failure of Tubes by Fatigue

H. L. COX, M.A., F.R.Ae.S., A.M.I.Mech.E. and N. B. OWEN, A.M.I.Mech.E.

(*National Physical Laboratory*)

SUMMARY: Thin-walled tubes, $\frac{5}{8}$ in. in diameter, of three hard aluminium alloys and of mild steel have been tested in fatigue under three systems of alternating stresses while subjected to biaxial mean tensions imposed by means of internal pressure. In fatigue under direct or bending stresses the hoop tension in the walls of the aluminium alloy tubes did not seriously reduce the fatigue endurance, but it did markedly affect the mode and rate of crack propagation; cracks initially transverse to the tube axis tended to develop very rapidly in the axial direction. This tendency was present under both fluid and gas pressure, and under gas pressure the cracks propagated so fast that the test piece was often blown to pieces before the gas pressure fell by leakage through the cracks. The gradual taper in wall thickness along the fillets joining the test section to the enlarged ends offered no barrier to propagation of the axial cracks and the whole test piece, including its enlarged ends, was often shattered. Propagation of the axial cracks was preventible by sufficiently reducing the fillet radius, or by a ring glued on. Under alternating torsion, both endurance and mode of failure were affected by internal gas pressure. The initial fatigue crack, either circumferential or axial, often extended over a length comparable with the diameter of the tube, except under low ranges of shear stress when the crack length was sometimes very short. At each end the cracks forked in a characteristic manner and under moderate gas pressure the portions of the wall between the prongs of the fork were blown outwards. Under high pressure explosive failure and fragmentation often occurred. Mild steel under alternating torsion with internal gas pressure exhibited the same modes of failure, and two or more fatigue cracks were often formed simultaneously. Under high hoop tension, cracks propagated rapidly and one test piece, after two million cycles endurance, failed by exploding. However, no mild steel test piece was fragmented. A tentative explanation is offered of the reason why, in tubes of small diameter, rather short fatigue cracks may be expected to lead to fast fracture under the static loading. Attention is drawn to the inference that the initial fatigue crack itself must develop very quickly to considerable length.

1. Introduction

An investigation has been made into the effect of biaxial mean stress on failure by fatigue.

Test pieces were made in the form of tubes, of $\frac{5}{8}$ in. diameter and 0·015 in. wall thickness, and the first tests were made under static hoop tension, imposed by internal

Received September 1960.

[The Aeronautical Quarterly, Vol. XII, February 1961]

pressure, and pulsating axial tension. The axial loading was imposed by means of the N.P.L. 1500 lb. Slipping Clutch Fatigue Machine, the mean loading being set to half the range imposed, diminished by the axial loading due to the internal pressure. For convenience the internal pressure was obtained from a cylinder of gas.

In the first test under these conditions the test piece of aluminium alloy to D.T.D. 683 endured 27,000 cycles and then exploded, fragments being blown all over the place (VCF 3, Fig. 10 on page 23). This was surprising, because the precaution of closing the valve of the gas cylinder had been taken and the energy available to fragment the test section was only that of the gas within the tube under test.

Two lines developed out of this first test; one was to investigate the conditions under which explosive failure occurred, and the other to ascertain the degree in which this type of failure was ascribable to the use of gas as the pressure medium.

In prosecution of the second line, tests were made using oil as the pressure medium and other tests with a reduced volume of gas. The three conclusions from these tests were quite clear; first, that fragmentation was due to the energy in the gas and that, by sufficient reduction of the gas volume, failures similar to those resulting when oil was used as the pressure medium could be obtained; second, that the tendency to fragment was inherent in the material itself, being far greater in D.T.D. 683 than in B.S. L 65; and third, that the tendency to fragment arose from a liability of the materials to develop several axial cracks, which often extended well beyond the thin-walled section and even right through the much thicker enlarged ends.

The gradual thickening of the wall associated with a generous radius of transition fillet appears to offer little resistance to the propagation of these axial cracks, which can penetrate into sections where the wall thickness is ten times greater, whereas a more abrupt change of section, afforded by a small fillet radius, does prevent the crack spreading even into a section only four times thicker. A very small fillet radius, or a separate ring glued on, will result in circumferential cracking, after a shorter endurance but without catastrophic failure.

In respect of the comparison between failures under gas and oil pressure media, our conclusions have since been fully substantiated elsewhere in tests on much larger cylinders. It is notable that the tendency to fragment depends on the total energy in the gas and this energy is related not to the gas pressure p itself but to the hoop tension, $pD/(2t)$, to which that pressure gives rise. In short, the complete fragmentation of our cylinders with D/t of about 40 under 1000 lb./in.^{2} pressure may presage similar fragmentation of cylinders with D/t of about 3000 under a pressure of 13 lb./in.^{2}

The second and third conclusions led us, in the first and main line of investigation, to compare the behaviour of the three aluminium alloys, D.T.D. 683, B.S. L 65, B.S. L 64, and a mild steel under several systems of loading. The general result of the tests has been to confirm marked differences between the materials in their liability to fragment; D.T.D. 683 is by far the worst, B.S. L 65 is markedly less liable, but apparently slightly worse than B.S. L 64, while mild steel has not yet been made to fragment.

At the same time it soon became apparent that explosive failure as such was not inevitably associated with the tendency to fragment. Explosive failure seemed to depend not entirely on metallurgical factors but also very markedly on the mode of stressing. In short, we were forced to conclude that, under suitable conditions, even mild steel might fail explosively and we have indeed succeeded in causing mild steel test pieces to explode after endurances ranging from 10^4 up to 2 million cycles.

It appears that the type of stressing most likely to lead to explosive failure is that in which planes subjected to maximum range of shear stress are also subject to maximum static direct stress; this observation might have been anticipated—though it was not—from previous experience. The influence of metallurgical factors inherent in extruded or rolled bars is also marked and this influence may sometimes predominate.

An empirical explanation of explosive failure of tubes is offered, which appears to correlate the observations both in the present tests and in many tests on larger cylinders made elsewhere. However, this explanation merely relates the occurrence of fast failure to the dimensions of the tube and indicates how the unstable crack length may be related to the tube dimensions. It leaves open two other questions; one, what determines the unstable crack length in a flat plate? and the other, what determines the growth of the fatigue crack up to the unstable length?

Both questions are fundamental but, while the first is the subject of much intensive study at present in progress, the second is not receiving so much attention. The results of the tests described in this paper clearly indicate that the propagation of the fatigue crack up to the unstable length is often extremely fast. Indeed, it would scarcely be too much to claim that the initial fatigue crack may sometimes spring into existence at a length approaching or exceeding the unstable crack length. It is this occurrence which results in explosive failure and fragmentation.

2. Materials Tested

Tests were made on five aluminium alloys, supplied in 1 in. diameter extruded bars, two to specification D.T.D. 683, two to B.S. L 65 and one to B.S. L 64. The chemical compositions of these alloys and their heat treatments are given in Table I(*a*).

Tests were also made on a mild steel of 30 tons/in.^{2} tensile strength, also in the form of 1 in. diameter bar, the chemical composition of which is given in Table I (*b*).

The mechanical properties of all the materials used are given in Table II: the 0·1 per cent proof stress is quoted for the aluminium alloys and the yield stress for the steel. Table II also includes the tensile hoop stresses obtained from static bursting tests described in Section 4.

3. Preparation of Test Pieces

The tubular test pieces used for the main series of tests on aluminium alloys are shown in Figs. 1 (*a*) and 1 (*b*). They were made by first drilling an undersize hole, which was then finished to size by boring; in order to achieve the desired high quality

TABLE I

CHEMICAL COMPOSITION

(per cent)

(a) Aluminium Alloys

Material	*N.P.L. Test Mark*	Cu	Mg	Si	Fe	Mn	Ti	Cr	Zn
D.T.D. 683	VCF	1·1	2·8	0·15	0·48	0·28	0·06	0·11	5·65
	WMS	0·62	2·6	0·13	0·27	0·35	0·05	0·10	6·18
B.S. L 65	VCG	4·34	0·78	0·80	0·28	0·73	0·008	—	—
	MAK	4·29	0·78	0·79	0·37	0·73	0·008	—	—
B.S. L 64	VCH	4·14	0·76	0·80	0·28	0·73	0·008	—	—

Heat Treatment	
D.T.D. 683:	Solution treated for 2 hours at 465°C, quenched in cold water, straightened by stretching and artificially aged for 8 hours at 135°C.
B.S. L 64:	Solution heat treated for 40 minutes at 508°C, quenched in cold water and straightened by stretching.
B.S. L 65:	Solution heat treated for 40 minutes at 508°C, quenched in cold water and straightened by stretching, and artificially aged for 6 hours at 170°C.

(b) Mild Steel

N.P.L. Test Mark	C	Si	Mn	S	P
BNZ	0·046	0·12	0·66	0·016	0·026

TABLE II

MECHANICAL PROPERTIES

Material	*N.P.L. Test Mark*	*Yield or 0·1% Proof Stress,* (tons/in.²)	*Ultimate Tensile Stress* (tons/in.²)	*Elongation (per cent) on Gauge Length of* $4\sqrt{(area)}$	*Reduction of Area* (per cent)	*Diamond Pyramid Hardness*	*Hoop Stress Static Bursting* (tons/in.²)
D.T.D. 683	VCF	41 (P.S.)	43·5	10	14	200 (HD/10)	34
	WMS	39 (P.S.)	41·8	8·5	10·5	195 (HD/10)	—
B.S. L 65	VCG	30·4 (P.S.)	34·4	11	20·5	164 (HD/10)	—
	MAK	31·6 (P.S.)	35·6	13	—	157 (HD/30)	29
B.S. L 64	VCH	25·3 (P.S.)	36·0	14	15	146 (HD/10)	24·5
Mild Steel	BNZ	22·9 (Y)	30·0	—	65	150 (HD/30)	28·5

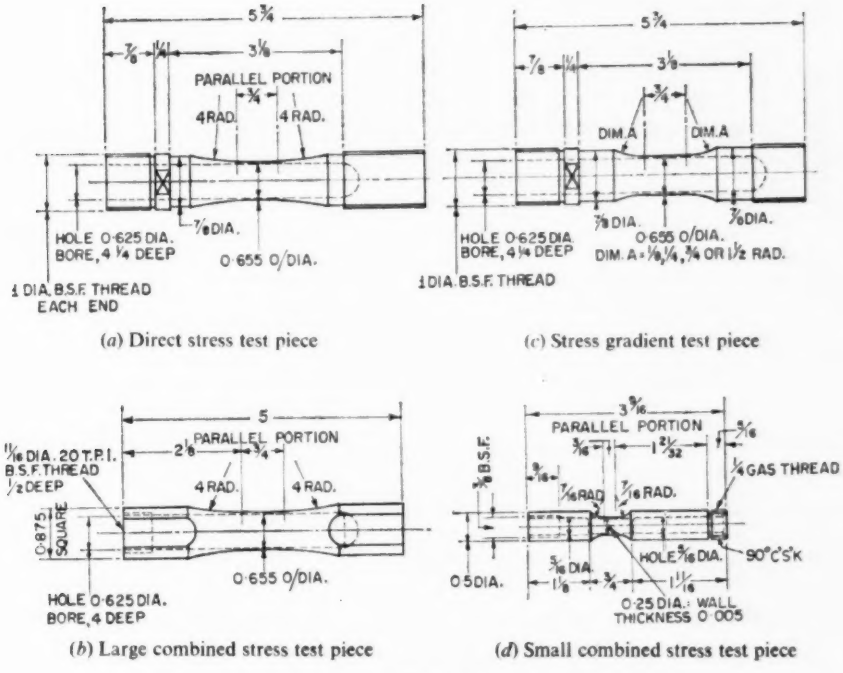

(*a*) Direct stress test piece

(*c*) Stress gradient test piece

(*b*) Large combined stress test piece

(*d*) Small combined stress test piece

FIGURE 1. The test pieces used (all dimensions are in inches).

of finish in these deep holes, extremely fine cuts were taken in the boring process. For the piece shown in Fig. 1 (*a*) the threaded ends were then formed and finally the test portion and fillets were turned coaxial with the bore; for the piece shown in Fig. 1 (*b*) the test portion and fillets were turned coaxial with the bore, before the square ends were machined. The steel pieces of this size were similar, but the wall thickness was 0·010 in.

To have polished the bore would have meant too great a risk of leaving it out of round; therefore, to maintain uniform wall thickness, both inner and outer surfaces were left as machined. The machine finish was, in fact, fairly good, and the influence of the surface irregularities on the fatigue strength was unlikely to have been great. In any case, this influence should have favoured the development of circumferential cracks, because all the turning marks ran in that direction, whereas in many tests axial cracks predominated.

Figure 1 (*d*) shows the form of a smaller test piece used in a later series of tests on the steel. In this case, since the required wall thickness was only 0·005 in., the test piece was redesigned as an open tube and the bore was lapped to allow precise location on the mandrel used to support it during the machining of the outer form. The test portion was polished circumferentially with 00 emery paper.

4. Bursting by Internal Pressure Only

To afford a comparison with the fatigue tests described later on, a series of tests was done in which test pieces were burst by the application of internal gas pressure only. The test piece was first filled with gas from a bottle at 2000 lb./in.^{2} pressure; then the gas supply was disconnected and oil pressure was used to compress the gas further until failure occurred. The gas volume involved in these tests was roughly the same as in subsequent tests under fatigue loading.

Tests were made on $\frac{5}{8}$ in. diameter tubes in the materials D.T.D. 683, B.S. L 65 and B.S. L 64; a $\frac{1}{4}$ in. tube of steel was also tested under gas pressure, and a $\frac{5}{8}$ in. tube of D.T.D. 683 was burst by oil pressure.

Photographs of the broken test pieces are shown in Fig. 8 on page 21. The values of ultimate tensile hoop stresses obtained are included in Table II; the value quoted for material VCF is the mean of three tests made with both the gas and oil pressure media; it is notable that the difference between the greatest and least of the three results was only 2 tons/in.^{2}. The values quoted for the other materials are based on a single test made with a gas pressure medium.

5. Fatigue Tests Under Biaxial Mean Stresses

5.1 Mode of Test

The mode of test adopted was to subject a tubular test piece to static internal pressure and to superimpose a fatigue loading of either direct stress, bending or torsion. The N.P.L. 1500 lb. Slipping Clutch Fatigue Machine was used for the direct stress fatigue tests and the N.P.L. Combined Stress Fatigue Machines, both large and small, were used for the torsion and bending fatigue tests.

The dimensions of the test pieces shown in Fig. 1 were determined by the capacities of the fatigue testing machines available and by the highest pressure (2000 lb./in.^{2}) readily available from gas cylinders.

To reduce the number of joints to be made gas tight, the test piece was made as a tube with a closed end. For the direct stress tests, access for the pressure medium to the bore of the tube was provided through the lower machine adaptor; in the torsion and bending tests, the supply pipe was connected straight to the test piece, through a suitable screwed connector, and this end of the test piece was mounted at the frame end of the machine. In the early tests a soft copper washer was used as a seal at the test piece end, but this was later replaced by a seal of hemp and jointing compound, which proved more satisfactory. The gas cylinder was connected to the test piece through a copper pipe, of 0·125 in. bore and about 7 ft. long, and the pressure applied was read by a gauge at the pipe end immediately adjacent to the gas cylinder. After the desired pressure had been attained, the valve on the cylinder was almost closed again, leaving just a sufficient opening to annul the very slight leakage in the system. Consequently, when the test piece failed the pressure fell at once to zero, and the gas released was restricted to that in the test piece and connecting pipe.

The procedure adopted for testing was to mount a test piece in the machine, test the system for pressure tightness, and then to set the pressure to the required value. When the fatigue loading was pulsating direct stress, the mean axial load was applied, this load being adjusted to the value which, together with the axial load due to the internal pressure, would afford the desired mean axial stress: the machine was then set running at the desired load range. In the tests in the combined stress machine, the gas pressure set up both hoop tension and axial tension half as great. When the pressure had been set to the desired value and maintained for a few minutes, the machine was set running at the desired range of load.

Examination of the fractured surfaces of some of the early pieces tested in direct stress indicated that these surfaces had been forced together by the sudden reduction of mean load resulting from the release of gas pressure when the test piece broke. This effect was overcome by fitting stops to limit the axial motion of the machine loading frame.

5.2. Direct Stress Pulsating Tests

The tests made under pulsating direct stress fatigue loading, with a superimposed hoop tensile stress, were sub-divided into two main groups. One series, to determine the effect of the hoop stress on the mode of failure, was run at a constant value of pulsating stress with the pieces loaded at several values of static hoop stress; the other series, to determine the effect of the pulsating stress, was run at a low value of hoop stress over a range of pulsating stresses.

The results of these tests are given in Tables III and IV, and the *S-N* curves are plotted in Figs. 2, 3, 4 and 5. Only a few check tests were made on the steel and these results are not shown plotted but are given in Table IV only. Photographs of the broken test pieces in all the materials tested are given in Fig. 10 on page 23.

5.3. Tests with Varying Energy Content of Pressure Medium

The pulsating direct stress tests mentioned in Section 5.2 were made using a gas pressure medium; the energy released at fracture by expansion of the gas within the test piece was of the order of 100 ft.lb. Clearly this release of energy would be expected to enhance the tendency to shatter and, accordingly, to determine how far shatter depended upon this release of energy, a number of tests were made with a pressure medium of varying energy content.

Tests were made on three pieces of D.T.D. 683, to Fig.1 (*a*), in which the internal volume was reduced by fitting plugs of varying clearance to the bore of the test pieces. These reduced the volume to about 20 per cent, 3 per cent and 0·3 per cent of the total, while leaving the hoop stress unaltered; the results of these tests are given in Table V. Three further test pieces of D.T.D. 683 were tested full of oil and, also, one piece of B.S. L 65; the results of these tests are included in Table III, and are plotted in Fig. 2 for comparison. Photographs of these broken pieces, which show the effect of energy content on the mode of failure, are given in Fig. 9 on page 22.

TABLE III

DIRECT STRESS FATIGUE TESTS WITH BIAXIAL MEAN STRESS
(VARYING HOOP STRESS WITH A NOMINALLY CONSTANT PULSATING STRESS)

Material	*N.P.L. Test Mark*	*Pulsating Stress* (tons/in.²)	*Hoop Stress* (tons/in.²)	*Endurance* (10^6 cycles)	*Pressure Medium*	*Type of Fracture*
D.T.D. 683	VCF 6	14·2±14·2	18·6	0·040 B	oil	Longitudinal split
	13A	8·7±15·0	17·3	0·027 B	nitrogen	Shattered
	14A	14·8±13·7	16·2	0·047 B	nitrogen	Shattered
	15A	14·2±14·2	14·0	0·062 B	nitrogen	Shattered
	8	14·2±14·2	12·1	0·049 B	oil	Broken in two halves
	3	14·2±14·2	10·2	0·067 B	nitrogen	Shattered
	7	13·7±13·7	7·2	0·072 B	oil	Broken in two halves
	2	13·7±13·7	7·2	0·082 B	nitrogen	Shattered
	1	14·2±14·2	5·6	0·059 B	nitrogen	Broken in two halves, but longitudinal cracks also formed
	5	13·7±13·7	4·5	0·049 B	air	Broken in two halves
	11	14·2±14·2	0	0·053 B	—	Broken in two halves
	4	10·1±10·1	0	0·022 B	—	Broken in two halves but test piece contained a flaw
B.S. L 65	VCG 7	14·2±14·2	18·6	0·004 B	oil	Broken in two halves but also split longitudinally
	6	14·2±14·2	18·6	0·021 B	air	Shattered
	5	13·7±13·7	15·3	0·001 B	nitrogen	Shattered. (Turning marks in bore)
	3	13·3±13·3	15·3	0·031 B	air	Broken in two halves
	1	13·7±13·7	14·0	0·045 B	nitrogen	Broken in two halves
	2	12·9±12·9	11·7	0·057 B	nitrogen	Broken in two halves
	12*	14·2±14·2	8·0	0·028 B	air	Broken in two halves
	4	12·9±12·9	4·2	0·029 B	air	Broken in two halves
	10	10·1±10·1	0	0·076 B	—	Broken in two halves
	12	7·0± 7·0	0	1·51 U	—	Unbroken
B.S. L 64	VCH 1	12·9±12·9	16·5	0·059 B	nitrogen	Broken in two halves, tendency for longitudinal tearing
	6	13·7±13·7	10·1	0·020 B	air	Broken in two halves, longitudinal tears following extrusion lines
	2	13·3±13·3	5·3	0·096 B	air	Broken in two halves
	4	10·0±10·0	0	2·38 B	—	Broken in two halves

*Previously run at a lower stress B = Broken U = Unbroken

TABLE IV

DIRECT STRESS FATIGUE TESTS WITH BIAXIAL MEAN STRESS
(VARYING PULSATING STRESS WITH A NOMINALLY CONSTANT HOOP STRESS)

Material	*N.P.L. Test Mark*	*Pulsating Stress* (tons/in.^{2})	*Hoop Stress* (tons/in.^{2})	*Endurance* (10^6 cycles)	*Pressure Medium*	*Type of Fracture*
D.T.D. 683	VCF 1	14·2±14·2	5·6	0·059 B	nitrogen	Broken in two halves, longitudinal cracks also
	5	13·7±13·7	4·5	0·049 B	air	Broken in two halves, but torn longitudinally
	9	10·5±10·5	5·6	0·460 B	nitrogen	Shattered
	10	9·0± 9·0	5·9	0·185 B	nitrogen	Broken in two halves but torn longitudinally
	12	8·0± 8·0	6·0	4·84 B	air	Broken in two halves, longitudinal cracks also
	11	7·0± 7·0	6·0	4·67 U	nitrogen	Unbroken
B.S. L 65	VCG 4	12·9±12·9	4·2	0·029 B	air	Broken in two halves
	8	10·1±10·1	5·9	0·086 B	nitrogen	Broken in two halves
	9	7·0± 7·0	5·9	0·113 B	nitrogen	Broken in two halves
	11	7·0± 7·0	5·9	0·345 B	nitrogen	Broken in two halves
	10*	6·0± 6·0	5·4	1·03 U	nitrogen	Unbroken
	10	5·0± 5·0	5·9	4·12 U	nitrogen	Unbroken
B.S. L 64	VCH 2*	13·3±13·3	5·3	0·096 B	air	Broken in two halves
	3	10·0±10·0	5·0	0·244 B	air	Broken in two halves, also torn longitudinally
	5	9·0± 9·0	5·4	0·283 B	air	Broken in two halves, also torn longitudinally
	4	8·0± 8·0	5·2	4·01 U	air	Unbroken
	2	6·8± 6·8	5·7	4·09 U	air	Unbroken
Mild Steel	BNZ 13F1*	14·3±14·3	16·7	0·320 B	air	Transverse fatigue crack half way round piece
	2	13·0±13·0	18·6	0·645 B	air	Transverse fatigue crack half way round piece
	1	11·5±11·5	18·6	1·87 U	air	Unbroken

*Previously run at a lower stress B = Broken U = Unbroken

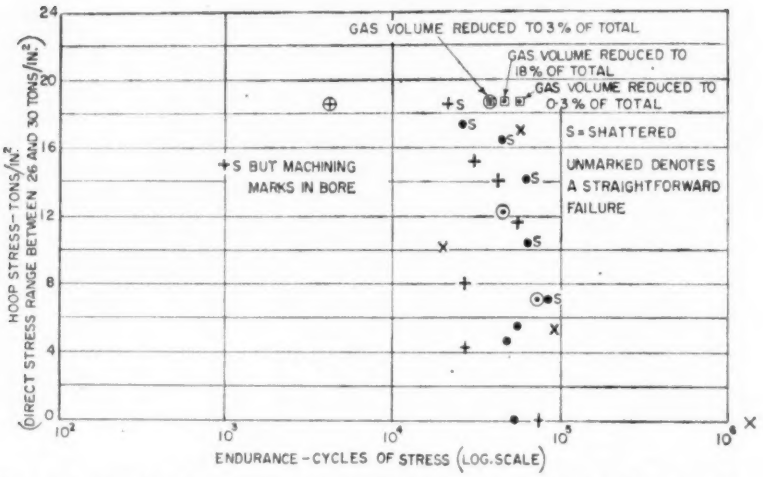
GAS VOLUME REDUCED TO 3% OF TOTAL
GAS VOLUME REDUCED TO 18% OF TOTAL
GAS VOLUME REDUCED TO 0·3% OF TOTAL
S = SHATTERED
UNMARKED DENOTES A STRAIGHTFORWARD FAILURE
+S BUT MACHINING MARKS IN BORE
HOOP STRESS-TONS/IN² (DIRECT STRESS RANGE BETWEEN 26 AND 30 TONS/IN²)
ENDURANCE-CYCLES OF STRESS (LOG. SCALE)

FIGURE 2. Varying hoop stress with a nominally constant pulsating direct stress.

Material D.T.D. 683:
- ● Gas pressure medium
- ⊙ Oil pressure medium
- ⊡ Gas pressure medium Reduced volume

N.P.L. test mark: VCF.

Material B.S. L 65:
- \+ Gas pressure medium
- ⊕ Oil pressure medium

N.P.L. test mark: VCG.

Material B.S. L 64:
- × Gas pressure medium

N.P.L. test mark: VCH.

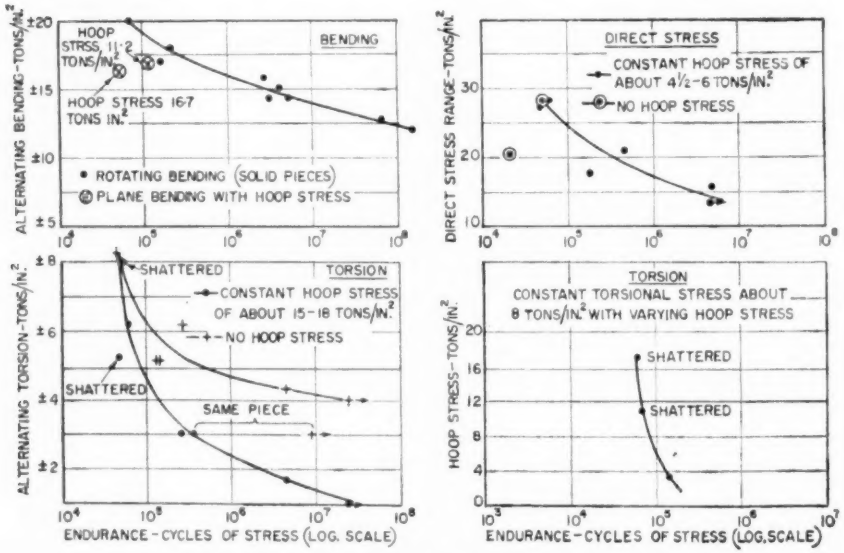

FIGURE 3. Material: D.T.D. 683. N.P.L. test mark: VCF.

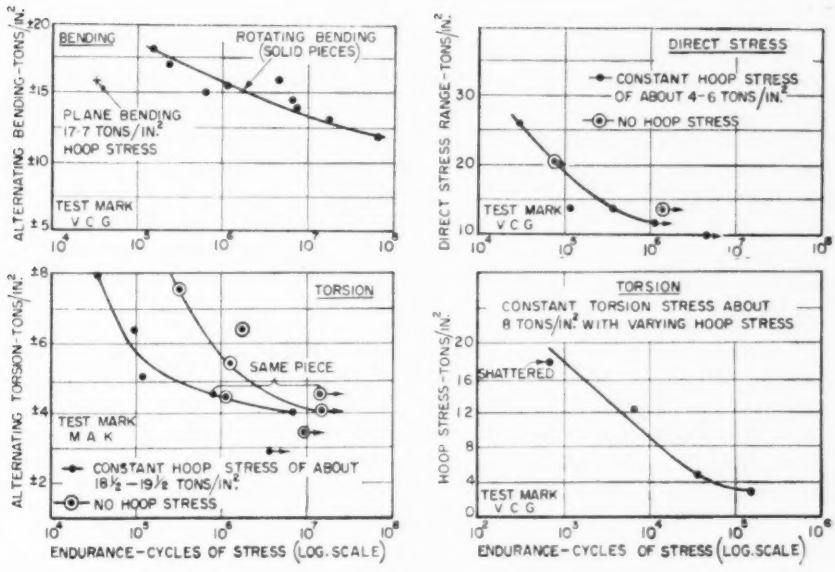

FIGURE 4. Material: B.S. L 65. N.P.L. test mark: VCG and MAK.

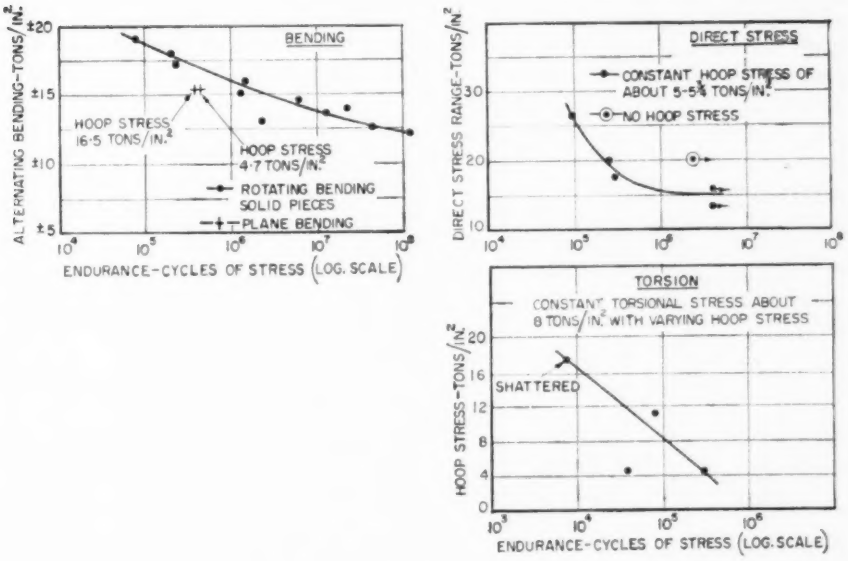

FIGURE 5. Material: B.S. L 64. N.P.L. test mark: VCH.

5.4. Effect of Stress Gradient

A limited number of tests were made on material D.T.D. 683, to check the effect of the transition radii at the ends of the test portion on the propagation of the longitudinal cracks. From the other tests it was known that these cracks developed extremely fast in D.T.D. 683, particularly at high values of pulsating direct stress and hoop stress, and propagated well into the enlarged ends of the test pieces, as shown in Fig. 10 on page 23. The form of test piece used in this series of tests is shown in Fig. 1(*c*) and tests were made with fillet radii of $\frac{1}{8}$, $\frac{1}{4}$, $\frac{3}{4}$ and $1\frac{1}{2}$ in.; pieces with 4 in. radii had already been covered in the other tests. In addition, a test was made on a piece to Fig. 1(*a*), but with a ring $\frac{3}{8}$ in. wide Redux-bonded around the centre of the test portion.

The pieces were all tested at about the same condition of loading, a high range of pulsating direct stress and a high hoop stress. The results of the tests are given in Table VII and the endurances to fracture are plotted in Fig. 6; included in this figure, but not in the table, are the results of some earlier tests made with varying fillet radii. Photographs of the broken test pieces are shown in Fig. 14 on page 27, and Fig. 7 shows a diagram of the nominal stress gradients associated with the fillet radii tested.

5.5. Alternating Bending Tests

A few check tests were made under alternating bending with superimposed tensile hoop stress and axial tension on pieces to Fig. 1 (*b*) in all the aluminium alloys. The results, given in Table VI, are plotted as *S*-*N* curves in Figs. 3, 4 and 5. Photographs of the broken pieces are shown in Fig. 11 on page 24: the mode of failure of the piece VCH 8 (B.S. L 64) relates to a test made under a low hoop stress, but another test, made under a hoop stress of 45 per cent, resulted in a fracture almost indistinguishable from that shown.

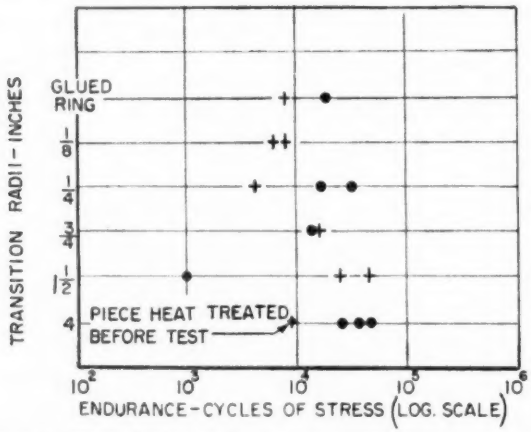

Figure 6. Effect of stress gradient on crack penetration. D.T.D. 683.
● N.P.L. test mark VCF
\+ N.P.L. test mark WMS

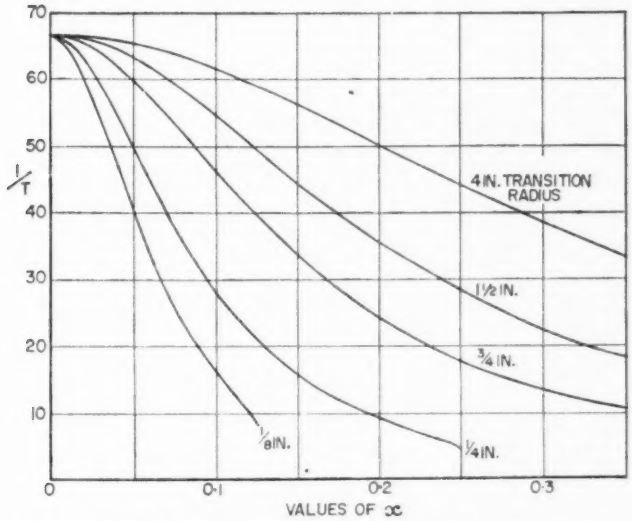

FIGURE 7. Effect of stress gradient on crack propagation under fatigue. (x is the distance in inches from the parallel section.)

For comparison the results of rotating-bending fatigue tests on materials D.T.D. 683, B.S. L 64 and B.S. L 65 are given in Table VIII and are also included in Figs. 3, 4 and 5: the results for the mild steel are given in Table VIII only.

5.6. Alternating Torsion Tests

A number of tests under alternating torsional stress with superimposed tensile hoop stress and axial tension were made on all materials; the pieces were to Fig. 1 (*b*). The first tests were made with a constant alternating stress at different values of static stresses. Because the results obtained were most unexpected, additional tests were made on D.T.D. 683 and B.S. L 65 at various levels of alternating torsion, with and without static stresses. The results of all these tests are given in Table IX, and the *S-N* curves are plotted in Figs. 3, 4 and 5; Figs. 12, 13 and 16 show photographs of some of these $\frac{5}{8}$ in. diameter broken test pieces.

6. Unstable Crack Length

In Appendix I an empirical theory is developed which indicates how the unstable crack length may be expected to diminish as the size of the tube is reduced. The values of unstable crack length indicated by this theory are in fair agreement with observations made on larger tubes elsewhere (*see* Appendix I).

Observation of the crack lengths developed in $\frac{5}{8}$ in. tubes of mild steel under fatigue loading (piece BNZ 13F5, Fig. 16 on page 28) suggested that in smaller tubes the initial fatigue crack might prove unstable. In order to test this inference, a

TABLE V

EFFECT OF ENERGY CONTENT OF PRESSURE MEDIUM ON CRACK PROPAGATION UNDER DIRECT STRESS FATIGUE AND HIGH HOOP TENSION

Material: D.T.D. 683

Pressure Medium: Nitrogen

N.P.L. Test Mark	*Pulsating Stress* (tons/in.^{2})	*Hoop Stress* (tons/in.^{2})	*Gas Volume* (percentage of total)	*Endurance* (10^6 cycles)	*Remarks*
VCF 19	14·2±14·2	18·6	18	0·047 B	Exploded; large piece broken out, including portion of thick material: cracks running well into enlarged end
VCF 20	14·2±14·2	18·6	3	0·040 B	Fractured circumferentially, but longitudinal cracks also present
VCF 22	14·5±14·5	18·0	0·3	0·058 B	No explosion, broken in two halves, tendency for longitudinal cracks to form

TABLE VI

FATIGUE TESTS IN BENDING ON TUBULAR PIECES WITH AND WITHOUT A HOOP STRESS

Material	*N.P.L. Test Mark*	*Alternating Stress* (tons/in.^{2})	*Hoop Stress* (tons/in.^{2})	*Endurance* (10^6 cycles)	*Pressure Medium*	*Type of Fracture*
D.T.D. 683	VCF 14	±16·4	16·7	0·059 B	nitrogen	Exploded; large cracks running into enlarged ends
	15	±17·0	11·2	0·110 B	nitrogen	Transverse crack only; no longitudinal cracks visible
B.S. L 65	VCG 15	±16·0	17·7	0·031 B	nitrogen	Cracked only
B.S. L 64	VCH 9	±15·3	16·5	0·419 B	nitrogen	Cracked only
	8	±15·3	4·65	0·425 B	air	Cracked only

B = Broken

TABLE VII

EFFECT OF STRESS GRADIENT ON THE PROPAGATION OF FATIGUE CRACKS

Material: D.T.D. 683

Pressure medium: Nitrogen

N.P.L. Test Mark	*Transition Radii* (in.)	*Pulsating Stress* (tons/in.^{2})	*Hoop Stress* (tons/in.^{2})	*Endurance* (10^6 cycles)	*Remarks*
WMS 1	$\frac{1}{8}$	13·6±13·6	14·6	0·009 B	Exploded; centre portion blown out and split longitudinally; short longitudinal crack at one fillet
2	$\frac{1}{8}$	14·5±14·5	18·4	0·007 B	Exploded; centre portion shattered; short longitudinal crack at one fillet
4	$\frac{1}{4}$	14·6±14·6	18·4	0·005 B	Exploded; centre portion shattered; longitudinal crack stopped in fillet
5	$\frac{3}{4}$	14·8±14·8	18·8	0·017 B	Exploded; centre portion shattered; longitudinal crack stopped in fillet
7	$1\frac{1}{2}$	14·3±14·3	15·4	0·043 B	Circumferential crack only at centre of test length
8	$1\frac{1}{2}$	14·8±14·8	18·8	0·026 B	Exploded; centre portion shattered; longitudinal crack through both fillets
19*	4	14·5±14·5	18·4	0·008 B	Exploded; centre portion shattered and longitudinal cracks well into enlarged ends
20	glued ring	14·8±14·8	18·8	0·009 B	Exploded; circumferential crack around edge of ring

*Heated to 140°C for 20 minutes and allowed to cool in oven to simulate heat treatment given to WMS 20 B = Broken

TABLE VIII

ROTATING-BENDING FATIGUE TESTS

Material	*N.P.L. Test Mark*	*Alternating Stress* (± tons/in.²)	*Endurance* (10^6 cycles)	*Material*	*N.P.L. Test Mark*	*Alternating Stress* (± tons/in.²)	*Endurance* (10^6 cycles)
D.T.D. 683	VCF	20·0	0·074 B	B.S. L 64	VCH	19·0	0·083 B
		18·0	0·238 B			18·0	0·209 B
		17·0	0·183 B			17·0	0·263 B
		16·0	2·97 B			16·0	1·71 B
		15·0	4·14 B			15·0	1·31 B
		14·0	3·13 B			14·5	6·06 B
		14·0	5·04 B			14·0	24·5 B
		13·0	69·5 B			13·5	13·5 B
		12·0	136·5 B			13·0	2·36 B
		12·0	167·9 U			12·5	49·0 B
B.S. L 65	VCG	18·0	0·171 B			12·0	111·4 U
		17·0	0·244 B	Mild Steel	BNZ 2F27*	22·0	0·069 B
		16·0	4·60 B		25*	20·0	0·245 B
		15·5	1·10 B		26	18·0	0·614 B
		15·0	0·639 B		24	17·8	1·27 B
		14·5	6·99 B		27*	17·5	12·4 U
		14·0	7·69 B		27	16·5	25·9 U
		13·0	19·6 B		25*	16·0	12·6 U
		12·0	61·9 B		25	14·0	22·5 U
	MAK	18·0	0·886 B				
		17·0	1·92 B				
		16·0	4·86 B				
		15·0	10·2 B				
		14·0	21·3 B				
		13·0	33·8 B				
		12·0	34·6 B				
		11·0	48·0 B				
		10·0	60·4 U				

*Previously run at a lower stress B = Broken U = Unbroken

TABLE IX

FATIGUE TESTS IN TORSION ON TUBULAR PIECES WITH AND WITHOUT A HOOP STRESS

Material	*N.P.L. Test Mark*	*Alternating Stress* (tons/in.^{2})	*Hoop Stress* (tons/in.^{2})	*Endurance* (10^6 cycles)	*Pressure Medium*	*Type of Fracture*
D.T.D. 683	VCF 13	± 8·0	17·5	0·059 B	nitrogen	Shattered; central portion blown out longitudinally; cracks into enlarged ends
	16	± 8·2	11·3	0·070 B	nitrogen	Exploded; central portion blown open with transverse and longitudinal cracks
	18	± 8·2	3·7	0·137 B	air	Exploded; main transverse crack and secondary longitudinal crack
	VCF 13	± 8·0	17·5	0·059 B	nitrogen	Shattered; central portion blown out, longitudinal cracks into enlarged ends
	25	± 6·1	17·1	0·063 B	nitrogen	Longitudinal crack
	26	± 5·2	16·2	0·050 B	nitrogen	Shattered, as VCF 13
	28	± 3·1	15·8	0·248 C		Circumferential crack 0·06 in. in length
	29*	± 3·1	15·1	0·346 B	nitrogen	Main transverse crack and secondary longitudinal crack
	34*	± 1·8	18·9	5·33 B	nitrogen	Circumferential crack with small longitudinal cracks
	34	± 0·9	18·9	25·4 U	nitrogen	
	VCF 35	± 8·2	0	0·048 B	—	Circumferential crack
	36	± 6·1	0	0·388 B	—	
	37	± 5·1	0	0·133 B	—	
	38	± 5·1	0	0·132 B	—	
	40	± 4·3	0	4·40 B	—	
	24	± 4·0	0	27·4 U	—	
	29	± 3·1	0	9·96 U	—	

*Previously run at a lower stress B = Broken U = Unbroken C = Cracked

[continued over

TABLE IX (*contd.*)

FATIGUE TESTS IN TORSION ON TUBULAR PIECES WITH AND WITHOUT A HOOP STRESS

Material	*N.P.L. Test Mark*	*Alternating Stress* (tons/in.²)	*Hoop Stress* (tons/in².)	*Endurance* (10^6 cycles)	*Pressure Medium*	*Type of Fracture*
B.S. L 65	VCG 16	± 8·8	12·2	0·006 B	nitrogen	Longitudinal crack
	17	± 8·0	3·1	0·163 B	air	Longitudinal crack
	14	± 8·0	5·0	0·038 B	nitrogen	Circumferential main cracks with secondary longitudinal crack
	13	± 8·0	18·0	0·0007 B	nitrogen	Exploded; centre portion unfolded and blown out in one piece
	MAK 7*	± 7·9	19·2	0·039 B	nitrogen	Longitudinal crack
	2	± 6·3	18·5	0·098 B	nitrogen	Exploded; longitudinal crack
	4	± 5·1	19·7	0·116 B	nitrogen	Longitudinal crack
	9*	± 4·7	18·7	0·850 B	nitrogen	Circumferential crack
	10	± 4·0	20·4	6·80 B	nitrogen	Shattered; main longitudinal crack
	7	± 3·0	19·5	3·84 U	nitrogen	
	MAK 5	± 7·6	0	0·319 B	—	Circumferential crack
	14	± 6·4	0	1·74 B	—	Circumferential crack
	3	± 5·5	0	1·16 B	—	Circumferential crack
	9*	± 4·7	0	15·7 U	—	
	16	± 4·5	0	1·04 B	—	Tensile crack (45° to axis)
	11	± 4·0	0	12·0 U	—	
	9	± 3·5	0	9·40 U	—	
B.S. L 64	VCH 10	± 8·0	17·3	0·007 B	nitrogen	Exploded; test portion torn open
	12	± 7·8	4·7	0·301 B	air	Main circumferential crack with secondary longitudinal crack
	11	± 7·7	11·0	0·081 B	nitrogen	Main longitudinal crack with secondary tensile cracks
	7	± 7·7	4·7	0·039 B	air	Circumferential crack
Mild Steel	BNZ 13F3	±13·3	17·4	0·024 B	nitrogen	Small longitudinal shear cracks with tensile cracks at ends of main crack
	5	±11·3	15·2	0·088 B	nitrogen	Multi longitudinal cracks with tensile cracks at ends of main cracks

*Previously run at a lower stress B = Broken U = Unbroken C = Cracked

TABLE X

LENGTH OF FATIGUE CRACKS IN MILD STEEL PIECES TESTED UNDER ALTERNATING TORSION AND STATIC HOOP TENSION

N.P.L. Test Mark	*Mean Wall Thickness* (1/1000 in.)	*Alternating Torsional Stress* (tons/in.²)	*Hoop Stress* (f_0) (tons/in.²)	*Endurance* (10^6 cycles)	*Total Length of Axial Crack before Branching*† (1/1000 in.)	***Unstable Length of Crack* (1/1000 in.)	*Remarks*
			(*a*) 1/4 INCH DIAMETER				
BNZ 2F7	5·3	±11·6	10·7	0·085 U			
		±11·6	16·1	0·047 U			
		±11·6	20·4	0·226 U			
		±15·5	20·4	0·105 B	80	70	No explosion
BNZ 2F8	4·3	±18·8	24·7	0·009 B	200	45	Semi-explosion
BNZ 2F9	4·8	±12·8	22·0	0·030 B	220	60	Explosion
BNZ 2F10	6·3	±12·9	16·2	0·236 B	15	95	No explosion
			(*b*) 5/8 INCH DIAMETER				
BNZ 2F12	10·5	±13·3	18·6	0·005 B	41	180	
19	10·3	±11·0	18·4	0·012 B	75	185	
23	10·8	±8·3	21·2	0·009 B	450	155	Explosion
20	10·8	±8·3	19·5	0·299 B	250	170	
13	10·8	±8·3	19·0	0·670 B	105	180	
14	11·5	±7·3	19·7	0·832 B	290	175	
15	9·8	±6·7	22·0	2·01 B	900	155	Exploded
18		±6·7	20·3	1·30 B	240	165	Failure not observed
21	10·8	±6·5	19·5	0·279 B	370	170	Failure not observed
18*		±5·8	21·0 to 20·6	58·5 U			
18*	10·8	±5·8	19·5 to 20·0	70·8 U			
BNZ 2F22	10·0	±11·1	0	0·891 B	All cracks circumferential		
17	8·0	±9·9	0	0·038 B			
16	9·6	±9·3	0	0·032 B			

B = Broken U = Unbroken * Previous tests † *See*, for instance, BNZ 13F5, Fig. 16

** Computed from equation (1) of Appendix I on the assumption that fast failure occurs when $f_a + f_0$ exceeds the hoop tensile strength, namely 28·5 tons/in.²

number of mild steel test pieces of the form shown in Fig. 1(*d*), 0·25 in. bore and 0·005 in. wall thickness, were tested under alternating torsion and internal pressure affording hoop and axial static tensions.

The results of the tests are given in Table X(*a*) and a photograph of the pieces after test is given in Fig. 15. Included in Table X(*a*) are the apparent lengths of the axial fatigue cracks as measured from the broken pieces, using a travelling microscope, and the unstable crack lengths as computed according to Appendix I, using the experimental value of the hoop tensile stress, namely 28·5 tons/in.^{2}

Because of the uncertainty of the stress combination that these particular pieces would withstand, the stress applied to the first piece was increased in stages, the hoop stress being first raised to the maximum gas pressure available before the torsional stress was increased. The stresses quoted are nominal values based on the mean wall thickness of the tube.

Subsequently a series of pieces of mild steel of the larger size (Fig. 1 (*b*), but having the wall thickness 0·010 in.) were tested under alternating torsion, with superimposed static stresses set up by internal gas pressure. The results of these tests are given in Table X(*b*) and a photograph of some of the pieces after test is given in Fig. 16.

7. Conclusion

The evidence afforded by the present tests has to be reviewed in relation to two separate questions:—

(*a*) In what way and to what extent does biaxial mean stress affect failure by fatigue?

(*b*) Under what conditions does fatigue failure develop almost instantaneously into complete rupture?

For convenience of comparison in relation to these questions, the hoop tensile and fatigue stresses quoted with the photographs (Figs. 10 to 16) are there expressed as ratios to the tensile strengths of the materials. The actual values are given in the tables.

Under direct stress or bending, high hoop stress due to internal pressure does not materially reduce endurance under high fatigue stresses; nor is the endurance affected by the energy content of the pressure medium. Under torsion, however, internal pressure does markedly reduce endurance; for instance, one piece (VCF 29) after an endurance of 10 million cycles without internal pressure, failed when internal pressure was applied after a further 350,000 cycles of the same range of shear stress.

Sufficiently high internal pressure may markedly affect the mode of failure by fatigue and cause it to develop almost instantaneously into complete rupture.

Under static loading, fast fracture is known to develop once a crack or slit exceeds a certain unstable length. Under any particular loading condition the unstable length is a characteristic of the material; but, for tubes of any one material, the length is shorter the smaller the diameter of the tube and the higher the hoop tensile stress.

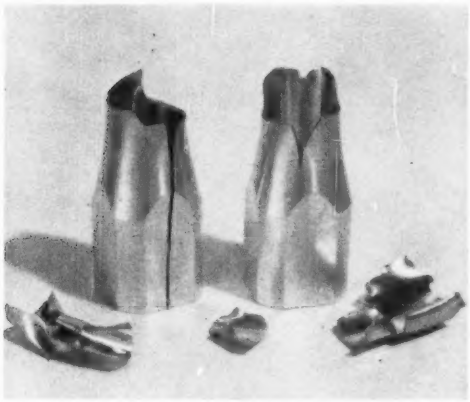

D.T.D. 683 (VCF 23)
Burst by gas pressure

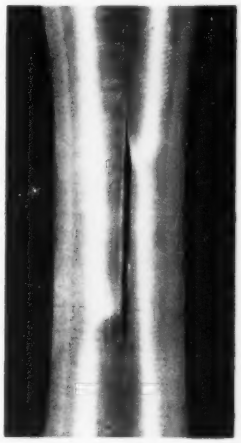

D.T.D. 683 (VCF 27)
Burst by oil pressure

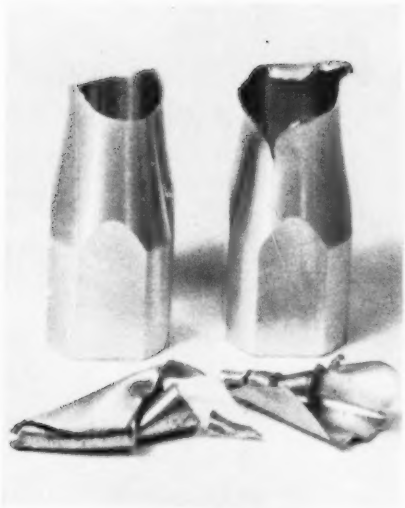

B.S. L 65 (MAK 15)
Burst by gas pressure

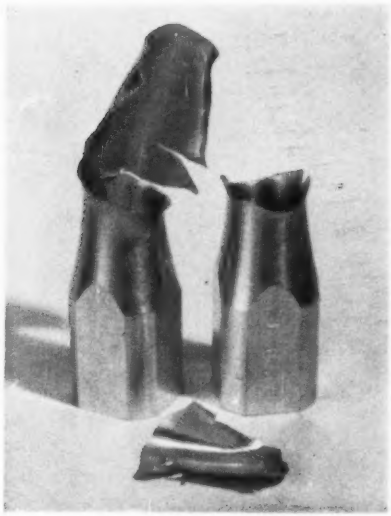

B.S. L 64 (VCH 13)
Burst by gas pressure

FIGURE 8. Cracks due to static pressure.

D.T.D. 683 (VCF 19)
Gas pressure
18% of total volume

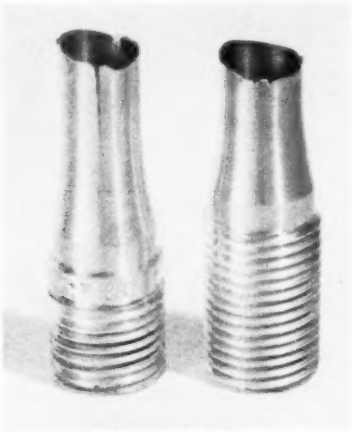

D.T.D. 683 (VCF 20)
Gas pressure
3% of total volume

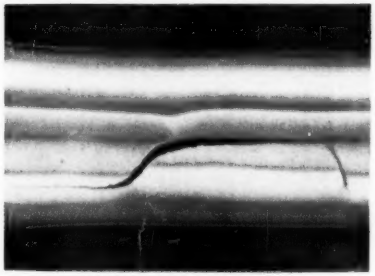

D.T.D. 683 (VCF 6)
Oil pressure

D.T.D. 683 (VCF 22)
Gas pressure
0·3% of total volume

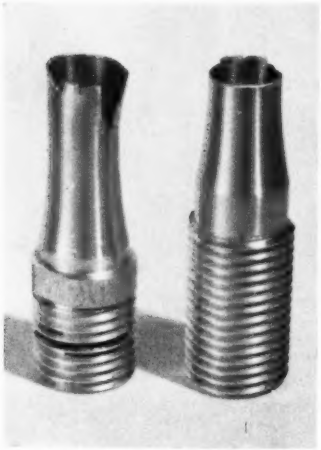

B.S. L 65 (VCG 7)
Oil pressure

FIGURE 9. Effect of energy content of pressure medium on crack propagation under fatigue.

D.T.D. 683 (VCF 3)
Hoop stress 25%
Range of direct stress 65%

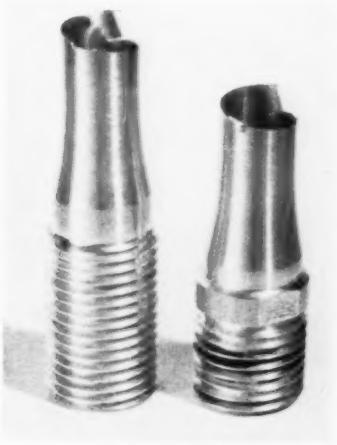

D.T.D. 683 (VCF 5)
Hoop stress 10%
Range of direct stress 65%

Right:
B.S. L 64 (VCH 1)
Hoop stress 45%
Range of direct stress 70%

B.S. L 65 (VCG 6)
Hoop stress 55%
Range of direct stress 85%

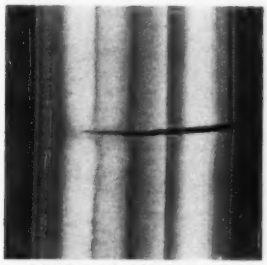

Mild steel (BNZ 13 F 1)
Hoop stress 35%
Range of direct stress 60%

FIGURE 10. Fatigue cracks under pulsating direct stress and static hoop tension.

D.T.D. 683 (VCF 14)
Hoop stress 40%
Range of bending stress 75%

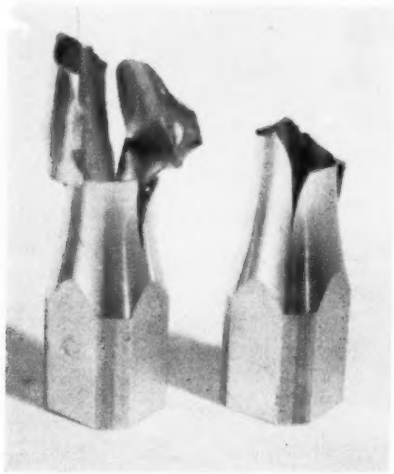

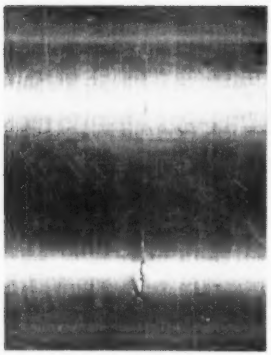

D.T.D. 683 (VCF 15)
Hoop stress 25%
Range of bending stress 80%

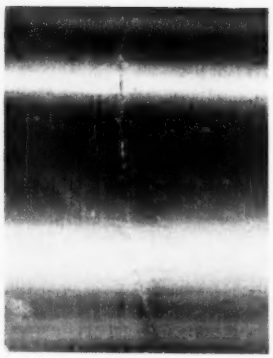

B.S. L 65 (VCG 15)
Hoop stress 50%
Range of bending stress 95%

B.S. L 64 (VCH 8)
Hoop stress 15%
Range of bending stress 85%

FIGURE 11. Fatigue cracks under alternating bending and static hoop tension.

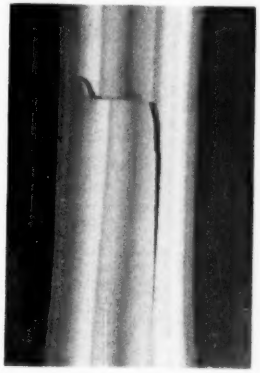

Left:
D.T.D. 683 (VCF 18)
Hoop stress 10%
Range of torsion stress 40%

Right:
B.S.L. 65 (VCG 16)
Hoop stress 35%
Range of torsion stress 50%

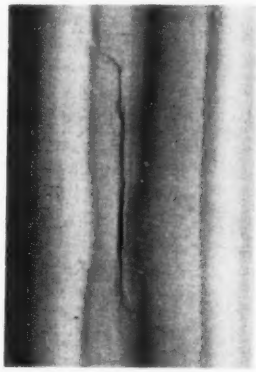

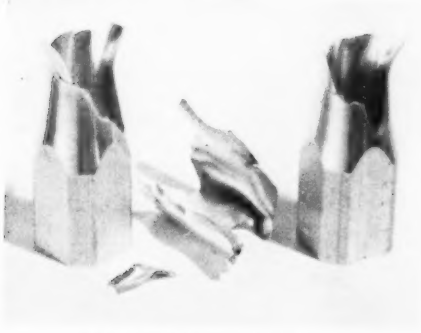

D.T.D. 683 (VCF 13)
Hoop stress 40%
Range of torsion stress 35%

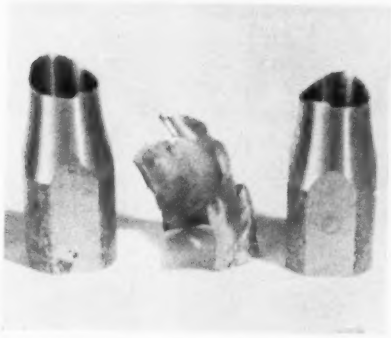

B.S. L 65 (VCG 13)
Hoop stress 50%
Range of torsion stress 45%

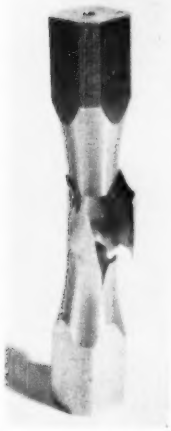

Left:
D.T.D. 683
(VCF 16)
Hoop stress 25%
Range of torsion stress 40%

Right:
D.T.D. 683
(VCF 34)
Hoop stress 45%
Range of torsion stress 10%

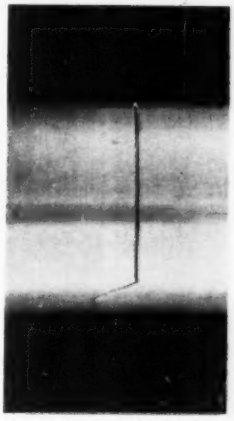

FIGURE 12. Fatigue cracks under alternating torsion and static hoop tension.

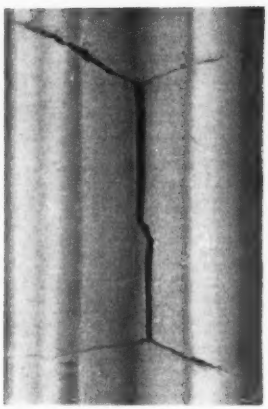

B.S. L 65
(VCG 17)
Hoop stress 10%
Range of torsion stress 45%

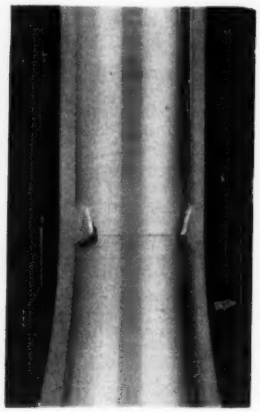

B.S. L 64
(VCH 7)
Hoop stress 15%
Range of torsion stress 45%

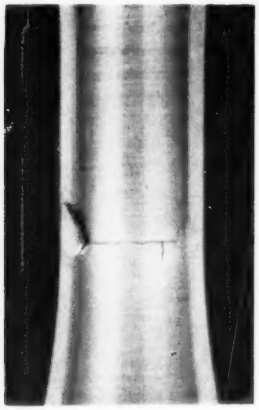

B.S. L 64
(VCH 12)
Hoop stress 15%
Range of torsion stress 45%

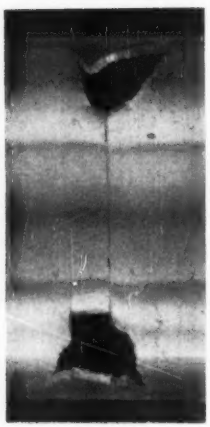

B.S. L 65
(VCG 14)
Hoop stress 15%
Range of torsion
stress 45%

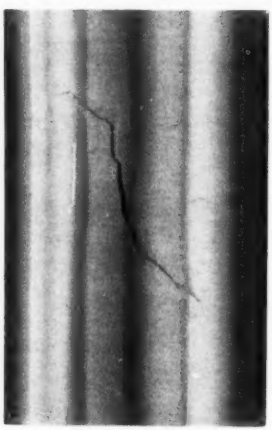

B.S. L 64
(VCH 11)
Hoop stress 30%
Range of torsion stress 45%

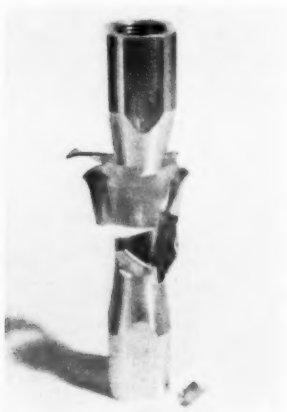

B.S. L 64
(VCH 10)
Hoop stress 50%
Range of torsion stress 45%

FIGURE 13. Fatigue cracks under alternating torsion and static hoop tension.

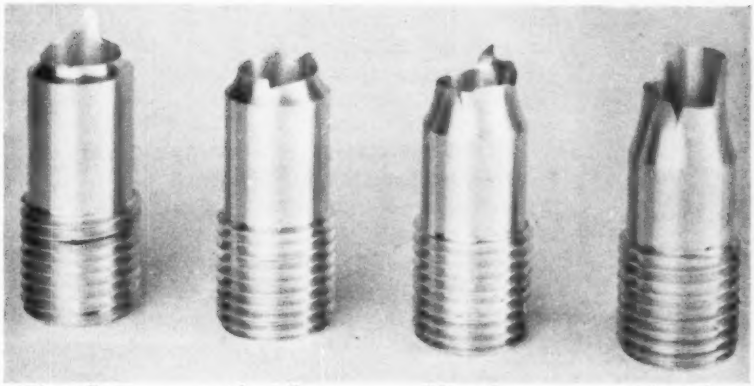

$\frac{1}{8}$ in. radius $\frac{1}{4}$ in. radius $\frac{3}{4}$ in. radius $1\frac{1}{2}$ in. radius

WMS 2, 4, 5 and 8

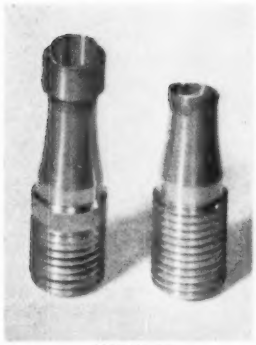

WMS 20
Ring glued to test section

Above and left:

FIGURE 14. Effect of stress gradient on crack propagation under fatigue in D.T.D. 683.

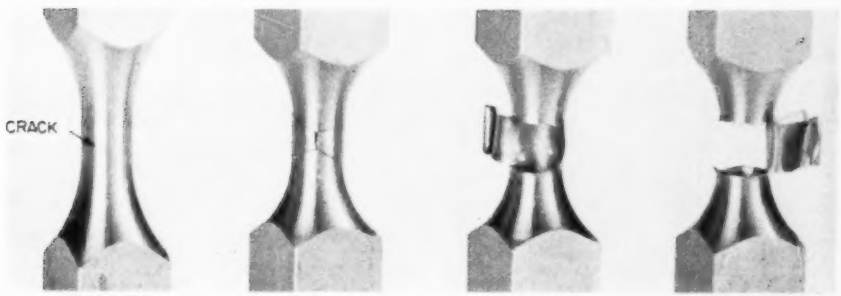

BNZ 2 F 10
Hoop stress 55%
Range of torsion stress 85%

BNZ 2 F 7
Hoop stress 70%
Range of torsion stress 105%

BNZ 2 F 8
Hoop stress 80%
Range of torsion stress 125%

BNZ 2 F 9
Hoop stress 75%
Range of torsion stress 85%

FIGURE 15. Fatigue cracks under alternating torsion and static hoop tension in mild steel.

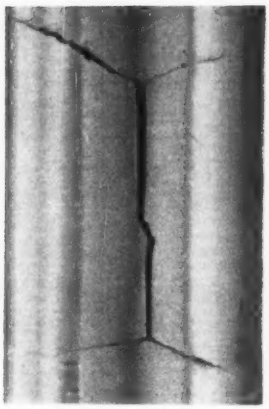

B.S. L 65
(VCG 17)
Hoop stress 10%
Range of torsion stress 45%

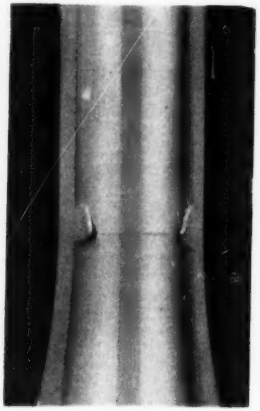

B.S. L 64
(VCH 7)
Hoop stress 15%
Range of torsion stress 45%

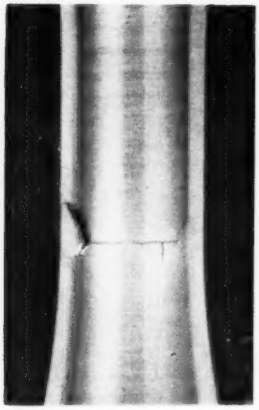

B.S. L 64
(VCH 12)
Hoop stress 15%
Range of torsion stress 45%

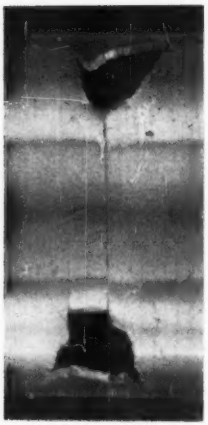

B.S. L 65
(VCG 14)
Hoop stress 15%
Range of torsion
stress 45%

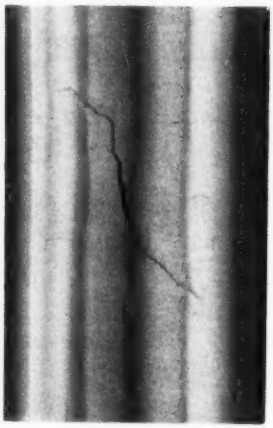

B.S. L 64
(VCH 11)
Hoop stress 30%
Range of torsion stress 45%

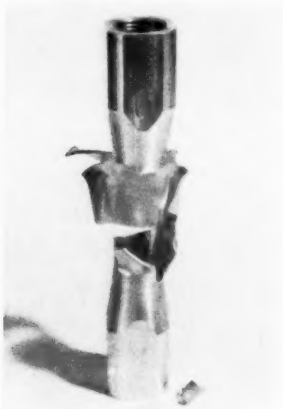

B.S. L 64
(VCH 10)
Hoop stress 50%
Range of torsion stress 45%

FIGURE 13. Fatigue cracks under alternating torsion and static hoop tension.

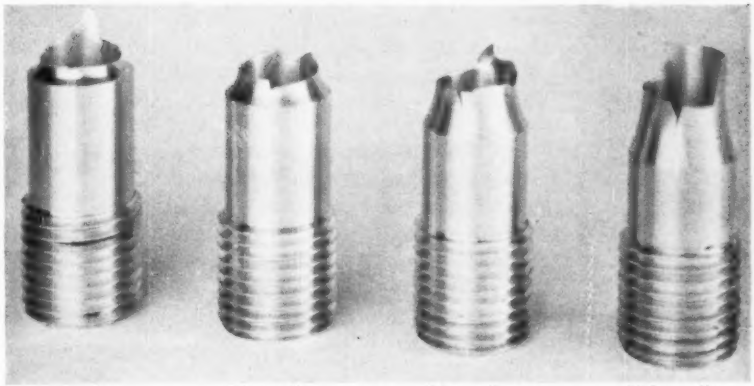

$\frac{1}{8}$ in. radius $\frac{1}{4}$ in. radius $\frac{1}{2}$ in. radius $1\frac{1}{2}$ in. radius

WMS 2, 4, 5 and 8

WMS 20
Ring glued to test section

Above and left:

FIGURE 14. Effect of stress gradient on crack propagation under fatigue in D.T.D. 683.

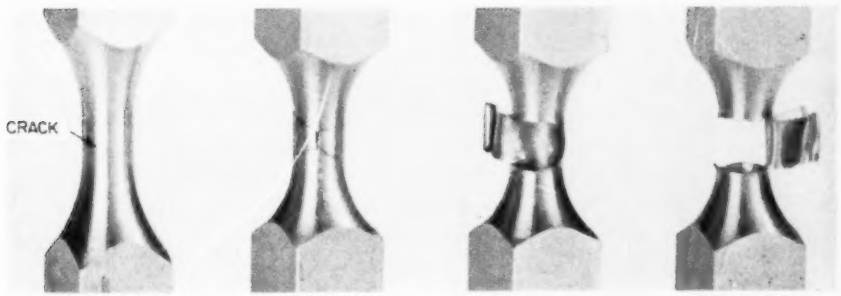

BNZ 2 F 10
Hoop stress 55%
Range of torsion stress 85%

BNZ 2 F 7
Hoop stress 70%
Range of torsion stress 105%

BNZ 2 F 8
Hoop stress 80%
Range of torsion stress 125%

BNZ 2 F 9
Hoop stress 75%
Range of torsion stress 85%

FIGURE 15. Fatigue cracks under alternating torsion and static hoop tension in mild steel.

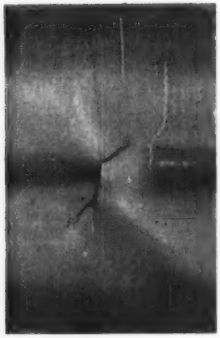

Left:
BNZ 2 F 17
No hoop stress
Range of torsion stress 65%

Right:
BNZ 2 F 22
No hoop stress
Range of torsion stress 75%

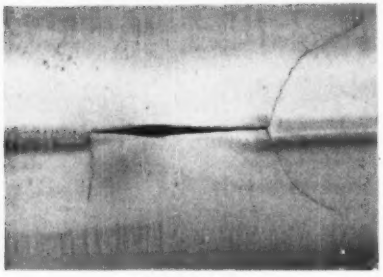

BNZ 2 F 21
Hoop stress 65%
Range of torsion stress 45%

BNZ 2 F 13
Hoop stress 65%
Range of torsion stress 55%

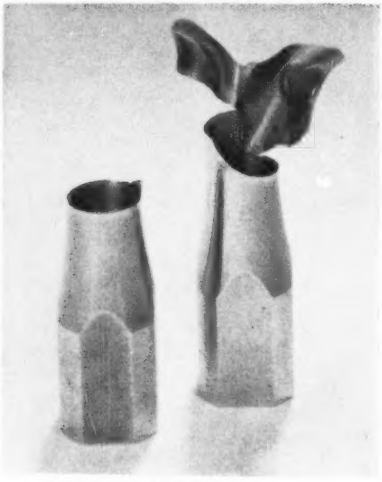

BNZ 2 F 23
Hoop stress 70%
Range of torsion stress 55%

Right:
L is the total length of the axial crack

BNZ 13 F 5
Hoop stress 50%
Range of torsion stress 75%

FIGURE 16. Fatigue cracks under alternating torsion in mild steel with and without static hoop tension.

Accordingly, in tubes under internal pressure, the first fatigue crack, if it develops rapidly enough, may lead at once to fast fracture under the static loading. In consequence, all the complete failures in the present tests, and in particular the explosive ones, look not unlike failures under internal pressure alone.

However, complete rupture can result under fatigue loading only if the initial fatigue crack develops to a length greater than the unstable length appropriate to the material, the size of the tube and the mean loading applied, before the gas pressure falls to zero. The results of the present tests demonstrate that sufficiently rapid development is possible in both hard and soft materials; they demonstrate further, on the one hand, that the unstable crack length may be quite short, and, on the other, that development of the fatigue crack to this length must be extremely rapid.

The present tests are too few to justify strictly quantitative assessment of these two factors but they do afford some further evidence of a qualitative nature with regard to the effects of surface finish and other metallurgical factors.

Under the conditions of the torsion tests (the hoop tensile stress being twice the axial mean tensile stress), fast fracture would be expected to develop more readily from axial than from circumferential cracks. The finish of the tubular test pieces certainly favoured the latter mode and, in the hard aluminium alloys, the first crack was often circumferential. However, when the internal pressure was high, these circumferential cracks often branched and developed into axial ones; comparison between D.T.D. 683, B.S. L 65 and B.S. L 64 in this respect strongly suggests that metallurgical factors, perhaps associated with the extrusion process, may be responsible for this tendency. In the mild steel pieces of $\frac{5}{8}$ in. diameter, circumferential cracks developed in all tests made without a hoop stress, whereas with a hoop stress the cracks were mainly axial.

Once an axial crack has got going, only an abrupt change of section will stop it spreading, but a glued-on ring is equally as effective as a small radius fillet. The concentration of stress at such abrupt change of section may reduce the fatigue endurance, but the resulting crack will be circumferential and, accordingly, far less likely to lead to catastrophic failure.

It remains to comment on the results of the tests on the material to D.T.D. 683 under alternating torsion, which are particularly disquieting. Even without mean stresses due to internal pressure, the fatigue resistance to this form of loading was much lower than the estimate based on the fatigue resistance under direct stress or in bending; when biaxial mean stresses were imposed, fatigue failures resulted under ranges of shear stress as low as $\pm 1{\cdot}8$ tons/in.^{2}

The fatigue resistance of material to B.S. L 65 under alternating torsion is also low by comparison with its resistance to direct or bending stresses but, in this material, biaxial mean stress did not materially affect the strength at long endurances, although the endurances at high stresses were appreciably reduced.

From the literature it certainly appears that the fatigue resistance of the hard aluminium alloys under alternating torsion is often low by comparison with their

resistance under alternating bending, ratios as low as 0·4 having been reported; but the reasons for this weakness seem not to have been explored.

To supplement the evidence presented here, further tests under alternating torsion have been made on two further samples of material to D.T.D. 683 in tubular form and on solid pieces of all three materials. The results so far indicate that, in tubular form, all three sources of material are equally poor and that their low strength is still further reduced by biaxial stresses imposed by internal pressure. One of the materials also gave much the same results when tested in the form of solid bar, whereas the material VCF and the third material in solid bar form exhibited under alternating torsion a resistance fully concordant with their resistance under alternating bending.

The differences in behaviour do not appear to be due to differences in surface finish, but it is possible that they may be due to internal stresses. However, this explanation seems likely to prove satisfactory only if the high fatigue resistance in solid bar form is attributable to compressive mean stresses in the surface layers. Accordingly, it appears probable on the evidence at present available that the fatigue resistance of the hard aluminium alloys under alternating shear stresses may prove abnormally low when the planes subjected to maximum shear are also subjected to static tensile stresses.

ACKNOWLEDGMENTS

The work described in this paper has been carried out as part of the research programme of the National Physical Laboratory and is published by permission of the Director of the Laboratory.

The authors wish to acknowledge the assistance rendered by Mr. J. W. Casemore, who carried out most of the fatigue tests.

Appendix I

UNSTABLE CRACK LENGTH IN A TUBE

1. *Increase of Hoop Tension at the Ends of an Axial Slit*

When an axial slit of length a is made in the wall of a tube, of radius R and wall thickness t, which is under internal pressure p, the circumferential tension, originally $f_0 = p(R/t)$ everywhere, is reduced to zero at the edges of the slit. It follows that the mean circumferential tension in the way of the slit is reduced by λf_0, where λ is some ratio between 0 and 1 which must tend to zero with the ratio a/R.

By analysis of the diffusion of loading applied along the edges of the slit outlined in Appendix II, it appears reasonable to assume $\lambda = \mu(a/R)$, where the factor μ is about 1/8.

The internal pressure being everywhere maintained at the value p, over the segment of the tube in the way of the slit, a part $\mu(a/R)p$ of the total pressure is then unbalanced by circumferential tension and each of the sections of the tube through the ends of the slit

are subjected to shear loading $F=\frac{1}{2}\mu\,(a/R)\,pa$ and bending moment $M=1/[12\mu\,(a/R)\,pa^2]$ per unit length distributed uniformly* round the perimeter. These loadings give rise to an extra circumferential tension f_a in these sections where (*see* Appendix III)

$$f_a=[2{\cdot}6F\,(Rt)^{-1/2}+3{\cdot}3M\,(Rt)^{-1}]\,(R/t).$$

Substituting for F and M, and writing f_0 for pR/t,

$$\frac{f_a}{f_0}=\frac{1}{8}\left(\frac{t}{R}\right)^{1/2}\theta^2\,(1{\cdot}3+0{\cdot}3\theta), \qquad . \quad . \quad . \quad . \quad (1)$$

where $\theta=a/(Rt)^{1/2}$.

2. *Effect of Stiffening and of the Periodic Components of Stresses Due to the Slit*

If the tube is stiffened by sturdy rings closely adjacent to the ends of the slit, both shear loading and bending moment may be virtually annulled and f_a may be reduced almost to zero. Similarly, closely spaced sturdy stringers would tend to reduce the bending moment but, in practical constructions, the influence of the stringers is likely to be far less than the effect of the rings. On the other hand, the effect of the stringers may be more or less independent of the position of the slit, whereas the rings will have but slight effect unless the ends of the slit are fairly close to them, say, within a distance $2\,(Rt)^{1/2}$.

The mean radial shear loading F and mean bending moment M are, of course, only the first (constant) terms in Fourier series which would represent the total loading on the outer parts of the tube arising from the disturbance of stress in the way of the slit; and, of course, the periodic terms in these series also give rise to stresses in the outer parts. However, the heart of plate stresses arising from the periodic terms are mainly shear stresses on the axial and circumferential sections and these terms do not contribute at all to the mean hoop tension (or rather their contribution is only second order). Moreover, the bending strains in the tube walls arising from the periodic terms are limited by their association with shear strains in the plane of the wall, and the bending stresses will be further limited by the stiffeners. In short, the stresses arising from the periodic terms are not likely to be very great and, in any case, these periodic terms do not affect the value of f_a.

3. *Interpretation and Application of Formula* (1)

Formula (1) represents the increase of nominal circumferential tension at the ends of the slit due simply to the curvature of the tube; if R is infinite, f_a is zero. Whereas the nominal tension at the ends of the slit in a flat plate would be f_0, in a tube it is f_0+f_a.

The actual local concentration of stress at the ends of the slit is probably much the same in both flat plate and tube, at least if R/t is of order 100. Therefore, in comparing the results of tests on plates and tubes, it may be expected that the tube subjected to f_0 will behave as a flat plate subjected to f_0+f_a.

However, sufficient information on flat plates is not available, nor would it be easy to compile reliable data for flat plates wide enough for the edge effect to be disregarded. Accordingly, it is more profitable to ignore the flat plate and to apply formula (1) to compare tubes of several sizes on the assumption that unstable crack length depends simply on the attainment of some critical value of f_0+f_a; or, assuming f_0 to be kept constant, on some critical value of f_a/f_0. Values of unstable crack length a_c computed in this way are shown in Table XI for three values of f_a/f_0 and for five sizes of tube.

*See the second paragraph of this Appendix.

The first and third examples relate to tubes tested at Bristol Aircraft Limited, the fifth and sixth examples relate to tubes tested at the N.P.L.; the second and fourth examples are included to illustrate the variation of a_c with t.

TABLE XI

UNSTABLE CRACK LENGTHS (a_c IN INCHES)

f_a/f_0	0·5	1·0	2·0
$R=72,\ t=0{\cdot}040$	12	15·5	20
$R=72,\ t=0{\cdot}064$	13·5	18	23
$R=22,\ t=0{\cdot}040$	5	7	9
$R=22,\ t=0{\cdot}064$	6	8	10·5
$R=0{\cdot}31,\ t=0{\cdot}015$	0·20	0·27	0·35
$R=0{\cdot}125,\ t=0{\cdot}005$	0·075	0·10	0·13

Appendix II

Relief of Mean Hoop Tension in a Segment of Slit Tube

Taking axes Ox circumferentially and Oy axially through the centre of the slit, the stress system in the unstiffened tube may be represented in the form

Circumferential stress, $f_x = \Sigma\,(A\cosh \alpha y + B\alpha y \sinh \alpha y)\sin \alpha x.$

Shear stress, $q = -\Sigma\,[(A-B)\sinh \alpha y + B\alpha y \cosh \alpha y]\cos \alpha x.$

Axial stress, $f_y = -\Sigma\,[(A-2B)\cosh \alpha y + B\alpha y \sinh \alpha y]\sin \alpha x.$

Here $\alpha = n/(2R)$ and the summations are over all odd values of n.

The average circumferential stress, f_{av}, across the axial section at x of the segment comprising the slit is

$$f_{av} = \frac{2}{a}\int_0^{a/2} f_x\,dy = -\frac{2}{a}\int_0^{x} q\,dx = \sum\left[(A-B)\frac{S}{\theta} + BC\right]\sin \alpha x$$

where $\theta = na/(4R)$, $C = \cosh\theta$ and $S = \sinh\theta$.

The average value of f_{av} round the whole perimeter of the tube is

$$f_{av} = \frac{1}{2\pi R}\int_0^{2\pi R} f_{av}\,dx = \frac{2}{\pi}\sum\frac{1}{n}\left[(A-B)\frac{S}{\theta} + BC\right]$$

If we assume $f_y = 0$ and $f_x = f$ (constant) at $y = \pm\,(a/2)$, $AC = B\,(2C - \theta S)$ and $AC + B\theta S = (4/\pi n)\,f$, and it follows that

$$\frac{f_{av}}{f} = \frac{8}{\pi^2}\sum\frac{1}{2n^2}\left(\frac{T}{\theta} + 1 - T^2\right), \quad \text{where } T = \tanh\theta.$$

Evaluation of the series for values of (a/R) from 0 to 1·5 indicates that

$$1-\frac{f_{av}}{f}=\frac{1}{8}\frac{a}{R}.$$

Other, perhaps more reasonable, assumptions with regard to the conditions at the sections through the ends of the slit would, of course, result in a different relationship; but the analysis outlined here may suffice to justify the assumption that the relief of mean hoop tension in the way of the slit varies linearly with a/R and to indicate the order of the constant of proportionality.

Appendix III

HOOP TENSION SET UP AT THE END OF A LONG TUBE BY SHEAR LOADING AND BENDING MOMENT APPLIED UNIFORMLY ALL ROUND THE END SECTION

The differential equation governing the radial displacement y at the section distant x from one end of a tube of radius R and thickness t ($t \ll R$) under circularly symmetrical loading is

$$\frac{d^4y}{dx^4}+\frac{12(1-\sigma^2)y}{R^2t^2}=0,$$

of which the solution appropriate to a long tube loaded at one end only is

$$y=e^{-\alpha x}(A\cos\alpha x+B\sin\alpha x),$$

where $\alpha^4=(1-\sigma^2)/R^2t^2$.

Under shear loading F and bending moment M per unit width applied over the whole section at $x=0$,

$$A=6(F+M\alpha)/(E'\alpha^3t^3) \quad \text{and} \quad B=-6M/(E'\alpha^2t^3),$$

where $E'=E/(1-\sigma^2)$.

Then, at $x=0$, $y=A$

and the hoop tension $f=Ey/R=6(1-\sigma^2)(F+M\alpha)/(R\alpha^3t^3)$.

Or, substituting for α and taking $\sigma=0{\cdot}3$,

$$f=[2{\cdot}6F(Rt)^{-1/2}+3{\cdot}3M(Rt)^{-1}](R/t).$$

The Vibration of Air in a Duct with a Subsonic Mean Flow

D. S. WHITEHEAD

(*University Engineering Laboratory, Cambridge*)

SUMMARY: The effect of a subsonic mean flow on the organ-pipe type of vibration of the air in a duct of uniform area is calculated. The flow at entry to the duct is assumed to be at constant stagnation pressure, and a range of exit conditions is considered. It is found that the effect of the mean flow is to reduce the resonant frequencies by a factor of $(1-M^2)$ (where M is the Mach number in the duct) and to introduce damping of the vibration. Except when the duct is terminated by an efficient diffuser, this damping is rather large and it would require a powerful driving mechanism to produce large vibrations in the duct.

1. Introduction

The investigation reported in this paper was carried out in connection with a suspected case of severe oscillation (not subsequently confirmed) of the air in the intake duct of a jet engine installation. It was required to find out what the effect of the mean flow would be on the organ-pipe type of vibration of the air in the duct. Similar situations occur in the combustion chambers and jet pipes of jet engines, and in the combustion chambers of rocket motors.

The system to be analysed is shown in Fig. 1. A duct of uniform cross-sectional area is fed at constant stagnation pressure from an atmosphere through a short contraction. The duct is terminated by an area change leading to a large vessel in which the static pressure is maintained constant. Small oscillations of the air in the duct are considered and, in order to obtain a solution, it is necessary to allow for exponential growth or decay of the oscillations. The system is assumed to be one-dimensional and fluid friction is neglected throughout. The fluid is assumed to be a perfect gas.

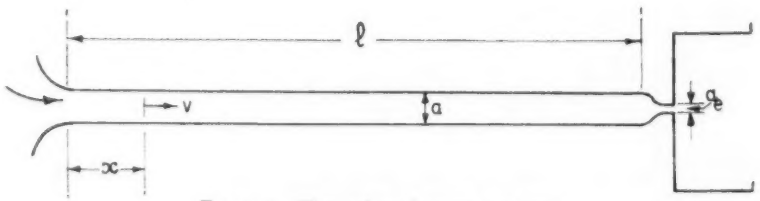

FIGURE 1. Illustration of system analysed.

Received December 1960.

NOTATION

A, B arbitrary constants

$M = U/c$, mean Mach number in duct

M_e mean Mach number at exit

T temperature

U mean velocity of flow in duct

a area of duct

a_e area of exit

c mean speed of sound in duct

c_p specific heat at constant pressure

$i = \sqrt{(-1)}$, indicates component leading 90° in phase

k constant given by equation (16)

l length of duct

n integer ($n \geqslant 1$)

p static pressure

s a measure of density variation

t time

u a measure of velocity variation

v velocity of fluid in duct

x distance along duct

α amplification factor

γ ratio of specific heats of fluid

δ logarithmic decrement

ρ fluid density in duct

ρ_0 mean fluid density in duct

ω angular frequency of oscillations.

2 Analysis of Flow in Duct

The equation of continuity for flow in a duct of constant area is

$$\frac{\partial}{\partial x}(\rho v) + \frac{\partial \rho}{\partial t} = 0. \quad . \quad . \quad . \quad . \quad (1)$$

The equation of motion in the x-direction is

$$\frac{\partial v}{\partial t} + v\frac{\partial v}{\partial x} + \frac{1}{\rho}\frac{\partial p}{\partial x} = 0. \quad . \quad . \quad . \quad . \quad (2)$$

Since the flow is reversible and adiabatic, and the fluid is a perfect gas,

$$\frac{p}{\rho^\gamma} = \text{constant} \quad . \quad . \quad . \quad . \quad (3)$$

and the speed of sound is given by

$$c^2 = \frac{\gamma p}{\rho} \quad . \quad . \quad . \quad . \quad . \quad . \quad . \quad (4)$$

Eliminating the pressure variation from (2) and (3), and using (4), gives

$$\frac{\partial v}{\partial t} + v\frac{\partial v}{\partial x} + \frac{c^2}{\rho}\frac{\partial \rho}{\partial x} = 0. \quad . \quad . \quad . \quad . \quad (5)$$

It is now supposed that ρ and v vary with time in the following way: —

$$\left.\begin{aligned} \rho &= \rho_0 \left[1 + s e^{(\alpha + i\omega)t}\right] \\ v &= U \left[1 + u e^{(\alpha + i\omega)t}\right] \end{aligned}\right\}, \quad . \quad . \quad . \quad . \quad (6)$$

where ρ_0 and U are constants, and s and u are functions of x only and are small quantities. The time variation represents oscillations with angular frequency ω with an exponential growth or decay given by the factor α.

Substituting equations (6) into equations (1) and (5), and neglecting terms of second order in small quantities, gives

$$\frac{du}{dx} + \frac{ds}{dx} + \frac{\alpha + i\omega}{U} s = 0, \quad . \quad . \quad . \quad . \quad (7)$$

$$\frac{\alpha + i\omega}{U} u + \frac{du}{dx} + \frac{c^2}{U^2}\frac{ds}{dx} = 0. \quad . \quad . \quad . \quad . \quad (8)$$

Writing D for d/dx, and eliminating s between these two equations, gives

$$\left(D + \frac{\alpha + i\omega}{U}\right)^2 u - \frac{c^2}{U^2} D^2 u = 0$$

$$\text{or} \quad \left\{D\left(1 - \frac{c}{U}\right) + \frac{\alpha + i\omega}{U}\right\}\left\{D\left(1 + \frac{c}{U}\right) + \frac{\alpha + i\omega}{U}\right\} u = 0.$$

The solution of this equation is

$$u = A e^{\frac{(\alpha + i\omega)}{1 - M}\frac{x}{c}} + B e^{-\frac{(\alpha + i\omega)}{1 + M}\frac{x}{c}}, \quad . \quad . \quad . \quad (9)$$

where $M = U/c$, and A and B are arbitrary constants.

Substituting (9) into (8) gives the corresponding solution for s,

$$s = -AM\,e^{\frac{(\alpha+i\omega)}{1-M}\frac{x}{c}} + BM\,e^{-\frac{(\alpha+i\omega)}{1+M}\frac{x}{c}}. \quad . \quad . \quad (10)$$

The first terms in equations (9) and (10) represent a wave travelling backwards at a speed $c(1-M)$, *i.e.* at sonic speed relative to the fluid. The second terms represent a wave travelling forwards at a speed $c(1+M)$.

3. End Conditions

Consider first the end conditions to be applied at the exit from the duct. It is supposed that the area change takes place over a very short length of duct, so that conditions over this short length can be regarded as though they were steady. Conditions at the end of the duct will be denoted by the suffix " 2 " and at the exit after the area change by suffix " e." Since the static pressure at the exit, p_e, is fixed and the whole flow is isentropic, the state of the fluid at exit is fixed and T_e and ρ_e are constants.

By continuity,

$$\rho_2 a_2 v_2 = \rho_e a_e v_e. \quad . \quad . \quad . \quad . \quad . \quad . \quad (11)$$

From energy considerations,

$$T_2 + \frac{v_2^2}{2c_p} = T_e + \frac{v_e^2}{2c_p} \quad . \quad . \quad . \quad . \quad . \quad . \quad (12)$$

and for isentropic flow of a perfect gas

$$\frac{T_e}{T_2} = \left(\frac{\rho_e}{\rho_2}\right)^{\gamma-1} \quad . \quad . \quad . \quad . \quad . \quad . \quad (13)$$

Eliminating v_e and T_2 from equations (11), (12) and (13) gives

$$\frac{v_2^2}{2c_p T_e} = \frac{1-\left(\frac{\rho_2}{\rho_e}\right)^{\gamma-1}}{1-\left(\frac{a_2}{a_e}\right)^2\left(\frac{\rho_2}{\rho_e}\right)^2} \quad . \quad . \quad . \quad . \quad . \quad (14)$$

This equation is the required relationship between v_2 and ρ_2, since all the other quantities appearing in the equation are constants. Substituting for ρ_2 and v_2 from equations (6), and picking out terms of first order in small quantities, gives the corresponding relationship between u and s in the form

$$u = ks. \quad . \quad . \quad . \quad . \quad . \quad . \quad (15)$$

If the constant k is expressed in terms of Mach numbers, it is found after some manipulation that

$$k=\frac{\left(1+\frac{\gamma-1}{2}M_e^2\right)-M_e^2\left(1+\frac{\gamma-1}{2}M^2\right)}{M_e^2-M^2} \quad . \quad . \quad . \quad (16)$$

This is the required end condition at the outlet end of the duct. Three special cases are of interest.

(*i*) If $M_e=0$ then $u=-s/M^2$. This is the case when the duct is fitted with an ideal diffuser of very large area ratio, so that the stagnation pressure at duct exit is constant.

(*ii*) If $M_e=M$ then $s=0$. In this case there is no area change at duct exit, so that the static pressure at duct exit is constant.

(*iii*) If $M_e=1$ then $u=\frac{1}{2}(\gamma-1)s$. In this case the duct is terminated by a choked nozzle.

At entry to the duct the assumed condition is one of constant stagnation pressure. This corresponds to the special case (*i*), so that at entry

$$u=-\frac{s}{M^2} \quad . \quad . \quad . \quad . \quad . \quad . \quad . \quad (17)$$

4. Solution

Applying the outlet condition (15) to equations (9) and (10) when $x=0$ gives

$$A+B=-\frac{1}{M}(-A+B),$$

$$\text{or} \quad \frac{A}{B}=\frac{1+M}{1-M} \quad . \quad . \quad . \quad . \quad . \quad . \quad (18)$$

Applying the outlet condition (15) to equations (9) and (10) when $x=l$ gives

$$Ae^{\frac{(\alpha+i\omega)}{1-M}\frac{l}{c}}+Be^{-\frac{(\alpha+i\omega)}{1+M}\frac{l}{c}}=kM\left\{-Ae^{\frac{(\alpha+i\omega)}{1-M}\frac{l}{c}}+Be^{-\frac{(\alpha+i\omega)}{1+M}\frac{l}{c}}\right\} \quad . \quad (19)$$

Eliminating the ratio A/B from equations (18) and (19) gives

$$e^{\frac{\alpha+i\omega}{1-M^2}\frac{2l}{c}}=-\frac{(1-M)(1-kM)}{(1+M)(1+kM)} \quad . \quad . \quad . \quad (20)$$

The real and imaginary parts of this equation must both be satisfied.

Hence
$$e^{\frac{2\alpha l}{c(1-M^2)}} \cos\frac{2\omega l}{c(1-M^2)} = -\frac{(1-M)(1-kM)}{(1+M)(1+kM)} \quad . \quad . \quad . \quad (21)$$

$$e^{\frac{2\alpha l}{c(1-M^2)}} \sin\frac{2\omega l}{c(1-M^2)} = 0. \quad . \quad . \quad . \quad . \quad . \quad . \quad (22)$$

These two equations enable the two unknowns α and ω to be found. The result depends on the sign of the right-hand side of equation (21).

If $\left\{-\frac{(1-M)(1-kM)}{(1+M)(1+kM)}\right\}$ is positive,

$$\left.\begin{aligned} \text{then} \quad & \frac{2\omega l}{c(1-M^2)} = 2\pi n \\ \text{and} \quad & \frac{2\alpha l}{c(1-M^2)} = \log_e\left\{-\frac{(1-M)(1-kM)}{(1+M)(1+kM)}\right\}. \end{aligned}\right\} \quad . \quad . \quad (23)$$

If $\left\{-\frac{(1-M)(1-kM)}{(1+M)(1+kM)}\right\}$ is negative,

$$\left.\begin{aligned} \text{then} \quad & \frac{2\omega l}{c(1-M^2)} = (2n-1)\pi \\ \text{and} \quad & \frac{2\alpha l}{c(1-M^2)} = \log_e\frac{(1-M)(1-kM)}{(1+M)(1+kM)}. \end{aligned}\right\} \quad . \quad . \quad (24)$$

In each case n is an integer ($n \geqslant 1$) which determines the various modes of the system.

The solution (23) includes the special cases ((*i*) and (*ii*) in Section 3) of constant outlet stagnation pressure and static pressure, and the result is analogous to the standard solution for an organ pipe open at both ends. The solution (24) includes the special case ((*iii*) in Section 3) of a choked exit, and is analogous to an organ pipe open at one end and closed at the other.

It will be seen that, in both solutions, one effect of the uniform flow in the duct is to drop the frequency from the standard organ pipe value by the factor $(1-M^2)$. This simply represents the extra time taken for a wave to travel from one end of the duct to the other and back again.

The other effect of the uniform flow is to introduce damping of the oscillations. This is probably best specified by the usual logarithmic decrement δ, which is related to the quantity α as follows:—

$$\delta = -2\pi\alpha/\omega. \quad . \quad . \quad . \quad . \quad . \quad (25)$$

For the solution (23) this is given by

$$n\delta = \log_e\left\{-\frac{(1+M)(1+kM)}{(1-M)(1-kM)}\right\}. \quad . \quad . \quad . \quad (26)$$

For the solution (24) it is given by

$$\frac{2n-1}{2}\delta = \log_e \frac{(1+M)(1+kM)}{(1-M)(1-kM)} \cdot \quad . \quad . \quad . \quad . \quad . \quad (27)$$

These equations are illustrated in Fig. 2 (for $\gamma = 1{\cdot}4$). The full line is the boundary between the two solutions (given by $kM = 1$) and also corresponds to infinitely great damping of the oscillations. Below this are shown broken lines of constant values of $n\delta$, calculated from equation (26). Similarly, above the full line are shown broken lines of constant values of $\frac{1}{2}(2n-1)\delta$, calculated from equation (27). This diagram therefore enables the type of solution to be determined and the damping to be estimated for any given values of M and M_e. Constant outlet stagnation pressure conditions lie on the line OP and the damping is zero. Constant outlet static pressure conditions lie on the straight line OQ, and choked outlet conditions lie on the line QR.

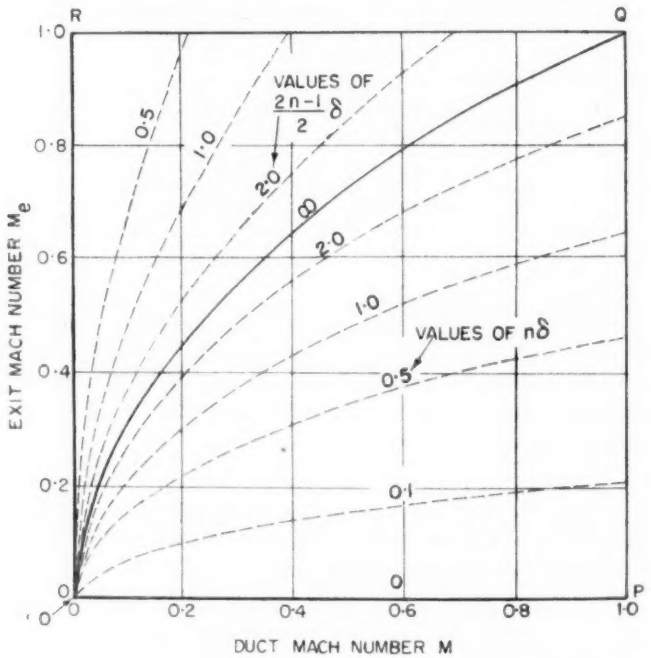

FIGURE 2. Damping of duct vibration.

It can be seen from Fig. 2 that, except when the exit Mach number is low, the damping of the vibrations is high, at least for the lower modes of vibration corresponding to low values of n. It is concluded that vibration of this type would only occur if a very powerful driving mechanism were present. The exceptions to this are cases when the duct is fitted with an efficient diffuser of large area ratio at exit, in which cases vibration might be rather easily excited.

The Effect of Fuel Distribution on Reaction Rates

M. V. HERBERT

(*National Gas Turbine Establishment*)

SUMMARY: Theoretical reaction rate considerations normally require homogeneity of the mixture supply. An attempt—necessarily crude by reason of the analytical difficulties—is made here to cater for the case of non-uniform fuel distribution. Assuming a point-source injector in a parallel pipe, the "loss" in reaction rate is calculated for a limited number of specimen cases.

1. Introduction

Since Longwell's classic experiments with the spherical reactor, much play has been made with homogeneous reaction rate theory using effective "global" constants derived from his data. Such theories ordinarily assume "ideal" conditions both inside and at entry to the reactor, including the supply of perfectly mixed combustibles. These conditions could scarcely be satisfied in a practical system, and often are not even approached. Heat loss from, and imperfect internal mixing in, the reaction zone are inherent in practical designs, and a further departure from the ideal can occur in the mixture entry conditions. The fuel may be incompletely vaporised, incompletely mixed, or both. The case of non-uniform fuel distribution is one for which an attempt may be made to cater analytically in a simple instance. Applications of particular interest are reheat systems and ram-jet pilot burners, where considerable penalty may be suffered by allowing insufficient distance between fuel injection and stabiliser for full diffusion. In such cases, interest is mainly in the stoichiometric condition, and it is that to which most attention has been given here.

NOTATION

A cross-sectional area of duct (ft.^{2})

C concentration of fuel in air (lb./lb.)

e turbulent diffusivity (ft.^{2}/sec.)

P pressure (atmospheres)

Q air mass flow (lb./sec.)

Q_f overall fuel flow (lb./sec.)

Received November 1960.

r radius from centre line of duct (ft.)

V reaction volume (ft.^{3})

v air velocity (ft./sec.)

y distance downstream from source (ft.)

δ weight fraction of air mass flow at given mixture strength

ε combustion efficiency

ρ air density (lb./ft.^{3})

ϕ equivalence ratio $= \dfrac{\text{fuel/air ratio}}{\text{stoichiometric fuel/air ratio}}$

Suffixes

m overall weight mean

0 centre line

w wall

A prime (′) denotes infinite stream conditions.
Other symbols are defined in the text.

2. General Conditions

The hypothetical arrangement considered is a circular duct containing a single central " point-source " fuel injector upstream of a flame-holder (Fig. 1). Conditions in the duct are assumed to be turbulent and uniform, both as to velocity and temperature, and reaction rates are arbitrarily computed for the case of unvitiated air at 500°K. In the case of liquid fuel, it is assumed that diffusion and evaporation take place simultaneously after injection, and the turbulent diffusivity (e) is taken to be an effective one for the state of the fuel at the station considered. It is reasonable

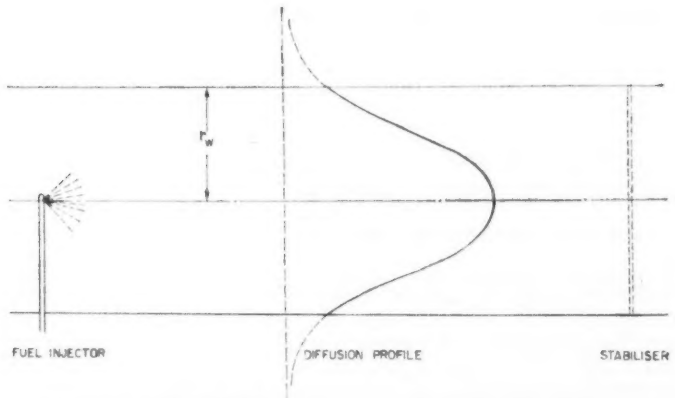

FIGURE 1. Fuel distribution: diagrammatic arrangement of system.

to suppose that, as evaporation proceeds, so e will apparently increase with distance downstream, until evaporation is complete, when it will assume a constant value. In the absence of experimental data for these conditions, we can only take e as fixed, *i.e.* evaporation is assumed to be complete upstream of the flame-holder in each case.

The form of stabiliser shown in Fig. 1 is not a true representation of either a reheat or a ram-jet pilot burner, and we should consider how applicable this analysis will be. In computing an overall reaction rate, it is arbitrarily assumed that the total reaction volume is shared amongst discrete volumina at different mixture strengths so that all reach the same stage of combustion together—*i.e.* all have the same fractional consumption efficiency—and that there is no heat transfer between them. While this is recognised as a quite artificial treatment, it is the most convenient of manipulation in deriving an overall average reaction rate. These conditions will give not only a reduction of reaction rate relative to the homogeneous case, but also a lower mean temperature.

These assumptions may be expected to be most nearly realised in a ram-jet colander burner, as the stability of the whole reaction there is not dependent on propagation from any one particular region and hence on any one set of local conditions. It is more difficult to predict how the performance of a reheat gutter system will respond to an assumed change in fuel distribution; but qualitatively it can be supposed that reduced overall reaction rate will be accompanied by a shift in the peak of the stability loop away from the region of stoichiometric overall towards some weaker mean mixture strength.

It is not intended that the quantitative values derived here should be anything more than illustrative, bearing in mind the limitations in treatment. The order of the effect, however, should be of quite general interest.

3. Fuel Distribution Profiles

The radial concentration gradient at any station distant y downstream of a point source in an infinite stream is given in Ref. 1 as

$$C = \frac{Q_i}{Q} \frac{Av}{4\pi ye} \exp\left[-r^2 v/(4ye)\right] \quad . \quad . \quad . \quad (1)$$

Other conditions being constant, the concentration at radius r is then

$$C = C_0 \exp\left[-(r/k)^2\right] \quad . \quad . \quad . \quad . \quad . \quad (2)$$

where $k^2 = 4ye/v$.

Suppose a wall concentration C_w be defined at radius r_w. Then

$$\frac{C}{C_0} = \left[\frac{C_w}{C_0}\right]^{(r/r_w)^2} \quad . \quad . \quad . \quad . \quad . \quad . \quad (3)$$

A distribution such as that given by equation (3) is indicated in Fig. 1.

In the practical case of a finite duct, some allowance must be introduced for the presence of the duct wall. The method adopted cannot be rigidly defended, but it will presently be shown that the result is reasonably satisfactory. The assumption is here made that equation (3) can be applied to that portion of the profile inside the duct, with r_w as the duct radius. Now we know that the total quantity of fuel across the section is Q_f. If C_m is the overall weight mean concentration, then

$$Q_f = C_m Q$$

$$= C_m \rho v \pi r_w^2.$$

Also,
$$Q_f = \int_0^{r_w} C \rho v \, 2\pi r \, dr.$$

Hence, substituting from equation (3),

$$C_m r_w^2 = 2 \int_0^{r_w} C_0 \left[\frac{C_w}{C_0}\right]^{(r/r_w)^2} r \, dr,$$

$$\text{which gives} \qquad C_m = \frac{C_w - C_0}{\log (C_w/C_0)} \quad . \quad . \quad . \quad . \quad (4)$$

Now it is convenient to work in terms of equivalence ratio (ϕ) in calculation of reaction rates. We know that for the conditions considered

$$C \propto \phi.$$

Thus equation (4) may be rewritten as

$$\phi_m = \frac{\phi_w - \phi_0}{\log (\phi_w/\phi_0)} \quad . \quad . \quad . \quad . \quad . \quad . \quad (5)$$

To avoid introducing particular duct dimensions we define arbitrarily, as an example, a wall condition of $\phi_w = 0{\cdot}5$ for an overall fuel/air ratio given by $\phi_m = 1$ (stoichiometric). Then equation (5) gives

$$\phi_0 = 1{\cdot}76 \qquad \text{on the centre line.}$$

Hence, from equation (3),

$$\phi = \phi_0 \left[\frac{\phi_w}{\phi_0}\right]^{(r/r_w)^2} = \frac{1{\cdot}76}{(3{\cdot}52)^{(r/r_w)^2}} \quad .$$

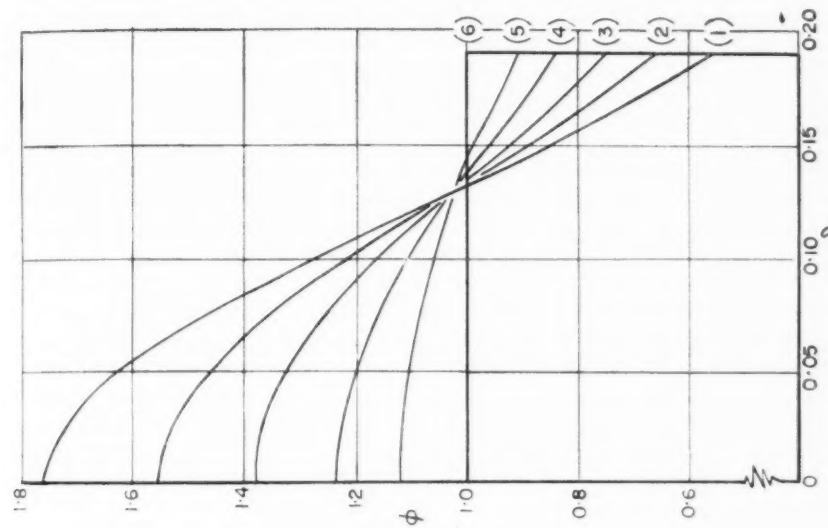

FIGURE 3. Mass mixture proportion curves ($\phi_m = 1$).

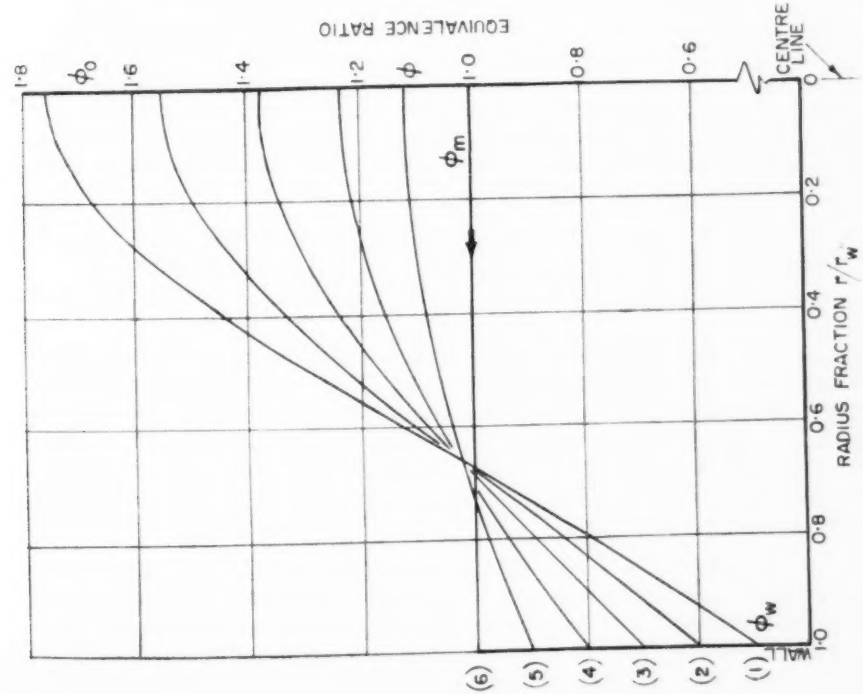

FIGURE 2. Fuel distribution profiles in duct ($\phi_m = 1$).

Plotting this relation gives the profile curve (1) in Fig. 2. Other similar curves are also shown for values of ϕ_w between 0·5 and 1·0, all for the same overall stoichiometric condition. Corresponding to each of these curves in Fig. 2 are those of Fig. 3, giving the proportion of air flow by weight (δ) reaching any mixture strength.

One must now consider how justified is the assumed treatment of wall effects. The infinite stream profile (Fig. 1) is modified in practice by collection of fuel on the wall and diffusion back into the duct, so that the concentration gradient at the wall is zero for equilibrium. For a large duct (or a short distance from the injector) this will lead to a distribution as indicated by the upper curve in Fig. 4(*a*), the thick line denoting the infinite stream profile (ϕ'), and the fuel masses represented by areas *A* and *B* being equal. (*Note*: On the diagram, area $B >$ area *A* because of the changing radius.) No general diffusion equation can take these wall effects into account and, even in a particular case, the treatment of secondary diffusion to give the superposed profile (Fig. 4(*a*)) involves some arbitrary assumptions. The best compromise seems to be the retention of a general relation such as equation (1) (cf. various empirical curves as, for instance, in Ref. 2) deliberately misapplied for convenience.

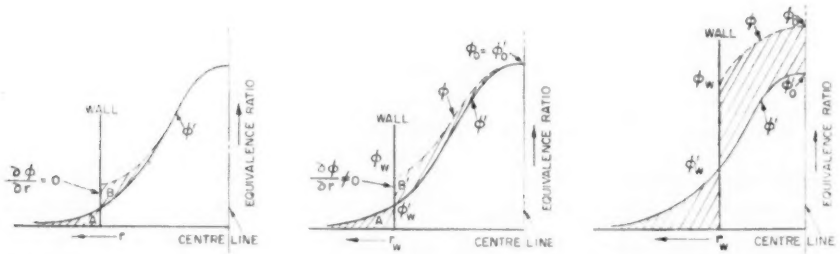

(*a*) True pattern of re-diffusion at wall of duct.

(*b*) Substitute assumed for calculations.

(*c*) Condition as diffusion nears completion.

FIGURE 4. Effect of duct wall on fuel diffusion.

The assumption made that equation (3) may be applied to the whole profile within the duct gives the upper curve of Fig. 4(*b*), which may often be a sufficiently close representation of the true state of affairs, despite the fact that the concentration gradient at the wall is not zero. It would be possible to distort that part of the curve adjacent to the wall to give $\partial\phi/\partial r = 0$ but, for constant fuel mass flow ($\propto \phi_m$) and for a given value of ϕ_o, this would give a new value of ϕ_w bearing no relation to that computed from equation (5).

In any case, the final result is only affected if the steps of radius taken in the subsequent calculations are sufficiently small and, with our use of 10 per cent intervals, it does not seem worth introducing any correction. Concentrating, then, on the method of Fig. 4(*b*) and referring ϕ' to the infinite stream profile, the values of ϕ_w and ϕ_w' are now compared.

For the same overall fuel flow ($\propto \phi_m$),

$$\int_0^{r_w} \phi r\, dr = \int_0^{\infty} \phi' r\, dr.$$

Substituting again from equation (3), this yields

$$\frac{\phi_w}{\phi_o} = \left| \frac{\phi_w'}{\phi_o'} \right|^{(\phi_o - \phi_w)/\phi_o'} \qquad (6)$$

Applying this to the previous example in which $\phi_w = 0{\cdot}5$, and for which (following Fig. 4(*b*)) we can write

$$\phi_o = \phi_o' = 1{\cdot}76,$$

we get $\phi_w' = 0{\cdot}33$, which seems a reasonable value. Hence the method is deemed to be acceptable for the present purpose and has been used to produce the curves of Figs. 2 and 3 already described.

For a more even distribution, as occurs at a long distance from the injector, it is no longer permissible to write $\phi_o = \phi_o'$, as the picture becomes like Fig. 4(*c*). This is the result of successive re-diffusion from the wall to the centre line and back. In this régime there is no real justification for continuing to use part of an infinite stream profile (given by equation (3)) in the manner previously assumed. Since, however, the actual shape of the distribution profile becomes relatively unimportant as complete diffusion is approached, the method has been retained for convenience.

4. Reaction Rate Calculation

For a given fuel distribution profile, an assessment of local reaction rate has been made over a series of radial steps, using the mass mixture proportions shown in Fig. 3. For each step the method of Ref. 3 was used to find the local value of air loading. This is defined in terms of the group $Q/(VP^2)$, being a function of equivalence ratio and inlet temperature, and dependent on combustion efficiency. At efficiencies of 100 per cent and close to zero the value of air loading is zero, and a peak loading is reached at some efficiency usually around 80 per cent. This peak corresponds to combustion extinction or "blow-out", as stable operation is only possible, in general, when the gradient is such that an increase in loading can be met by a decrease in efficiency.

As mentioned earlier, each radial step is treated as a separate adiabatic and homogeneous entity without influence on its neighbours, and it has been further assumed, purely for convenience, that the same level of combustion efficiency is reached simultaneously in each step. Thus a curve of aggregate reaction rate against efficiency can be obtained for each fuel distribution pattern.

Defining local conditions by

$$\begin{cases} \delta = \text{weight fraction of air mass flow at state } \phi \\ \Delta V = \text{volume required for reaction of mass } \delta Q \\ Y = \text{air loading of volume } \Delta V = \dfrac{\delta Q}{\Delta V P^2}, \end{cases}$$

we know that $\Sigma\,|\Delta V| = V$ and $\Sigma\,|\delta| = 1{\cdot}0$,

whence $$V = \Sigma \left| \frac{\delta Q}{Y P^2} \right| = \frac{Q}{P^2} \Sigma \left| \frac{\delta}{Y} \right|$$

or $$\frac{Q}{VP^2} = \frac{1}{\Sigma \left| \dfrac{\delta}{Y} \right|} \qquad \ldots\ldots\ldots\ldots \quad (7)$$

This result is shown in Fig. 5, corresponding to the distributions in Figs. 2 and 3, all for $\phi_m = 1$. Fig. 6 gives the blow-out conditions taken from Fig. 5, from which it can be seen that in the worst case considered the "loss" of air loading is 75 per cent.

Since maximum reaction rates occur close to the stoichiometric condition, and fall off rapidly on either side, distributions such as those in Fig. 2 must naturally be expected to result in overall losses. It seemed possible, however, that at some other value of ϕ_m the fractions of mixture nearer the stoichiometric condition might balance the effect of those further away. To check this, a single case has been worked out for $\phi_m = 0{\cdot}75$, with the distribution shown in Fig. 7. The result is given in Fig. 8, from which it is clear that the large mass of mixture at conditions less than ϕ_m has far outweighed the existence of a local stoichiometric region, and that no "gain" in reaction rate is possible.

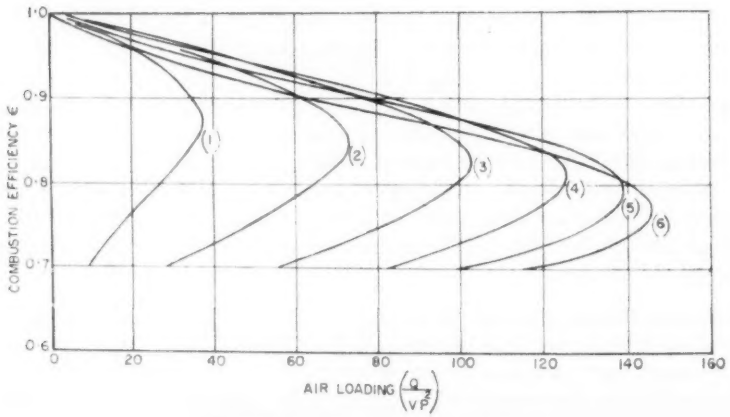

FIGURE 5. Reaction rate curves ($\phi_m = 1$).

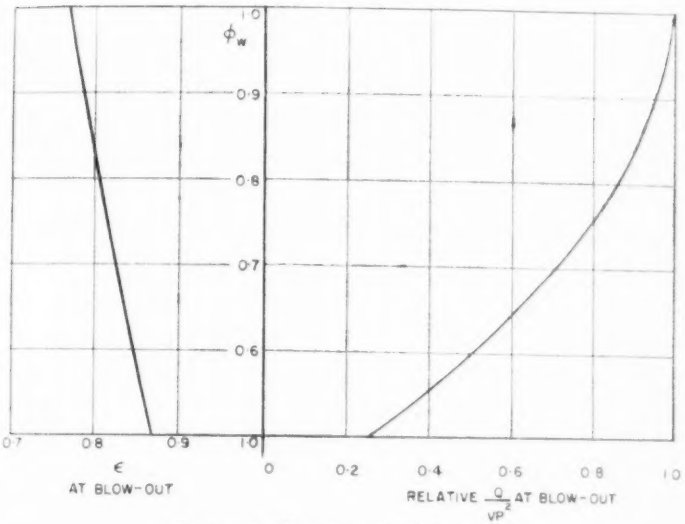

FIGURE 6. Blow-out conditions ($\phi_m = 1$).

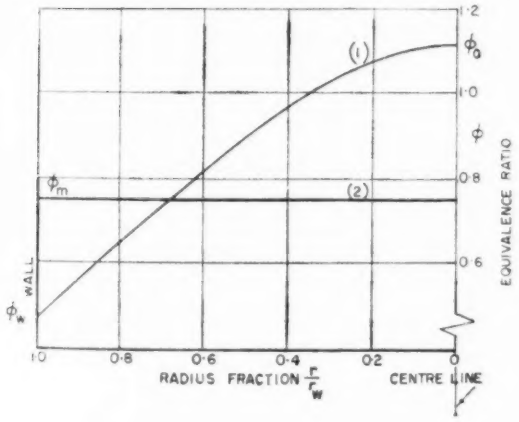

FIGURE 7. Fuel distribution profile ($\phi_m = 0{\cdot}75$).

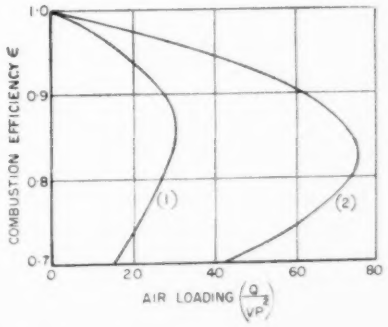

FIGURE 8. Reaction rate curves ($\phi_m = 0{\cdot}75$).

It is of interest to compare the relative blow-out loading at $\phi_m = 0{\cdot}75$ (from Fig. 8, we have 41 per cent of the uniform distribution case) with an appropriate value at $\phi_m = 1$. Making the assumption that the value of e is unchanged, which is experimentally valid for downstream injection, equation (1) leads to

$$\phi_o \propto \phi_m. \quad . \quad . \quad . \quad . \quad . \quad . \quad . \quad (8)$$

Hence, scaling the value of ϕ_0 from Fig. 7 in the ratio of ϕ_m, we have that

$$\text{at} \quad \phi_m = 1, \quad \phi_o = 1{\cdot}49,$$

at which condition Fig. 2 gives $\phi_w = 0{\cdot}63$. A value of 57 per cent relative loading may then be taken from Fig. 6 for comparison with the 41 per cent obtained previously.

The implication is, then, that there is no substantial change in the absolute value of " loss " throughout the range of overall mixture strength. A stability loop—in terms of air loading and equivalence ratio—would be shifted, but not apparently blunted. This conclusion is necessarily tentative, because of the crudity of the analysis, but may be of some interest. Several practical combustion systems, operating with less perfect uniformity of conditions than Longwell's spherical reactor, have produced stability loops much blunter than this, and differences in fuel distribution might have been a contributory cause.

5. Conclusion

A tentative method has been used to plot the fuel distribution in a finite duct. The reaction rate has been calculated for a number of cases with an overall stoichiometric mixture, and the "loss" due to uneven distribution is found to be 75 per cent in the worst case considered. From limited work at other conditions, it is thought that no significant change in the shape of a stability loop should result from fuel distribution alone.

Acknowledgment

This paper is based on work done at the National Gas Turbine Establishment during 1956 and is published by permission of the Director. The illustrations are Crown Copyright.

References

1. Beeton, A. B. P. A Theoretical Expression for Point-Source Diffusion in Turbulent Flow. Unpublished Ministry of Supply Paper, March 1954.

2. Forstall, W. and Shapiro, A. H. Momentum and Mass Transfer in Coaxial Gas Jets. *Journal of Applied Mechanics*, Vol. 17, 1950.

3. Herbert, M. V. A Theoretical Analysis of Reaction Rate Controlled Systems—Part I. *AGARD Combustion Researches and Reviews*, Butterworth, London, 1957. Part II—*Eighth International Symposium on Combustion, 1960*. To be published by Williams and Wilkins, Baltimore.

The Behaviour of a Clamped Circular Plate in Compression

A. N. SHERBOURNE

(University Engineering Laboratory, Cambridge)

SUMMARY: A theoretical solution is presented for the problem of the clamped circular plate loaded in uniform compression. The solution employs a numerical method programmed for a digital computer. Instead of solving the classical von Kármán large deflection equations, a step-by-step integration of the elastic differential equations of equilibrium is carried out until suitable boundary conditions are attained. The method is an extension of one developed earlier to explain the behaviour of the simply-supported plate.

1. Introduction

The ultimate load for thin plates under uniform compression may be estimated from the intersection of an elastic-plastic loading path and a rigid-plastic mechanism line, when the resulting load will represent an upper bound on the collapse of the plate. The treatment of the circular plate appears to fall naturally into two distinct problems, involving the simply-supported and the clamped plate; each problem may be regarded separately by defining the complete loading history for plates with these particular boundary conditions. For the plate with the elastically restrained edge, an estimate of the collapse load and loading history may conveniently be obtained by interpolating between the two solutions mentioned.

The classical problem of the clamped circular plate in compression has been discussed by Bodner[1]. His solution applied power series and perturbation methods developed earlier by Friedrichs and Stoker[2] to explain the behaviour of the simply-supported circular plate loaded beyond the critical thrust. Timoshenko[3] has used numerical methods to determine the elastic behaviour, at large deflection, of a circular plate bent by couples uniformly distributed along the supported edge.

A previous paper[4] developed a numerical procedure for the post-buckling behaviour of a simply-supported circular plate. The method obviated the solution of the classical von Kármán large deflection equations, substituting, instead, a step-by-step integration of the equations of equilibrium until specific boundary conditions were attained. Such a method had the added advantage of accommodating plastic behaviour by a suitable modification of the equations of moment, thrust and equilibrium for the bent plate.

Received October 1960.

The current investigation applies this numerical method to the clamped circular plate loaded in uniform compression beyond the critical thrust, the analysis being confined to elastic behaviour throughout the plate. The procedure converts the conventional two-point boundary-value problem, in which statical and geometrical conditions are fulfilled at the centre of the plate and along the supported edge, into an initial-value problem by selecting appropriate numerical values for the moment and thrust at the centre of the plate. These values completely define the geometry of the plate as expressed in terms of the radial and transverse displacements and are so chosen as to preserve elastic behaviour. A step-by-step integration of the differential equations of equilibrium is carried out and statical and geometrical conditions are evaluated over each interval. This process is continued until a critical radius is reached when the statics and geometry match prescribed boundary conditions on the problem. For the clamped plate this implies a condition of zero slope, and the boundary tractions are evaluated in this position. By varying the initial combinations of moment and thrust, a set of boundary tractions can be obtained corresponding to plates of various size. For a plate of specific radius, with particular boundary conditions, the elastic, post-buckling behaviour at large deflection may be obtained by interpolating between the contours of moment and thrust.

Notation

u, w radial and transverse displacements

r radius

R plate radius

μ Poisson's ratio

h plate thickness

D flexural rigidity of plate, $= Eh^3/\{12(1-\mu^2)\}$

E modulus of elasticity

γ, β non-dimensional moment and thrust

γ_r, β_r non-dimensional moment and thrust in radial direction

γ_t, β_t non-dimensional moment and thrust in tangential direction

m_p fully plastic moment per unit width of plate, $= h^2 f_y/4$

f_y yield stress in tension or compression

σ mean stress in plate

$k^2 = E/\{3f_y(1-\mu^2)\}$

$\alpha = dw/dr$

$q^2 = hp/D$

p applied edge load per unit width

p_{cr} elastic critical load per unit width

$\bar{\gamma}$, $\bar{\beta} = \gamma/k^2$ and β/k^2 respectively

$\bar{w}, \bar{u}, \bar{r}, \bar{R} = w/h, u/h, r/h$ and R/h, respectively

W, U functions of $\bar{r}^2$

P total edge load

P_y yield load.

The suffixes r, t, 0 denote the radial and tangential directions and the centre of the plate respectively.

2. General Analysis

The elastic critical load and subsequent post-buckling behaviour of a circular plate may be obtained from the equilibrium of the plate at large deflection,

$$\frac{d^2u}{dr^2} = -\frac{1}{r}\frac{du}{dr} + \frac{u}{r^2} - \frac{(1-\mu)}{2r}\left(\frac{dw}{dr}\right)^2 - \left(\frac{dw}{dr}\right)\left(\frac{d^2w}{dr^2}\right) \quad . \quad . \quad (1)$$

$$\frac{d^3w}{dr^3} = -\frac{1}{r}\frac{d^2w}{dr^2} + \frac{1}{r^2}\frac{dw}{dr} + \frac{12}{h^2}\frac{dw}{dr}\left[\frac{du}{dr} + \frac{1}{2}\left(\frac{dw}{dr}\right)^2 + \mu\frac{u}{r}\right], \quad . \quad (2)$$

where u and w are the radial and transverse displacements respectively at radius r, μ is Poisson's ratio and h is the plate thickness.

The critical load is obtained from equation (2) by considering the associated plane strain problem in the small deflection theory

$$r^2\frac{d^2\alpha}{dr^2} + r\frac{d\alpha}{dr} + (q^2r^2 - 1)\alpha = 0, \quad . \quad . \quad . \quad . \quad (3)$$

such that $\alpha = dw/dr$, $q^2 = hp/D$, where D is the flexural rigidity of the plate, $Eh^3/\{12(1-\mu^2)\}$, and p is the applied edge load.

For the clamped plate, of radius R, a solution of equation (3) is given by the characteristic value

$$p_{cr} = \frac{14{\cdot}68D}{hR^2} \quad . \quad . \quad . \quad . \quad . \quad . \quad (4)$$

The moments and thrusts obtaining in the plate can be expressed, in terms of the parameters γ and β, as

$$\gamma = m/m_p$$
$$\beta = \sigma/f_y,$$

where m is a general moment in the plate, m_p the full plastic moment per unit width of plate ($=\frac{1}{4}h^2f_y$), σ the mean stress in the plate and f_y the yield stress in simple tension or compression. At large deflection, the moments and thrusts are determined from the system of strains and stresses obtaining in the bent plate[4] and may be written as follows.

$$\left.\begin{aligned}
\gamma_r &= -k^2 h\left[\frac{d^2w}{dr^2} + \frac{\mu}{r}\frac{dw}{dr}\right] \\
\beta_r &= 3k^2\left[\frac{du}{dr} + \frac{1}{2}\left(\frac{dw}{dr}\right)^2 + \mu\frac{u}{r}\right] \\
\gamma_t &= -k^2 h\left[\frac{1}{r}\frac{dw}{dr} + \mu\frac{d^2w}{dr^2}\right] \\
\beta_t &= 3k^2\left[\frac{u}{r} + \mu\frac{du}{dr} + \frac{\mu}{2}\left(\frac{dw}{dr}\right)^2\right],
\end{aligned}\right\} \quad . \quad . \quad . \quad (5)$$

where $k^2 = \dfrac{E}{3f_y(1-\mu^2)}$

and the suffixes r and t denote the radial and tangential directions respectively.

The initial conditions are obtained from the symmetry of statics and geometry at $r=0$. Substitution for identical curvatures, strains and slopes in the radial and tangential directions in equations (1), (2) and (5), gives

$$\left.\begin{aligned}
u_0 = w_0 &= \left[\left(\frac{dw}{dr}\right)\right]_0 = 0 \\
\left[\frac{1}{r}\frac{dw}{dr}\right]_0 &= \left[\left(\frac{d^2w}{dr^2}\right)\right]_0 = -\frac{\gamma_0}{k^2 h(1+\mu)} \\
\left[\frac{du}{dr}\right]_0 &= \left[\frac{u}{r}\right]_0 = \frac{\beta_0}{3k^2(1+\mu)} \\
\left[r\frac{d^2u}{dr^2}\right]_0 &= \left[r\frac{d^3w}{dr^3}\right]_0 = 0
\end{aligned}\right\} \quad . \quad . \quad . \quad (6)$$

and $\gamma_r = \gamma_t = \gamma_0$, $\beta_r = \beta_t = \beta_0$.

A limiting condition of elasticity throughout the plate is derived by considering the interaction between moment and thrust within a maximum stress criterion

$$\gamma \leqslant \frac{2}{3}\left(1 - |\beta|\right). \quad . \quad . \quad . \quad . \quad . \quad (7)$$

such that $|\beta|$ caters for membrane tension or compression.

The previous equations may be non-dimensionalised through the relationships

$$\bar{\gamma} = \frac{\gamma}{k^2}, \quad \bar{\beta} = \frac{\beta}{k^2}, \quad \bar{w} = \frac{w}{h}, \quad \bar{u} = \frac{u}{h}, \quad \bar{r} = \frac{r}{h}$$

when the entire problem can be defined as follows.

(*a*) The equations of moment and thrust,

$$\left.\begin{aligned} \bar{\gamma}_r &= -\left[\frac{d^2\bar{w}}{d\bar{r}^2} + \frac{\mu}{\bar{r}}\frac{d\bar{w}}{d\bar{r}}\right] \\ \bar{\beta}_r &= 3\left[\frac{d\bar{u}}{d\bar{r}} + \frac{1}{2}\left(\frac{d\bar{w}}{d\bar{r}}\right)^2 + \mu\frac{\bar{u}}{\bar{r}}\right] \\ \bar{\gamma}_t &= -\left[\frac{1}{\bar{r}}\frac{d\bar{w}}{d\bar{r}} + \mu\frac{d^2\bar{w}}{d\bar{r}^2}\right] \\ \bar{\beta}_t &= 3\left[\frac{\bar{u}}{\bar{r}} + \mu\frac{d\bar{u}}{d\bar{r}} + \frac{\mu}{2}\left(\frac{d\bar{w}}{d\bar{r}}\right)^2\right] \end{aligned}\right\} \quad . \quad . \quad . \quad . \quad . \quad (8)$$

(*b*) The differential equations of equilibrium,

$$\left.\begin{aligned} \bar{r}\frac{d^2\bar{u}}{d\bar{r}^2} &= -\frac{d\bar{u}}{d\bar{r}} + \frac{\bar{u}}{\bar{r}} - \frac{(1-\mu)}{2}\left(\frac{d\bar{w}}{d\bar{r}}\right)^2 - \bar{r}\left(\frac{d\bar{w}}{d\bar{r}}\right)\left(\frac{d^2\bar{w}}{d\bar{r}^2}\right) \\ \bar{r}\frac{d^3\bar{w}}{d\bar{r}^3} &= -\frac{d^2\bar{w}}{d\bar{r}^2} + \frac{1}{\bar{r}}\frac{d\bar{w}}{d\bar{r}} + 12\bar{r}\left(\frac{d\bar{w}}{d\bar{r}}\right)\left[\frac{d\bar{u}}{d\bar{r}} + \frac{1}{2}\left(\frac{d\bar{w}}{d\bar{r}}\right)^2 + \mu\frac{\bar{w}}{\bar{r}}\right] \end{aligned}\right\} \quad . \quad (9)$$

(*c*) The initial conditions,

$$\left.\begin{aligned} \bar{u}_0 = \bar{w}_0 &= \left[\frac{d\bar{w}}{d\bar{r}}\right]_0 = 0 \\ \left[\frac{1}{\bar{r}}\frac{d\bar{w}}{d\bar{r}}\right]_0 &= \left[\frac{d^2\bar{w}}{d\bar{r}^2}\right]_0 = -\frac{\bar{\gamma}_0}{(1+\mu)} \\ \left[\frac{d\bar{u}}{d\bar{r}}\right]_0 &= \left[\frac{\bar{u}}{\bar{r}}\right]_0 = \frac{\bar{\beta}_0}{3(1+\mu)} \\ \left[\bar{r}\frac{d^2\bar{u}}{d\bar{r}^2}\right]_0 &= \left[\bar{r}\frac{d^3\bar{w}}{d\bar{r}^3}\right]_0 = 0 \end{aligned}\right\} \quad . \quad . \quad . \quad . \quad (10)$$

(*d*) The conditions for elasticity.

Elastic behaviour at the centre of the plate can be expressed by the inequality

$$\bar{\gamma}_0 \leqslant \frac{2}{3}\left(\frac{1}{k^2} - |\bar{\beta}_0|\right), \quad . \quad . \quad . \quad . \quad (11)$$

whereas at radius r, the inequality expressing elastic behaviour in orthogonal directions is given by

$$\left.\begin{aligned} \bar{\gamma}_r &\leqslant \frac{2}{3}\left(\frac{1}{k^2} - |\bar{\beta}_r|\right) \\ \bar{\gamma}_t &\leqslant \frac{2}{3}\left(\frac{1}{k^2} - |\bar{\beta}_t|\right) \end{aligned}\right\} \quad . \quad . \quad . \quad . \quad (12)$$

3. The Numerical Method for Integrating the Differential Equations of Equilibrium

Before suggesting a programme for the numerical integration of the differential equations of equilibrium, it is necessary to obtain finite initial values for $d^2\bar{u}/d\bar{r}^2$ and $d^3\bar{w}/d\bar{r}^3$. The singularities in these functions, which prevail at the origin, are of the form $0/0$ and may be removed by introducing the transformations

$$\left.\begin{aligned} \bar{w}(\bar{r}) &= W(\bar{r}^2) \\ \bar{u}(\bar{r}) &= \bar{r}U(\bar{r}^2) \\ \bar{r}^2 &= x \end{aligned}\right\} \quad . \quad . \quad . \quad . \quad . \quad (13)$$

when the entire problem may be redefined in terms of the new variables, as follows.

(*a*) The equations of moment and thrust,

$$\left.\begin{aligned} \gamma_r &= -[2(1+\mu)W' + 4xW''] \\ \bar{\beta}_r &= 3[(1+\mu)U + 2x\{U' + (W')^2\}] \\ \bar{\gamma}_t &= -[2(1+\mu)W' + 4\mu xW''] \\ \bar{\beta}_t &= 3[(1+\mu)U + 2\mu x\{U' + (W')^2\}] \end{aligned}\right\} \quad . \quad . \quad . \quad (14)$$

where primes ($'$) denote differentiation with respect to x.

(*b*) The equations of equilibrium,

$$\left.\begin{aligned} U'' &= -\frac{2}{x}U' + \frac{\mu-3}{2x}(W')^2 - 2W'W''' \\ W''' &= -\frac{2}{x}W'' + \frac{3(1+\mu)}{x}UW' + 6W'\{U' + (W')^2\} \end{aligned}\right\} \quad . \quad . \quad (15)$$

(*c*) The initial conditions,

$$\left.\begin{aligned} W_0 &= 0 & U_0 &= \frac{\bar{\beta}_0}{3(1+\mu)} \\ W_0' &= -\frac{\bar{\gamma}_0}{2(1+\mu)} & U_0' &= \frac{(\mu-3)\bar{\gamma}_0^2}{16(1+\mu)^2} \\ W_0'' &= -\frac{\bar{\gamma}_0\bar{\beta}_0}{4(1+\mu)} & U_0'' &= \frac{(\mu-5)\bar{\beta}_0\bar{\gamma}_0^2}{24(1+\mu)^2} \\ W_0''' &= \frac{\bar{\gamma}_0}{96(1+\mu)}[3(1-\mu)\bar{\gamma}_0^2 - 8(1+\mu)\bar{\beta}_0^2] \end{aligned}\right\} \quad . \quad . \quad . \quad . \quad (16)$$

(*d*) The yield conditions,

$$\bar{\gamma}_0 \leqslant \frac{2}{3}\left(\frac{1}{k^2} - |\bar{\beta}_0|\right) \quad . \quad . \quad . \quad . \quad . \quad . \quad . \quad . \quad . \quad . \quad (17)$$

$$\left.\begin{aligned} \bar{\gamma}_r &\leqslant \frac{2}{3}\left(\frac{1}{k^2} - |\bar{\beta}_r|\right) \\ \bar{\gamma}_t &\leqslant \frac{2}{3}\left(\frac{1}{k^2} - |\bar{\beta}_t|\right) \end{aligned}\right\} \quad . \quad . \quad . \quad . \quad . \quad . \quad . \quad . \quad . \quad . \quad (18)$$

The load-deflection relationship for the clamped circular plate in compression can now be obtained using a numerical procedure, the equations (14) to (18) being of a form suitable for programming on a digital computer. The various stages of such a programme may be outlined as follows.

Stage 1. Select values of $\bar{\gamma}_0$, $\bar{p}_0$ in accordance with equation (17).

Stage 2. Evaluate the initial conditions as given by equation (16).

Stage 3. Advance the functions W, W', W'', W''', U, U', U'', a single step δ, using a numerical integration procedure, and evaluate the moments and thrusts as given by equation (14). Check the yield conditions, equation (18), to ensure that the plate is elastic at radius δ.

Stage 4. Repeat Stage 3 until the slope is zero. This implies that $W'=0$.

Stage 5. Evaluate and print out the required results. For the clamped plate, obtain

the critical radius $\bar{R}$,	the boundary moment $\bar{\gamma}_R$,
the boundary thrust $\bar{\beta}_r=\bar{p}$,	the total deflection $\bar{w}_0$.

Stage 6. Repeat Stages 1 to 5 using a different set of $\bar{\gamma}_0$, $\bar{\beta}_0$.

4. The EDSAC Sub-Routine

The equations (14) to (18) were programmed for EDSAC II, the Cambridge University High Speed Digital Computer, the numerical integration being carried out using a modified fourth-order Runge-Kutta process which is incorporated in the machine as a Library Sub-Routine. As contained in EDSAC, the sub-routine will handle a set of simultaneous first-order differential equations in which each derivative is expressed explicitly in terms of the dependent variables

$$\begin{aligned} y_1' &= f_1(y_1, y_2, \ldots . y_n) \\ y_2' &= f_2(y_1, y_2, \ldots . y_n) \\ &\ldots \ldots \ldots \\ y_n' &= f_n(y_1, y_2, \ldots . y_n) \end{aligned}$$

Any equation or set of equations must be expressed in this form before the integration process can be applied.

Since the differential equations of equilibrium are of the form

$$U'' = F(x, U', W', W'')$$
$$W''' = G(x, U, U', W', W''),$$

they can be reduced to a set of first-order equations by introducing as many dependent variables as may be required,

$$x = s_1$$
$$U' = s_2$$
$$W' = s_3$$
$$W'' = \frac{ds_3}{dx} = s_4.$$

The resulting set of simultaneous equations is now of the form required in the sub-routine

$$\left.\begin{aligned} \frac{ds_2}{dx} &= F(s_1, s_2, s_3, s_4) \\ \frac{ds_4}{dx} &= G(s_1, U, s_2, s_3, s_4) \\ \frac{ds_1}{dx} &= 1 \\ \frac{ds_3}{dx} &= s_4 \\ \frac{dU}{dx} &= s_2 \end{aligned}\right\} \quad . \quad . \quad . \quad . \quad (19)$$

The sub-routine operates on the equations (19) by evaluating the dependent variables s_1, U, s_2, s_3 and s_4 at the half-interval $\delta/2$ using a fourth-order Runge-Kutta process and uses these functional values at the half-interval to advance the functions over a full interval. In this respect the procedure differs from orthodox numerical integration techniques where functional values are obtained directly over the full interval δ.

The Runge-Kutta procedure, used in the sub-routine of EDSAC for the numerical integration of a set of first-order simultaneous differential equations, has powerful advantages when compared with other methods of numerical integration inasmuch as it can easily be modified to include changes in the step interval, it is self-starting and does not require back information to continue the integration procedure. These features become important in high-speed digital computers since they lead to a minimum of special instructions, with consequent saving in machine time.

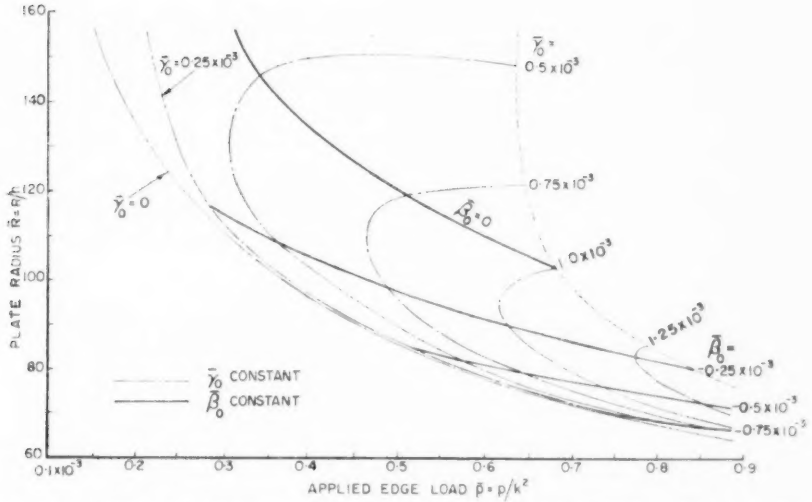

FIGURE 1. Plate size against applied edge load for a clamped circular plate (for elastic behaviour in the plate).

Notes: $\bar{\beta}_0\times k^2\times hf_y$ = mean stress at the centre of the plate (tons/in.)

$\bar{\gamma}_0\times k^2\times\dfrac{h^2f_y}{4}$ = moment at the centre of the plate (ton in./in.)

$\bar{p}\times k^2\times hf_y$ = edge load (tons/in.)

$$k^2=\frac{E}{3f_y(1-\mu^2)}=322 \text{ for } E=13{,}400 \text{ tons/in.}^2,\quad f_y=15{\cdot}25 \text{ tons/in.}^2,\quad \mu=0{\cdot}3.$$

5. Results

The programme was evaluated for the range of $\bar{\gamma}_0$ and $\bar{\beta}_0$ given in Table I, positive $\bar{\beta}_0$ being associated with a tension field and negative $\bar{\beta}_0$ with a compression field at the centre of the plate. The relationships between plate size, edge thrust, edge moment and central deflection are given in Figs. 1, 2, and 3 through contours of the moment and thrust parameters acting at the centre of the plate. For a given plate size, the load-deflection relationship may be determined by interpolating between contours. In deriving the results, the values chosen for the mechanical properties of mild steel were

$E=13{,}400$ tons/in.^{2},
$\mu=0{\cdot}3$,
$f_y=15{\cdot}25$ tons/in.^{2},
$k^2=322$, and hence $1/k^2=3{\cdot}1\times10^{-3}$.

TABLE I

THE CLAMPED PLATE

$10^3\bar{\gamma}_0$	$10^3\bar{\beta}_0$	$\bar{R}=\frac{R}{h}$	$\bar{w}_0=\frac{w_0}{h}$	$10^3\bar{p}\left(=10^3\frac{p}{k^2}\right)$	$10^3\bar{\gamma}_R\left(=10^3\frac{\gamma_R}{k^2}\right)$	$10^3\bar{\gamma}_0$	$10^3\bar{\beta}_0$	$\bar{R}=\frac{R}{h}$	$\bar{w}_0=\frac{w_0}{h}$	$10^3\bar{p}\left(=10^3\frac{p}{k^2}\right)$	$10^3\bar{\gamma}_R\left(=10^3\frac{\gamma_R}{k^2}\right)$
0·25	0	206·45	−2·3339	−0·17038	−0·34050	0·8		53·366	−0·33844	−1·3187	−0·50693
0·5		145·98	−2·3339	−0·34075	−0·68100	1·0		52·932	−0·41851	−1·3563	−0·64009
0·75		119·19	−2·3339	−0·51113	−1·0215	1·2		52·428	−0·49584	−1·4015	−0·77809
1·0		103·22	−2·3339	−0·68151	−1·3620	1·24		52·319	−0·51095	−1·4114	−0·80626
0·25	−0·25	116·93	−0·51471	−0·28278	−0·16267	0·2	−1·5	49·433	−0·07187	−1·5036	−0·12405
0·5		107·75	−0·91965	−0·36901	−0·36024	0·4		49·331	−0·14336	−1·5145	−0·24881
0·75		98·238	−1·2052	−0·49784	−0·59704	0·6		49·165	−0·21410	−1·5325	−0·37498
1·0		90·004	−1·4050	−0·62490	−0·86315	0·8		48·937	−0·28373	−1·5575	−0·50322
1·25		83·183	−1·5486	−0·77243	−1·1490	1·0		48·654	−0·35196	−1·5893	−0·63409
0·25	−0·5	84·873	−0·26644	−0·51688	−0·15697	1·07		48·544	−0·37545	−1·6020	−0·68060
0·5		82·681	−0·51471	−0·56555	−0·32533	0·15	−1·75	45·785	−0·04623	−1·7518	−0·09298
0·75		79·620	−0·73349	−0·64118	−0·51238	0·3		45·746	−0·09235	−1·7570	−0·18619
1·0		76·194	−0·91965	−0·73802	−0·72048	0·45		45·681	−0·13828	−1·7657	−0·27984
1·25		72·748	−1·0754	−0·85088	−0·94856	0·6		45·590	−0·18390	−1·7779	−0·37415
1·5		69·465	−1·2052	−0·97569	−1·1941	0·75		45·479	−0·22912	−1·7935	−0·46930
0·25	−0·75	69·660	−0·17884	−0·76131	−0·15584	0·90		45·342	−0·27386	−1·8124	−0·56553
0·5		68·809	−0·35196	−0·79465	−0·31704	0·15	−2·0	42·829	−0·04045	−2·0015	−0·09298
0·75		67·509	−0·51471	−0·84833	−0·48800	0·3		42·801	−0·08084	−2·0061	−0·18612
1·0		65·893	−0·66418	−0·91999	−0·67159	0·45		42·754	−0·12108	−2·0138	−0·27961
1·25		64·093	−0·79913	−1·0071	−0·86912	0·6		42·688	−0·16113	−2·0245	−0·37361
1·5		62·212	−0·91965	−1·1070	−1·0807	0·73		42·622	−0·19562	−2·0361	−0·45558
1·57		61·681	−0·95092	−1·1370	−1·1424	0·1	−2·25	40·386	−0·02398	−2·2506	−0·06197
0·25	−1·0	60·438	−0·13446	−1·0085	−0·15543	0·2		40·377	−0·04794	−2·2524	−0·12398
0·5		60·014	−0·26644	−1·0338	−0·31395	0·3		40·361	−0·07187	−2·2555	−0·18607
0·75		59·340	−0·39376	−1·0750	−0·47831	0·4		40·339	−0·09576	−2·2597	−0·24828
1·0		58·464	−0·51471	−1·1311	−0·65066	0·5		40·311	−0·11960	−2·2651	−0·31066
1·25		57·435	−0·62815	−1·2007	−0·83254	0·57		40·288	−0·13624	−2·2696	−0·35443
0·2	−1·25	54·135	−0·08621	−1·2544	−0·12410	0·05	−2·5	38·316	−0·01079	−2·5001	−0·03098
0·4		53·975	−0·17177	−1·2674	−0·24923	0·1		38·315	−0·02158	−2·5005	−0·06197
0·6		53·716	−0·25603	−1·2889	−0·37636	0·15		38·312	−0·03237	−2·5012	−0·09296
						0·2		38·308	−0·04315	−2·5022	−0·12397

TABLE I—*continued*

$10^3\bar{\gamma}_0$	$10^3\bar{\beta}_0$	$\bar{R}=\frac{R}{h}$	$\bar{w}_0=\frac{w_0}{h}$	$10^3\bar{p}\left(=10^3\frac{p}{k^2}\right)$	$10^3\bar{\gamma}_B\left(=10^3\frac{\gamma_B}{k^2}\right)$	$10^3\bar{\gamma}_0$	$10^3\beta_0$	$R=\frac{R}{h}$	$\bar{w}_0=\frac{w_0}{h}$	$10^3\bar{p}\left(=10^3\frac{p}{k^2}\right)$	$10^3\bar{\gamma}_B\left(=10^3\frac{\gamma_B}{k^2}\right)$
0·25		38·302	−0·05393	−2·5034	−0·15499		−1·0	60·014	−0·26644	−1·0338	−0·31395
0·3		38·296	−0·06470	−2·5049	−0·18604		−0·75	68·809	−0·35196	−0·79465	−0·31704
0·35		38·288	−0·07546	−2·5067	−0·21710		−0·5	82·681	−0·51471	−0·56555	−0·32533
0·4		38·279	−0·08621	−2·5087	−0·24820		−0·25	107·75	−0·91965	−0·36901	−0·36024
0·05	−2·75	36·529	−0·00981	−2·7501	−0·03099		0	145·98	−2·3339	−0·34075	−0·68100
0·1		36·527	−0·01962	−2·7505	−0·06197	0·75	−1·975	42·872	−0·20341	−2·0136	−0·46834
0·15		36·525	−0·02942	−2·7511	−0·09297		−1·75	45·479	−0·22912	−1·7935	−0·46930
0·2		36·521	−0·03923	−2·7520	−0·12397		−1·5	49·000	−0·26644	−1·5506	−0·47093
0·23		36·519	−0·04511	−2·7526	−0·14258		−1·25	53·461	−0·31804	−1·3105	−0·47357
0·02	−3·0	34·978	−0·00360	−3·0000	−0·01239		−1·0	59·340	−0·39376	−1·0750	−0·47831
0·04		34·978	−0·00719	−3·0001	−0·02479		−0·75	67·509	−0·51471	−0·84833	−0·48800
0·06		34·978	−0·01079	−3·0002	−0·03718		−0·5	79·620	−0·73349	−0·64118	−0·51238
0·07		34·978	−0·01259	−3·0002	−0·04338		−0·25	98·238	−1·2052	−0·48784	−0·59704
0·25	−2·725	36·687	−0·04948	−2·7281	−0·15498		0	119·19	−2·3339	−0·51113	−1·0215
	−2·5	38·302	−0·05393	−2·5034	−0·15499	1·0	−1·6	47·201	−0·33081	−1·6839	−0·63240
	−2·25	40·370	−0·05991	−2·2538	−0·15501		−1·5	48·654	−0·35196	−1·5893	−0·63409
	−2·0	42·812	−0·06739	−2·0043	−0·15504		−1·25	52·932	−0·41851	−1·3563	−0·64009
	−1·75	45·761	−0·07700	−1·7549	−0·15508		−1·0	58·464	−0·51471	−1·1311	−0·65066
	−1·5	49·414	−0·08980	−1·5057	−0·15514		−0·75	65·893	−0·66418	−0·91999	−0·67159
	−1·25	54·105	−0·10769	−1·2568	−0·15525		−0·5	76·194	−0·91965	−0·73802	−0·72048
	−1·0	60·438	−0·13446	−1·0085	−0·15543		−0·25	90·004	−1·4050	−0·62490	−0·86315
	−0·75	69·660	−0·17884	−0·76131	−0·15584		0	103·22	−2·3339	−0·68151	−1·3620
	−0·5	84·873	−0·26644	−0·51688	−0·15697	1·25	−1·225	52·752	−0·52426	−1·3920	−0·81479
	−0·25	116·93	−0·51471	−0·28278	−0·16267		−1·0	57·435	−0·62815	−1·2007	−0·83254
	0	206·45	−2·3339	−0·17038	−0·34050		−0·75	64·093	−0·79913	−1·0071	−0·86912
0·5	−2·35	39·451	−0·11453	−2·3645	−0·31059		−0·5	72·748	−1·0754	−0·85088	−0·94856
	−2·25	40·311	−0·11960	−2·2651	−0·31066		−0·25	83·183	−1·5486	−0·77243	−1·1490
	−2·0	42·734	−0·13446	−2·0170	−0·31088	1·5	−0·85	59·689	−0·83605	−1·1733	−1·0539
	−1·75	45·653	−0·15352	−1·7694	−0·31119		−0·8	60·923	−0·87610	−1·1394	−1·0664
	−1·5	49·259	−0·17884	−1·5226	−0·31168		−0·6	66·409	−1·0754	−1·0211	−1·1383
	−1·25	53·859	−0·21410	−1·2771	−0·31248						

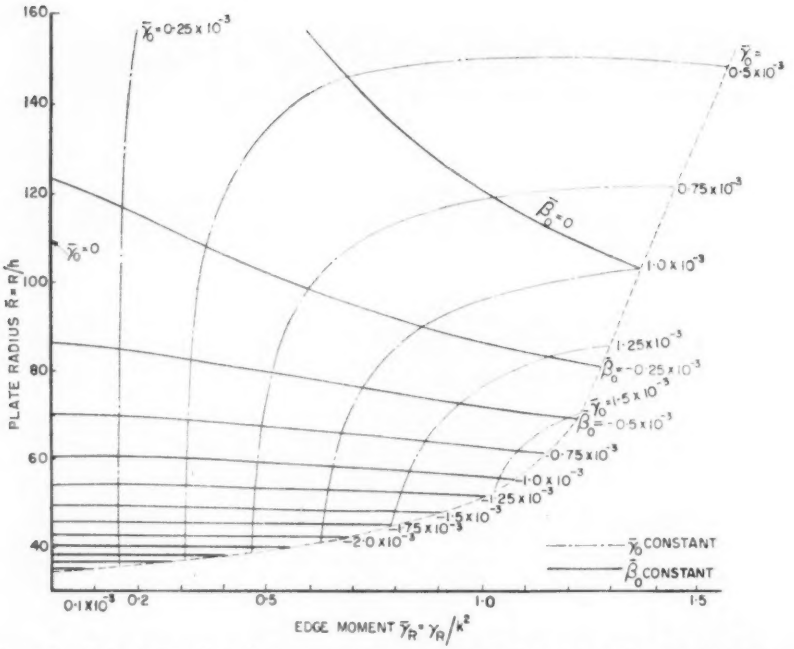

FIGURE 2. Plate size against edge moment for a clamped circular plate (for elastic behaviour in the plate).

6. Conclusions

A general load-deflection relationship for the clamped circular plate in compression may be deduced from the contours of Figs. 1 and 3. It can be shown that the relationship is of the form (*see* the Appendix)

$$\frac{P}{P_y} = -k_1\left(\frac{E}{f_y}\right)\left(\frac{h}{R}\right)^2 - k_2\left(\frac{E}{f_y}\right)\left(\frac{h}{R}\right)^2\left(\frac{w_0}{h}\right)^2, \qquad (20)$$

where the applied edge load and central deflection are expressed non-dimensionally. It should be noted that the first term of the expression on the right hand side represents the critical load as given by equation (4) and the second term represents the elastic, post-buckling behaviour. Equation (20) may be fitted to the results obtained from the computer programme by plotting the load against the square of the deflection for plates of various sizes when the locus of all points, for a given plate size, will constitute a straight line intersecting the load axis in the critical load and having a slope which defines the coefficient $-k_2(E/f_y)(h/R)^2$. Using this approach, the coefficients of equation (20) may be approximated to

$$k_1 = 1{\cdot}348 \quad \text{and} \quad k_2 = 0{\cdot}22.$$

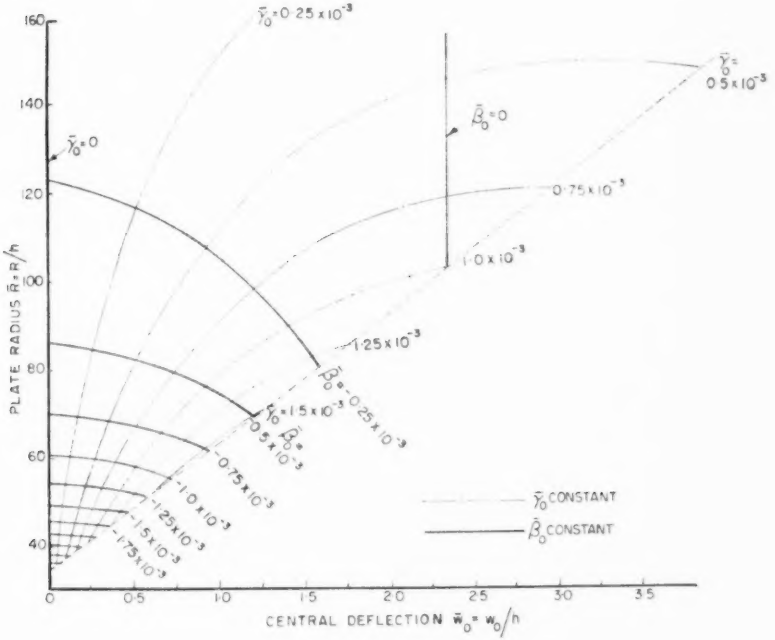

FIGURE 3. Plate size against central deflection for a clamped circular plate (for elastic behaviour in the plate).

ACKNOWLEDGMENTS

The author is grateful to Professor J. F. Baker for enabling him to carry out this research in the Engineering Department of the University of Cambridge. The results obtained on EDSAC II are published with the permission of the Director of the Cambridge University Mathematical Laboratory and the author is indebted to Miss G. M. Christ for programming the problem.

REFERENCES

1. BODNER, S. R. The Post-Buckling Behaviour of a Clamped Circular Plate. *Quarterly of Applied Mathematics*, Vol. 12, 1954.

2. FRIEDRICHS, K. O. and STOKER, J. J. Buckling of the Circular Plate Beyond the Critical Thrust. *Journal of Applied Mechanics*, Vol. 9, 1942.

3. TIMOSHENKO, S. *Theory of Plates and Shells*. McGraw-Hill, 1940.

4. SHERBOURNE, A. N. The Elastic, Post-Buckling Behaviour of a Simply Supported Circular Plate. (To be published.)

Appendix

The form of the load-deflection curve near the elastic critical load may be determined from the total energy of the bent plate,

$$V=V_B+V_M+V_E, \quad . \quad . \quad . \quad . \quad . \quad (21)$$

where the total energy V is made up of a bending component V_B, a membrane component V_M and the work done by the external load V_E. For large deflections the total energy can be written in terms of the total applied load P and the radial and transverse displacements u and w respectively.

$$V=\phi_1(w^2)+\phi_2(u^2, uw^2, w^4)+\phi_3(Pu), \quad . \quad . \quad . \quad (22)$$

such that $V_B=\phi_1(w^2)$,

$V_M=\phi_2(u^2, uw^2, w^4)$,

$V_E=\phi_3(Pu)$.

From the theorem of minimum potential energy

$$\frac{\partial V}{\partial w}=0$$

and u may be obtained as a function of w,

$$u=\phi_4(w^2). \quad . \quad . \quad . \quad . \quad . \quad . \quad (23)$$

The total energy is now a function of w only,

$$V=\psi_1(w^2)+\psi_2(w^4)+\psi_3(Pw^2), \quad . \quad . \quad . \quad . \quad (24)$$

The load-displacement relationship may be obtained from the condition

$$\frac{\partial V}{\partial w}=0=\psi_4(w)+\psi_5(w^3)+\psi_6(Pw), \quad . \quad . \quad . \quad . \quad (25)$$

when $P=P_{cr}+Kw^2$.

The Design of Wing Plan Forms for Transonic Speeds

R. C. LOCK, M.A., Ph.D.

(Aerodynamics Division, National Physical Laboratory)

SUMMARY: A method is suggested for designing the shape of the plan form of an unwarped swept-back wing so as to control the magnitude of the singularity that occurs in the chordwise loading distribution at the leading edge. At a Mach number of unity it is possible to do this simply and directly by an approximate application of linearised lifting-surface theory. Details are given of three families of wing plan forms, of varying sweep and aspect ratio, in all of which the strength of the leading-edge singularity is held constant near the wing tips, behind the Mach line from the root trailing edge. The local chordwise load distributions have been calculated in detail for several of these wings and it is found that in all cases the loading curves become effectively independent of spanwise position over that part of the span for which the singularity is constant.

1. Introduction

In the design of swept-winged aircraft to fly at transonic speeds, one of the important features which must be chosen is the wing plan form. The aspect ratio and basic angle of sweep will probably be fixed within narrow limits as a compromise between aerodynamic and structural considerations, but the detailed shaping of the plan form can still have a considerable effect on the aerodynamic behaviour of the wings. This is true to some extent for symmetrical wings at zero incidence, but the lifting aspects of the problem are much more important and are all that will be considered here.

The treatment must be restricted at the present time to the use of linearised theory for lifting surfaces, so that the effects on the loading of the wing thickness distribution, as well as of viscosity and shock waves, have to be neglected. Even so, at supersonic speeds there does not seem to be any satisfactory method applicable to wings of arbitrary plan form, though a great many particular solutions are available for wings with straight leading and trailing edges[1]; and the methods which have been developed for subsonic speeds[1] all break down as the Mach number approaches unity. Fortunately, however, at $M = 1$, lifting-surface theory is considerably simplified[2] and becomes identical to "sender wing" theory[3]. This form of the theory will be used in the present paper. It is felt that this should not unduly restrict the practical applications, since the results for highly swept wings should be

Received January 1961.

directly relevant over a range of Mach numbers around unity, and even outside this range the conclusions should be qualitatively correct.

There is now some experimental evidence that this theory does give good results for overall wing lift, provided that the leading-edge sweepback exceeds about 45°. Further, a comparison with theory of the detailed loading obtained at low incidences in a recent series of tests at the N.P.L.[4] on an uncambered wing of aspect ratio 2·8, taper ratio 1/3 and half-chord sweep 45° has shown reasonable agreement, particularly over the inboard half of the wing. This comparison is shown in Fig. 1. It can be seen that the agreement is poorer near the tip; this is partly due to the complicated shock system which appears in this region at quite small incidences (*see* Fig. 1) and to the failure of the theory to predict correctly the position of these shocks. However, this shock system, and particularly the "forward shock", which does not occur at all in the theory, is to some extent associated with the very high suction peaks and local Mach numbers which occur near the tips of conventional tapered swept wings at incidence in the transonic speed range. These high suction peaks are a fundamental defect of wing plan forms with straight edges, particularly when highly tapered, and it was felt that if they could be alleviated by suitable plan form design—and this is one of the principal objects of the present paper—then not only would such plan forms be of some practical value, but might also show better agreement between experiment and theory.

The present method of design is similar in some ways to that used by Brebner[5] in designing "constant C_L" plan forms for low speeds, but concentrates more directly on the real source of the trouble which, in linearised lifting-surface theory, appears as the singularity* in the load distribution at the leading edge. The trailing edge is first chosen to be straight and uniformly swept (*see* Fig. 2); this is not an essential feature but it represents the most feasible shape in practice if conventional controls are to be used. At the centre section of any swept wing (or at the wing-body junction of a complete aircraft) the load distribution has no singularity, so that over the inboard part of the wing the strength of the leading-edge singularity inevitably increases steadily in the spanwise direction; the rate of increase depends on the shape of the inner part of the leading edge, which may be chosen in various ways, as described in Section 2.4. The essential feature of the present method is that, outboard of a certain spanwise position, which may also be chosen arbitrarily, the leading-edge shape is modified in such a way as to keep the strength of the singularity constant out to the tip. The position P_0 (*see* Fig. 2) at which the leading edge modification begins determines the final aspect ratio of the wing. Thus, for a given trailing edge sweep and initial leading edge shape, a single family of wings of varying aspect ratio may be developed by varying this position, or alternatively by keeping P_0 fixed (in the streamwise direction) and varying the initial leading-edge shape. Three such families are considered in the present paper, each of which is

*The strength of the leading-edge singularity is one of the factors which influence the magnitude of the suction peak in real flow, although this must also depend on other factors, notably the thickness distribution of the wing section near the leading edge.

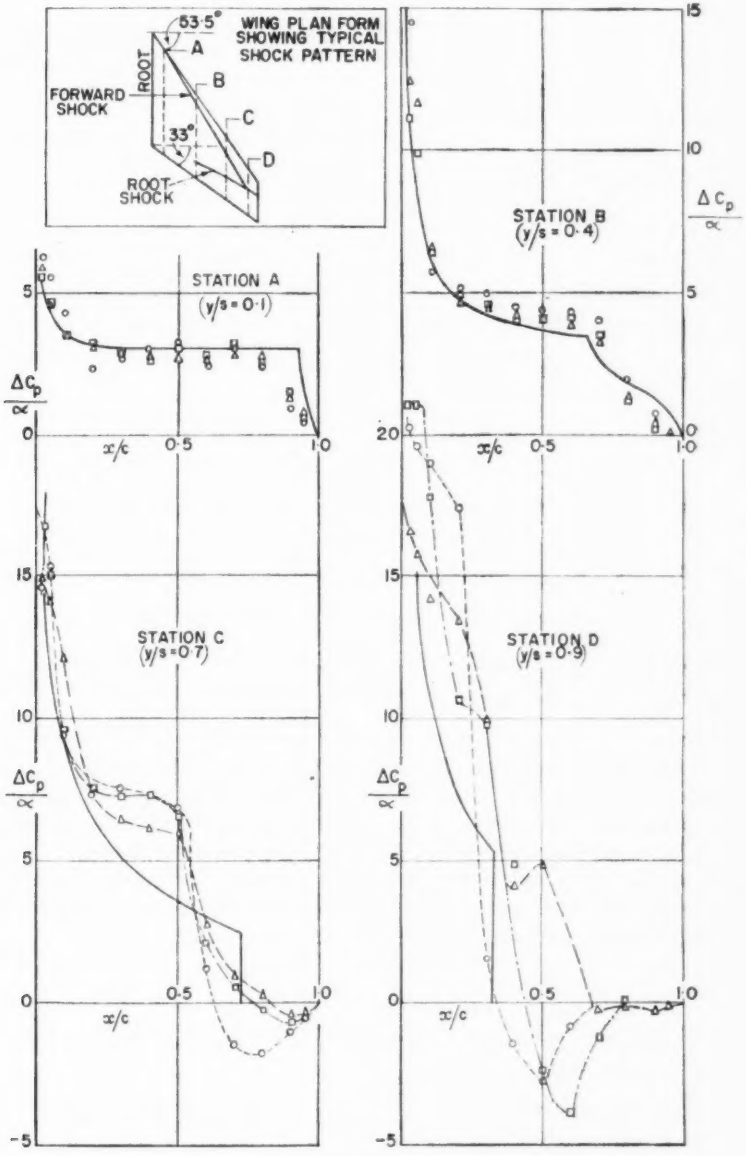

FIGURE 1. Comparison between sonic loading theory and experiment: $M = 1{\cdot}0$. Aspect ratio = 2·828. Taper ratio = 1/3. Wing section R.A.E. 102, 6% thick.

Experiment { $\alpha = 1°$ ○ ; $\alpha = 3°$ □ ; $\alpha = 5°$ △

Sonic theory ——

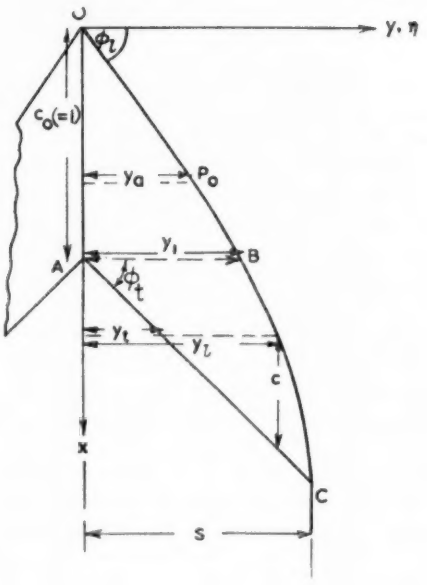

FIGURE 2. Typical wing plan form showing notation used.

believed to be of some practical interest. In all cases the method leads to a characteristic curved tip shape, as shown in Fig. 5 (p. 77).

An interesting feature that is apparent when calculations of the detailed loading are made for these wings is that, once the strength of the leading edge singularity is held constant, the shape of the chordwise loading curves also becomes almost independent of spanwise position. It follows that if the thickness distribution of such a wing is designed to give fully swept isobars at zero incidence, then this property should be retained in the tip regions under lifting conditions; and similarly for a wing, cambered and twisted to give fully swept isobars at one particular lift coefficient, under off-design conditions.

NOTATION

x, y, z	Cartesian co-ordinates, using root chord as unit of length
c	(wing chord)/(root chord)
s	(semi-span)/(root chord)
S	(wing area)/(root chord)^2
A	aspect ratio
M	Mach number
α	angle of incidence
ϕ_l	angle of sweepback of leading edge

ϕ_t angle of sweepback of trailing edge

$\xi = (x - x_l)/c$

$\eta = y \tan \phi_t$

C_p pressure coefficient

l loading coefficient $= C_p$ (lower surface) $- C_p$ (upper surface)

$k = y_t(x)/y_l(x)$

$k' = \sqrt{(1-k^2)}$

$\kappa = E(k')/K(k')$

$K(k')$ complete elliptic integral of the first kind with modulus k'

$E(k')$ complete elliptic integral of the second kind with modulus k'

$$\chi = \sin^{-1}\sqrt{\left(\frac{\eta_l^2 - \eta^2}{\eta_l^2 - \eta_t^2}\right)}$$

$H(x)$ function determined by equations (5) or (6)

σ strength of leading-edge singularity (*see* equation (7))

σ_1 constant value of σ in tip region

$m = (dx_l/d\eta)$, = (leading edge slope)/(trailing edge slope)

$G = H^2(1-k^2)$ (equation (15))

λ parameter used in Section 2.4.3.

$C_L(\eta)$ local section lift coefficient

$\overline{C_L}$ wing lift coefficient

$\Gamma = \dfrac{2sc}{S}\dfrac{C_L}{\overline{C_L}}$, spanwise loading factor

K vortex drag factor (equation (28))

C_M pitching moment coefficient about $x = 0$, based on root chord

$\bar{x}$ position of centre of pressure relative to root chord

Suffixes

l leading edge

t trailing edge

1 value at $x = 1$

0 value at P_0 (Fig. 2).

2. Details of the Design Method

2.1. Summary of Sonic Lifting-Surface Theory

The co-ordinate system and basic notation used are explained in Fig. 2. Axes Ox and Oy are taken in the usual way, with the origin O at the apex of the wing, Ox

in the streamwise direction and Oy in the spanwise direction. It is convenient to take as unit of length the root chord c_0, and to use in the spanwise direction the co-ordinate

$$\eta = y \tan \phi_t, \qquad (1)$$

where ϕ_t is the constant angle of sweep of the trailing edge; thus in the (x, η) system of co-ordinates the trailing edge has the equation

$$\eta_t = x - 1. \qquad (2)$$

If y_l and y_t are the y co-ordinates of the leading and trailing edges respectively at a given value of x, then the loading coefficient $l = \Delta C_p$ for a flat wing at incidence α at $M = 1$ is given by[2]

$$\left.\begin{aligned} \frac{l}{4\alpha} &= \frac{y_l}{\sqrt{(y_l^2 - y^2)}} \frac{dy_l}{dx} \\ \text{or} \qquad \frac{4\alpha}{l \tan \phi_t} &= \frac{\eta_l}{\sqrt{(\eta_l^2 - \eta^2)}} \frac{d\eta_l}{dx} \end{aligned}\right\} \quad \text{for} \quad 0 \leqslant x \leqslant 1, \qquad (3)$$

and by

$$\frac{l \tan \phi_t}{4\alpha} = H(x) \frac{d\eta_l}{dx} \left\{ \cot \chi \sqrt{(1 - k'^2 \sin^2 \chi)} + \right.$$
$$\left. + \int_0^{\chi} \sqrt{(1 - k'^2 \sin^2 \chi)}\, d\chi - \kappa \int_0^{\chi} \frac{d\chi}{\sqrt{(1 - k'^2 \sin^2 \chi)}} \right\} \quad \text{for} \quad x > 1, \qquad (4)$$

where $k = \dfrac{y_t(x)}{y_l(x)} = \dfrac{\eta_t(x)}{\eta_l(x)}$,

$k' = \sqrt{(1 - k^2)}$,

$\kappa = \dfrac{E(k')}{K(k')}$ (K and E being complete elliptic integrals of the first and second kinds respectively),

and $\chi = \sin^{-1} \sqrt{\left(\dfrac{\eta_l^2 - \eta^2}{\eta_l^2 - \eta_t^2} \right)}$.

The function $H(x)$ has to be determined from the fundamental integral equation

$$\int_{\eta_t}^{\eta_1} \left[H'(\eta_l) \sqrt{\left\{ \frac{(\eta^2 - \eta_t^2)}{(\eta^2 - \eta_l^2)} \right\}} - H(\eta_l) \frac{\eta_t \dfrac{d\eta_t}{d\eta_l} - \kappa \eta_l}{\sqrt{[(\eta^2 - \eta_t^2)(\eta^2 - \eta_l^2)]}} \right] d\eta_l = 0, \qquad (5)$$

where η_1 is the value of η_l at $x = 1$, and η_t is considered as a known function of η_l (*see* Ref. 2, equation (50)).

The following alternative form (Ref. 2, equation II.5) of equation (5) has proved useful for checking values of H obtained approximately by other methods:—

$$\frac{\eta}{\sqrt{(\eta^2-\eta_1^2)}}\Big(H(\eta)-1\Big)=\int_{\eta_1}^{\eta}\left[\frac{\left\{H(\eta)\,\eta_t\frac{d\eta_t}{d\eta_l}-H(\eta_l)\,\kappa\eta_l\right\}}{\sqrt{[(\eta^2-\eta_t^2)(\eta^2-\eta_l^2)]}}-\right.$$

$$\left.-\frac{\{H(\eta)-H(\eta_l)\}}{(\eta^2-\eta_l^2)^{3/2}}\,\eta_l\sqrt{(\eta^2-\eta_t^2)}\right]d\eta_l. \quad . \quad (6)$$

Here $H(\eta)$ means the value of H at the point at which the leading edge has the co-ordinates (x, η).

2.2 The Leading-Edge Singularity

Near the leading edge the elliptic integrals (the second and third terms) in equation (4) are negligible, and it may easily be shown that the loading in the chordwise direction has the singularity given by

$$\frac{l\tan\phi_t}{4\alpha}\simeq\frac{\sigma}{\sqrt{(2\xi)}} \quad \text{as} \quad \xi\to 0, \quad . \quad . \quad . \quad (7)$$

$$\text{where} \quad \xi=\frac{x-x_l(\eta)}{c(\eta)}$$

is the fraction of the local chord measured from the leading edge $x_l(\eta)$, and σ is given by

$$\left.\begin{aligned}\sigma&=\sqrt{\left(\frac{\eta}{c}\frac{d\eta}{dx_l}\right)} \quad \text{if} \quad x_l\leqslant 1\\ &=H(x_l)\sqrt{(1-k^2)}\sqrt{\left(\frac{\eta}{c}\frac{d\eta}{dx_l}\right)} \quad \text{if} \quad x_l\geqslant 1\end{aligned}\right\} \quad . \quad . \quad . \quad (8)$$

Note that $$k=\frac{x_l(\eta)-1}{\eta} \quad . \quad . \quad . \quad . \quad . \quad . \quad (9)$$

and $$c(\eta)=1+\eta-x_l(\eta). \quad . \quad . \quad . \quad . \quad . \quad (10)$$

Before proceeding further, it is of interest to calculate the strength σ of the leading-edge singularity in some simple cases.

(*a*) For an infinite swept wing of constant chord,

for which $$c=\frac{d\eta}{dx_l}=1,$$

we have

$$\left.\begin{aligned}\sigma&=\sqrt{\eta} \quad \text{for} \quad \eta\leqslant 1\\ &=H\sqrt{(1-k^2)}\,\sqrt{\eta} \quad \text{for} \quad \eta\geqslant 1\end{aligned}\right\}. \quad . \quad . \quad . \quad (11)$$

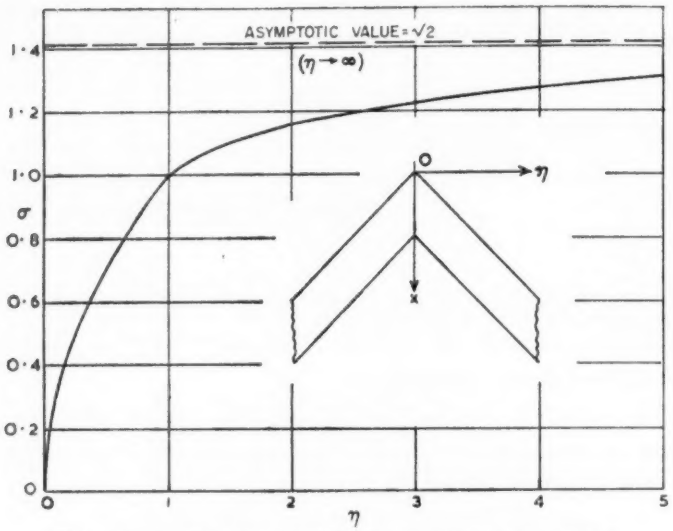

FIGURE 3. Leading edge singularity for an untapered swept wing.

where H has been calculated by Mangler[2] and Mirels[3]. These values of σ are shown plotted against η in Fig. 3. It can be seen that σ increases steadily in the spanwise direction, but approaches the asymptotic value $\sqrt{2}$ (corresponding to an "infinite yawed wing") quite slowly; for example, when $\eta = 5$ (aspect ratio $= 10 \cot \phi_t$) σ has only reached 90 per cent of the final value.

(*b*) For a highly tapered "swallow-tail" wing with leading edge $x_l = m\eta$, it is known[2, 3] that $H\sqrt{(1-k^2)} \simeq 1$ when $m \gg 1$,

so that $$\sigma \simeq \frac{1}{\sqrt{m}} \sqrt{\left(\frac{\eta}{c}\right)} \quad \text{for all values of } \eta.$$

Here $$c = 1 - (m-1)\,\eta,$$

so that $$\sigma \simeq \frac{1}{\sqrt{m}} \sqrt{\left(\frac{\eta}{1-(m-1)\,\eta}\right)}$$

$$= \frac{s \tan \phi_t}{\sqrt{(1 + s \tan \phi_t)}} \sqrt{\left[\frac{y/s}{1-(y/s)}\right]} \quad . \quad . \quad . \quad . \quad (12)$$

where $$s = \frac{1}{(m-1)\tan \phi_t} \text{ is the ratio } \frac{\text{semi-span}}{\text{root chord}}.$$

The quantity $$\sigma \frac{\sqrt{(1 + s \tan \phi_t)}}{s \tan \phi_t}$$ is plotted against y/s in Fig. 4.

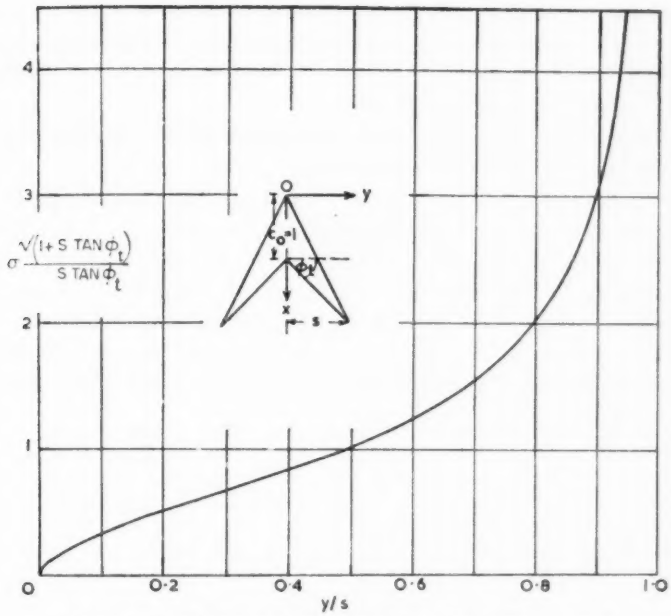

FIGURE 4. Leading edge singularity (σ) for a highly tapered wing.

The most noteworthy feature in Fig. 4 is the rapid increase in σ as the tip is approached. This is clearly an undesirable feature of such wings, and invariably leads in practice to flow separation at quite small incidences. For cropped wings of this type with straight streamwise tips, the leading-edge singularity takes exactly the same values as at the corresponding points on an equivalent fully tapered wing, so that, for wings with taper ratios greater than about $\frac{1}{2}$, the increase in σ is less serious, but there is then a loss of lift in the tip regions* and additional shock waves may appear. In the next section it will be shown how, by designing curved leading-edge shapes so that σ remains constant towards the tips, both these disadvantages may, in principle, be avoided.

2.3. Tip Shapes with Constant Leading-Edge Singularity

It is clear from the theoretical treatment summarised in Sections 2.1 and 2.2 (and also from physical considerations) that at $M=1$ the strength σ of the singularity at a particular point on the leading edge depends only on the shape of the leading edge upstream of that point. It is, therefore, possible in principle to specify σ as any reasonable function of x (or η), and to design the leading edge step by step so as to give the desired values of σ. In all the cases that will be considered here we

*Linearised theory for $M=1$ predicts zero loading in the region behind the Mach line from the tip leading edge[2]; such regions of zero (or even negative) loading are also observed experimentally[4], although their boundaries are not predicted correctly by theory.

shall take σ to be a *constant* σ_1, whenever $x \geqslant 1$ (downstream of the Mach line from the root trailing edge); this assumption appears to give sensible and useful tip shapes. Upstream of this line ($x \leqslant 1$) there are many alternative possibilities, some of which will be considered in Section 2.4.

When $\sigma = \sigma_1$ is constant for $x \geqslant 1$, equation (8) can be rewritten to give the following equation for the leading-edge shape

$$\frac{d\eta}{dx} = \frac{\sigma_1^2 (1+\eta-x)}{\eta H^2 (1-k^2)}$$

$$= \frac{\sigma_1^2}{H^2 (1+k)} ; \qquad (13)$$

here the suffix l has been dropped and $k = (x-1)/\eta$. It is convenient to use k as independent variable; then

$$\frac{d\eta}{dx} = \frac{1}{k} - \frac{(x-1)}{k^2} \frac{dk}{dx} ,$$

so that equation (13) becomes

$$(x-1) \frac{dk}{dx} = k - \frac{\sigma_1^2 k^2}{H^2 (1+k)} . \qquad (14)$$

If we write $$H^2 (1-k^2) = G \qquad (15)$$

(the reason for this will appear later), equation (15) can be arranged in the form

$$\frac{dx}{x-1} = dk \left[\frac{1}{k} + \frac{\sigma_1^2 (1-k)}{G - \sigma_1^2 k (1-k)} \right] ,$$

which can be integrated to give

$$\eta = \frac{x-1}{k} = \eta_1 \exp \left\{ \sigma_1^2 \int_1^k \frac{(1-k)\, dk}{G - \sigma_1^2 k (1-k)} \right\} , \qquad (16)$$

where η_1 is the value of η when $x = 1$.

If G (or H) were known as a function of k, equation (16) would provide an explicit solution to the problem. In fact, H is not, of course, known explicitly, but depends on the complicated integral equation (5) (or (6)). The procedure adopted in the present paper is to obtain a suitable approximation for H and to use it in equation (16) to find a first approximation to the leading-edge shape. A better approximation to H can then be found by means of equation (6), and this could be used in (16) to improve the leading-edge shape; but in practice this has not proved

necessary (*see* Section 2.5). A suitable approximation to H is provided by Mirels (Ref. 3, Appendix D). He shows that

$$G^{1/2}=H\sqrt{(1-k^2)}=1-\int_0^k \frac{dk}{m\,(k)\log\,(4/k)}+O\left(\frac{k^3}{m}\right)+O\left(\frac{k^2}{m^2\log k}\right), \qquad (17)$$

where $m=dx/d\eta_l$ is the ratio of the trailing-edge slope to the leading-edge slope for a given value of x. The form of the terms neglected on the right-hand side indicates that equation (17) should provide an adequate approximation to H provided *either* that k is small *or* m is large. In fact Mirels[3] has shown that, for an untapered wing ($m=1$), the approximation is valid as far as $k=\frac{1}{2}$; while Mangler's results[2] indicate that equation (17) may be used for all values of k provided that m is greater than about 2. Now all the plan forms developed here have the property that m is quite large wherever k is greater than $\frac{1}{2}$, and indeed becomes infinite at the tips ($k=1$), so that it seems reasonable to use equation (17) throughout. This enables an explicit approximation to H to be found, as follows.

Using equation (13),

we have $$m=\frac{dx}{d\eta}=\frac{H^2\,(1+k)}{{\sigma_1}^2}\,.$$

Substituting this expression for m in equation (17),

we get $$H\sqrt{(1-k^2)}=1-{\sigma_1}^2\int_0^k \frac{dk}{H^2\,(1+k)\log\,(4/k)}\,. \qquad (18)$$

Writing $$H\sqrt{(1-k^2)}=z\,(k) \quad \text{(so that } G=z^2\text{)},$$

and differentiating equation (18) with respect to k,

we get $$z^2\,\frac{dz}{dk}=\frac{-{\sigma_1}^2\,(1-k)}{\log\,(4/k)}\,,$$

which may be integrated to give

$$z^3=1-3\,{\sigma_1}^2\int_0^k \frac{(1-t)\,dt}{\log\,(4/t)} \quad \text{(since } z=1 \text{ when } k=0\text{)}$$

$$=1+12\,{\sigma_1}^2\left\{\mathrm{Ei}\left(\log\frac{k}{4}\right)-4\,\mathrm{Ei}\left(2\log\frac{k}{4}\right)\right\},$$

where $$\mathrm{Ei}\,(\log x)=\int_0^x \frac{dt}{\log t}\,.$$

TABLE I
VALUES OF THE FUNCTION $G(k, \sigma_1)$

	$\sigma_1^2=0{\cdot}5$	0·6	0·7	0·8	0·9	1·0
$k=0$	1·0	1·0	1·0	1·0	1·0	1·0
0·1	0·9790	0·9748	0·9705	0·9663	0·9621	0·9578
0·2	0·9528	0·9432	0·9336	0·9239	0·9141	0·9044
0·3	0·9249	0·9096	0·8940	0·8784	0·8626	0·8467
0·4	0·8970	0·8751	0·8542	0·8323	0·8102	0·7877
0·5	0·8703	0·8432	0·8156	0·7876	0·7591	0·7300
0·6	0·8458	0·8133	0·7802	0·7463	0·7116	0·6760
0·7	0·8248	0·7875	0·7494	0·7102	0·6699	0·6284
0·8	0·8083	0·7673	0·7257	0·6816	0·6368	0·5902
0·9	0·7976	0·7540	0·7091	0·6628	0·6148	0·5649

TABLE II
LEADING EDGE SHAPES: VALUES OF y/y_1

	$\sigma_1^2=0{\cdot}5$	0·6	0·7	0·8	0·9	1·0
$k=0$	1·0	1·0	1·0	1·0	1·0	1·0
0·1	1·0503	1·0612	1·0722	1·0836	1·0952	1·1071
0·2	1·1010	1·1242	1·1487	1·1745	1·2017	1·2305
0·3	1·1509	1·1880	1·2283	1·2720	1·3197	1·3720
0·4	1·1987	1·2509	1·3089	1·3740	1·4476	1·5317
0·5	1·2428	1·3102	1·3872	1·4762	1·5807	1·7053
0·6	1·2815	1·3633	1·4589	1·5725	1·7104	1·8820
0·7	1·3129	1·4071	1·5191	1·6552	1·8248	2·0434
0·8	1·3358	1·4392	1·5636	1·7170	1·9116	2·1683
0·9	1·3495	1·4583	1·5901	1·7537	1·9631	2·2424
1·0	1·3539	1·4644	1·5985	1·7652	1·9791	2·2650

Thus we obtain finally the approximation*

$$G(k, \sigma_1) = H^2(1-k^2) = \left[1 + 12\sigma_1^2 \left\{ \mathrm{Ei}\left(\log \frac{k}{4}\right) - 4\mathrm{Ei}\left(2\log \frac{k}{4}\right)\right\}\right]^{2/3}. \quad (19)$$

The functions $G(k, \sigma_1)$ given by equation (19) are tabulated in Table I for $\sigma_1^2 = 0{\cdot}5$, 0·6, 0·7, 0·8, 0·9 and 1·0. The corresponding values of

$$\frac{\eta}{\eta_1} = \exp\left\{\sigma_1^2 \int_0^k \frac{(1-k)\,dk}{G(k, \sigma_1) - \sigma_1^2 k(1-k)}\right\} \quad \text{(equation (16))}$$

have been found by numerical integration, and are given in Table II.

When η_1 and σ_1^2 are fixed, the shape of the leading edge downstream of $x=1$ can then be found parametrically in terms of k from equation (16) together with

$$x = 1 + k\eta \quad \text{(equation (9))}.$$

*Note that this is only valid for those tip shapes for which σ is constant.

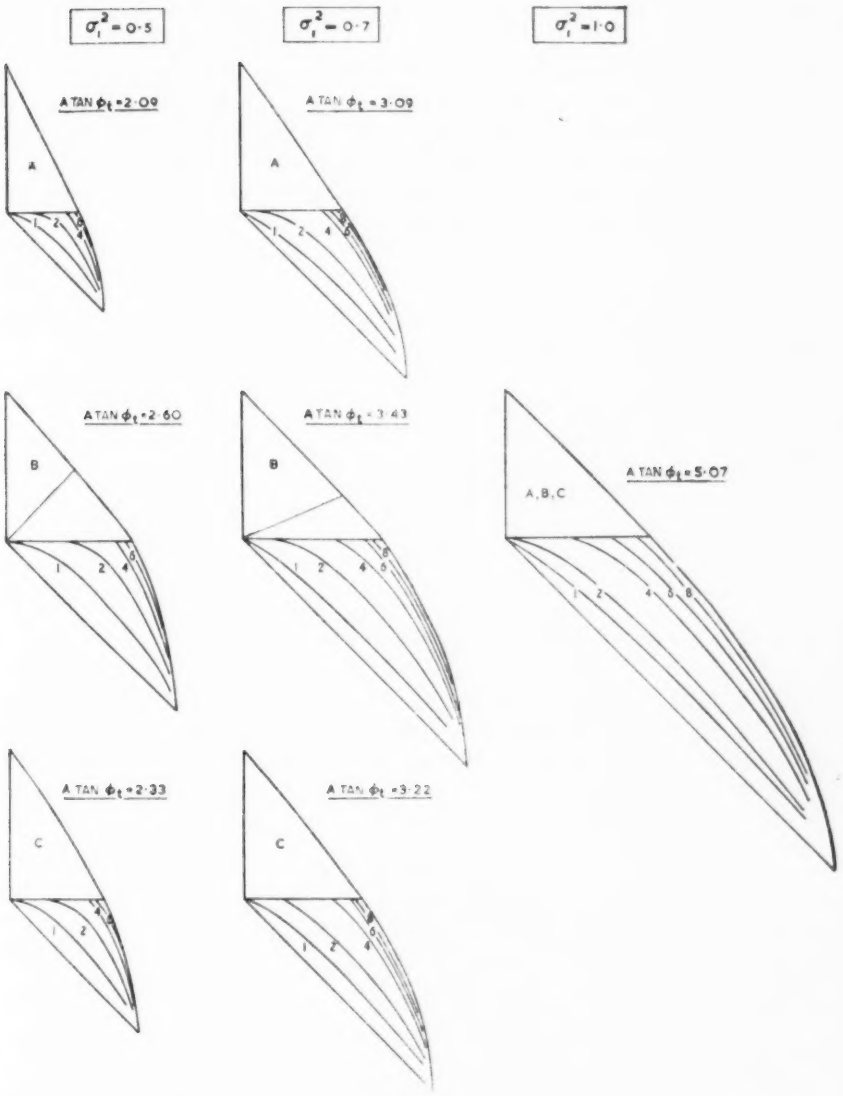

FIGURE 5. Typical wing plan forms. The numerals on the isobars give the values of $\Delta C_p/\alpha$ at $M=1.0$.

The curves thus obtained depend only on the two parameters η_1 (the value of η at $x=1$) and σ_1^2 (the value of $d\eta/dx$ at $x=1$); but for a given value of σ_1 the curves obtained by varying η_1 are geometrically similar with respect to the point (1, 0).

2.4. The Forward Part of the Leading Edge

In order to fix the plan form precisely, it is now necessary to specify the shape of the leading edge upstream of the Mach line ($x=1$) from the root trailing edge. This may of course be done in an infinite number of ways; in the present section we shall consider only three families of shapes which appear physically sensible, but other such families could easily be constructed.

2.4.1. *Type A*

The simplest course is to take the leading edge to be straight over the whole segment *OB* (Fig. 2). Its equation will then be

$$x=m_0\eta \quad (x\leqslant 1),$$

where m_0 is the ratio of the slope of the straight portion of the leading edge to that of the trailing edge. In this case we have clearly

$$\eta_1=\frac{1}{m_0}$$

and $$\sigma_1^2=\frac{1}{m_0} \quad \text{(from equation (8) or (13))};$$

with these values of η_1 and σ_1^2 the tip shape may then be found as described at the end of Section 2.3. Each value of m_0 thus defines a unique plan form (apart from the trailing edge sweepback ϕ_t, which may be chosen arbitrarily). Three typical examples corresponding to $\sigma_1^2=1/m_0=0{\cdot}5$, $0{\cdot}7$ and $1{\cdot}0$, are shown in Fig. 5(A); the ordinates of the leading edge are given in Table III (Type A). In each case ϕ_t has

TABLE III

COMPLETE LEADING EDGE SHAPES

Type A: Leading edge straight for $x\leqslant 1$ $(\eta=\sigma_1^2 x)$

	$\sigma_1^2=0{\cdot}5$		$\sigma_1^2=0{\cdot}7$		$\sigma_1^2=1{\cdot}0$	
k	x	η	x	η	x	η
0	1·0	0·5	1·0	0·7	1·0	1·0
0·1	1·0525	0·5252	1·0751	0·7505	1·1107	1·1071
0·2	1·1101	0·5505	1·1608	0·8041	1·2461	1·2305
0·3	1·1726	0·5754	1·2579	0·8598	1·4116	1·3720
0·4	1·2397	0·5994	1·3665	0·9162	1·6127	1·5317
0·5	1·3107	0·6214	1·4855	0·9711	1·8526	1·7053
0·6	1·3844	0·6407	1·6127	1·0212	2·1292	1·8820
0·7	1·4595	0·6565	1·7444	1·0634	1·4304	2·0434
0·8	1·5343	0·6679	1·8756	1·0945	2·7347	2·1683
0·9	1·6073	0·6748	2·0018	1·1131	3·0181	2·2424
1·0	1·6770	0·6770	2·1190	1·1190	3·2650	2·2650

TABLE III—*continued*

Type B: Leading edge straight for $x \leqq \sigma_1^2$ $(\eta = x)$

(The plan form for $\sigma_1^2 = 1{\cdot}0$ is identical with the corresponding plan form of Type A)

	$\sigma_1^2 = 0{\cdot}5$		$\sigma_1^2 = 0{\cdot}7$	
k	x	η	x	η
−1·0	0·5	0·5		
−0·9	0·5266	0·5256		
−0·8	0·5569	0·5539		
−0·7	0·5912	0·5840		
−0·6	0·6303	0·6162		
−0·5	0·6747	0·6506		
−0·4	0·7252	0·6871	0·7143	0·7142
−0·3	0·7823	0·7257	0·7698	0·7675
−0·2	0·8468	0·7659	0·8353	0·8238
−0·1	0·9192	0·8076	0·9115	0·8851
0	1·0	0·8499	1·0	0·9501
0·1	1·0893	0·8927	1·1019	1·0187
0·2	1·1871	0·9357	1·2183	1·0913
0·3	1·2934	0·9781	1·3501	1·1669
0·4	1·4075	1·0188	1·4974	1·2435
0·5	1·5282	1·0563	1·6590	1·3179
0·6	1·6535	1·0892	1·8316	1·3860
0·7	1·7811	1·1159	2·0103	1·4432
0·8	1·9083	1·1354	2·1818	1·4855
0·9	2·0323	1·1470	2·3596	1·5107
1·0	2·1507	1·1507	2·5187	1·5187

Type C: Leading edge curved throughout

(The plan form for $\sigma_1^2 = 1{\cdot}0$ is identical with the corresponding plan form of Type A)

	$\sigma_1^2 = 0{\cdot}5$		$\sigma_1^2 = 0{\cdot}7$	
k	x	η	x	η
	0	0	0	0
	0·1	0·0759	0·1	0·0869
	0·2	0·1499	0·2	0·1727
	0·3	0·2217	0·3	0·2571
	0·4	0·2914	0·4	0·3401
	0·5	0·3586	0·5	0·4215
	0·6	0·4232	0·6	0·5013
	0·7	0·4850	0·7	0·5792
	0·8	0·5437	0·8	0·6551
	0·9	0·5991	0·9	0·7288
0	1·0	0·6510	1·0	0·8001
0·1	1·0684	0·6838	1·0858	0·8578
0·2	1·1433	0·7167	1·1838	0·9190
0·3	1·2248	0·7492	1·2948	0·9827
0·4	1·3121	0·7803	1·4189	1·0472
0·5	1·4045	0·8091	1·5549	1·1099
0·6	1·5005	0·8342	1·7003	1·1672
0·7	1·5983	0·8547	1·8508	1·2154
0·8	1·6957	0·8696	2·0079	1·2510
0·9	1·7907	0·8785	2·1450	1·2722
1·0	1·8814	0·8814	2·2789	1·2789

TABLE IV
SUMMARY OF PLAN FORM CHARACTERISTICS

σ_1^2	$S \tan \phi_t$	$s \tan \phi_t$	$A \tan \phi_t$	$\frac{d\bar{C}_L}{d\alpha} \tan \phi_t$	$\bar{x}$	K
Type A: Leading edge straight for $x \leqslant 1{\cdot}0$						
0·5	0·876	0·677	2·094	2·605	0·830	1·009
0·7	1·622	1·119	3·088	3·392	0·966	1·013
1·0	4·040	2·265	5·079	4·353	1·360	1·047
Type B: Leading edge straight for $x \leqslant \sigma_1^2$						
0·5	2·034	1·151	2·603	3·238	0·828	1·006
0·7	2·688	1·519	3·434	3·773	1·007	1·016
1·0	4·040	2·265	5·079	4·353	1·360	1·047
Type C: Fully curved leading edge						
0·5	1·332	0·881	2·334	2·904	0·793	1·012
0·7	2·034	1·279	3·218	3·540	0·978	1·013
1·0	4·040	2·265	5·079	4·353	1·360	1·047

been taken as 45° for simplicity, but the corresponding shapes for other values of ϕ_t can be obtained at once by multiplying all lateral (y) dimensions by $\cot \phi_t$ while leaving all longitudinal (x) dimensions unchanged. For each value of m_0 it is clear that the aspect ratio A and the ratio of semi-span to root chord (s) are proportional to $\cot \phi_t$; the corresponding values of $A \tan \phi_t$ and $s \tan \phi_t$ are given in Table IV (Type A) and are shown in Fig. 6 (Type A) plotted against $\sigma_1^2 = 1/m_0$.

2.4.2. *Type B*

A more general class of leading-edge shapes can be obtained by starting (as in Section 2.4.1) with a straight portion OP_0, $x = m_0\eta$, but now taking the point P_0 outboard of which the singularity is to be held constant to be

$$x = x_0$$

$$\eta = \frac{x_0}{m_0} = \eta_0.$$

If $x_0 < 1$ (as in all examples considered here), the shape of the curve P_0B (Fig. 2) required to keep $\sigma = \text{constant} = \sigma_1$ for $x_0 \leqslant x \leqslant 1$ may easily be found from equation (16) by setting $G = H\sqrt{(1-k^2)} \equiv 1$ (compare the two forms of equation (8)). This gives

$$\frac{\eta}{\eta_1} = \frac{1}{\sqrt{[1+\sigma_1^2(k^2-k)]}} \exp\left[\left\{\frac{\sigma_1}{\sqrt{(4-\sigma_1^2)}} \tan^{-1} \frac{k\sigma_1\sqrt{(4-\sigma_1^2)}}{2-k\sigma_1^2}\right\}\right], \qquad (20)$$

where $k = (x-1)/\eta$ as before (k is, of course, negative). The value of σ_1 may be found from equation (8), which gives

$$\sigma_1^2 = \frac{\eta_0}{m_0\{1-(m_0-1)\eta_0\}} \quad . \quad . \quad . \quad . \quad . \quad (21)$$

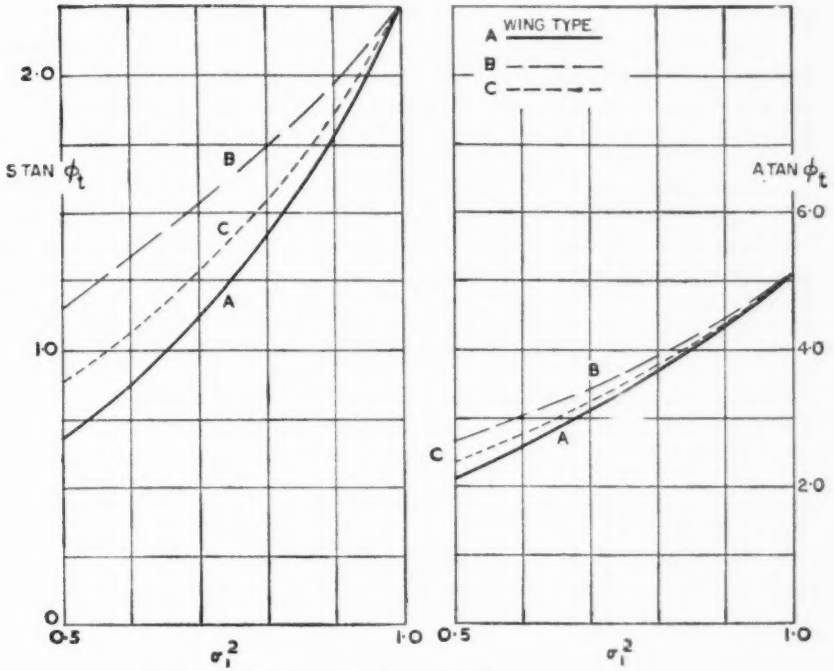

FIGURE 6. Variation of semi-span s and aspect ratio A with σ_1.

η_1 (the value of η when $x=1$) can then be found by substituting $k=k_0=(x_0-1)/\eta_0$ in equation (20) as follows:—

$$\eta_1=\eta_0\sqrt{[1+\sigma_1^2(k_0^2-k_0)]}\exp\left[\left\{-\frac{\sigma_1}{\sqrt{(4-\sigma_1^2)}}\tan^{-1}\frac{k_0\sigma_1\sqrt{(4-\sigma_1^2)}}{2-k_0\sigma_1^2}\right\}\right]. \quad (22)$$

Equations (20), (21) and (22) determine the shape of the curve P_0B ($x_0\leqslant x\leqslant 1$), and the remainder of the leading edge ($x>1$) can then be found as before.

The leading-edge shapes just described depend on two basic parameters, m_0 (the taper of the inner part of the plan form) and x_0 (the position at which the leading edge becomes curved). To provide a contrast to the plan forms of Type A described in Section 2.4.1, for which x_0 was taken as 1 and m_0 varied, we have chosen as an illustration the second family of curves for which $m_0=1$ (*i.e.* there is no initial taper) and x_0 is varied. In this case $x_0=\eta_0=\sigma_1^2$. Three examples, having $x_0=0{\cdot}5$, $0{\cdot}7$ and $1{\cdot}0$, are given in Table III and shown in Fig. 5 (Type B); the last example is identical with the corresponding case in Section 2.4.1 (Type A). The corresponding values of $A\tan\phi_t$ and $s\tan\phi_t$ are given in Table IV and plotted against σ_1^2 ($=x_0$) in Fig. 6.

2.4.3. *Type C*

The plan forms described in Sections 2.4.1 (Type A) and 2.4.2 (Type B) may suffer from certain disadvantages when $A \tan \phi_t$ is small. For plan forms of Type A this implies that the initial taper parameter m_0 is large, and it is then found (*see* Section 3.2) that the local section lift coefficients increase rather rapidly over the inner part of the span. Plan forms of Type B are satisfactory in this respect, but may prove undesirable from the structural point of view since they have no initial taper, while the rapid increase of leading-edge curvature at P_0 may have aerodynamic disadvantages. These difficulties could be overcome by a proper choice of m_0 and x_0 (cf. Section 2.4.2) but, as an alternative, it is possible to prescribe the variation of σ over the whole of the segment OB in such a way that it increases less rapidly in the spanwise direction than for the simple tapered plan forms of Type A (Section 2.4.1); this leads to leading-edge shapes which are curved over the entire span.

The simplest expression for σ which has the required property is

$$\sigma^2 = \lambda\eta \quad (x \leqslant 1). \qquad (23)$$

Equation (8) then becomes

$$\frac{d\eta}{dx} = \lambda\,(1 + \eta - x), \qquad (24)$$

which has the solution

$$\eta = x - \frac{(1-\lambda)}{\lambda}\,(e^{\lambda x} - 1). \qquad (25)$$

This gives

$$\eta_1 = \frac{1}{\lambda}\{1 - (1-\lambda)\,e^{\lambda}\} \qquad (26)$$

and

$$\sigma_1^2 = \lambda\eta_1 = 1 - (1-\lambda)\,e^{\lambda} \qquad (27)$$

In this way a third one-parameter family of leading-edge shapes (Type C) has been developed. Three examples, corresponding again to $\sigma_1^2 = 0{\cdot}5$, $0{\cdot}7$ and $1{\cdot}0$, are given in Table III and shown in Fig. 5(C); the plan form with $\sigma_1^2 = \lambda = 1$ is again identical with the corresponding plan form of Type A (Section 2.4.1) or Type B (Section 2.4.2). The values of $A \tan \phi_t$ and $s \tan \phi_t$ are given in Table IV and plotted against σ_1^2 in Fig. 6.

2.5. Higher Approximations to the Function $H(x)$

It will be recalled that the leading-edge shapes developed in Sections 2.3 and 2.4 were based on an approximation (17) or (19) for the function H. When a plan form has been obtained in this way it is important to verify that the chosen approximation is in fact a good one and, if necessary, to modify the shape accordingly. This can be done by substituting the first approximation to H into the

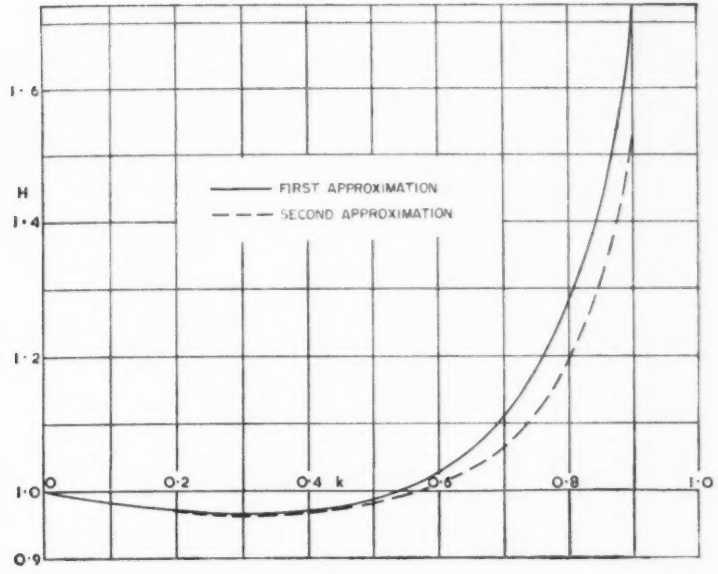

FIGURE 7. Approximations to $H(k)$ for wing with $\sigma_1 = 1$.

right-hand side of equation (6); the left-hand side will then give the required second approximation to H. Only one case has in fact been investigated in this way, namely the plan form having $m_0 = \sigma_1^2 = 1$. The results are shown in Fig. 7, in which the first approximation (19) to H and the second approximation obtained by numerical integration of equation (6) are plotted against the parameter k. The agreement between the two approximations is in general very good. The first approximation appears to overestimate the value of H; as expected, the difference between the two increases as k approaches unity (towards the wing tips), but it is less than 5 per cent when $k = 0{\cdot}7$ ($y/s = 0{\cdot}90$) and even when $k = 0{\cdot}9$ ($y/s = 0{\cdot}99$) it is only 13 per cent (of the second approximation). The actual errors in H should be less than these figures, since successive approximations will probably oscillate about the true value.

In view of the fact that linearised potential theory is inevitably liable to error (due largely to viscous effects) in the immediate neighbourhood of the tips of sweptback wings, it is felt that the accuracy obtained with the present approximation should be adequate for the purpose required. In addition, for plan forms of smaller aspect ratio, for which $\sigma_1 < 1$, the approximation should be still better, because the mean taper is greater and the terms neglected on the right-hand side of equation (17) will therefore, in general, be smaller.

3. Wing Loading Distributions at $M = 1$

This section reviews the most important theoretical characteristics of the wings designed according to the methods of Sections 2.3 and 2.4.

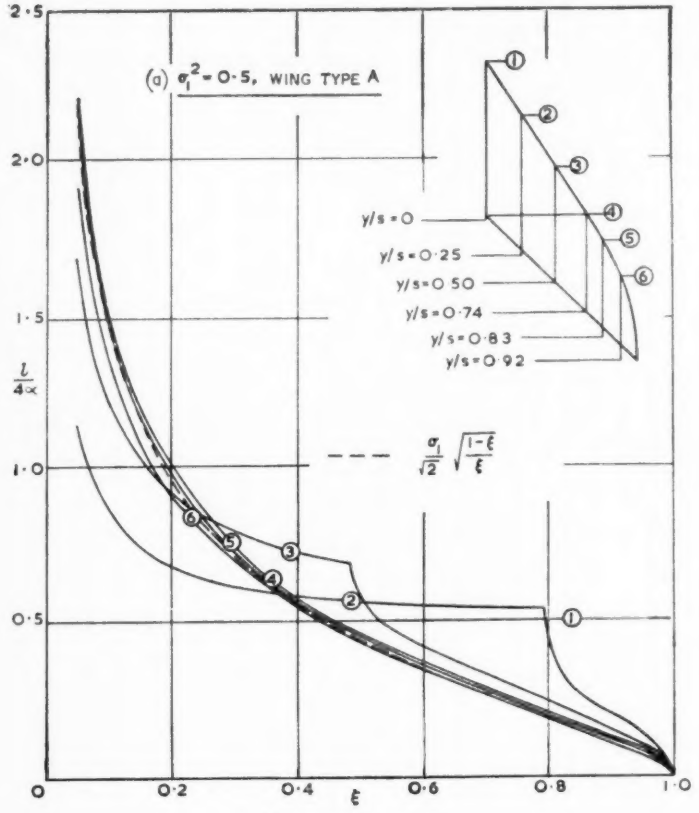

(*a*) Type A, $\sigma_1^2 = \frac{1}{2}$.

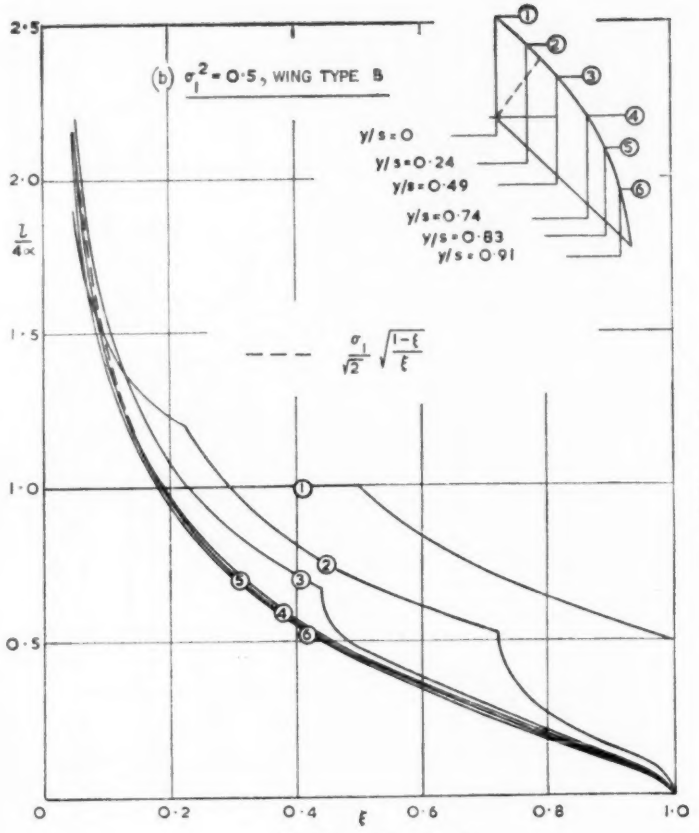

(*b*) Type B, $\sigma_1^2 = \frac{1}{2}$.

FIGURE 8. Chordwise loading curves.

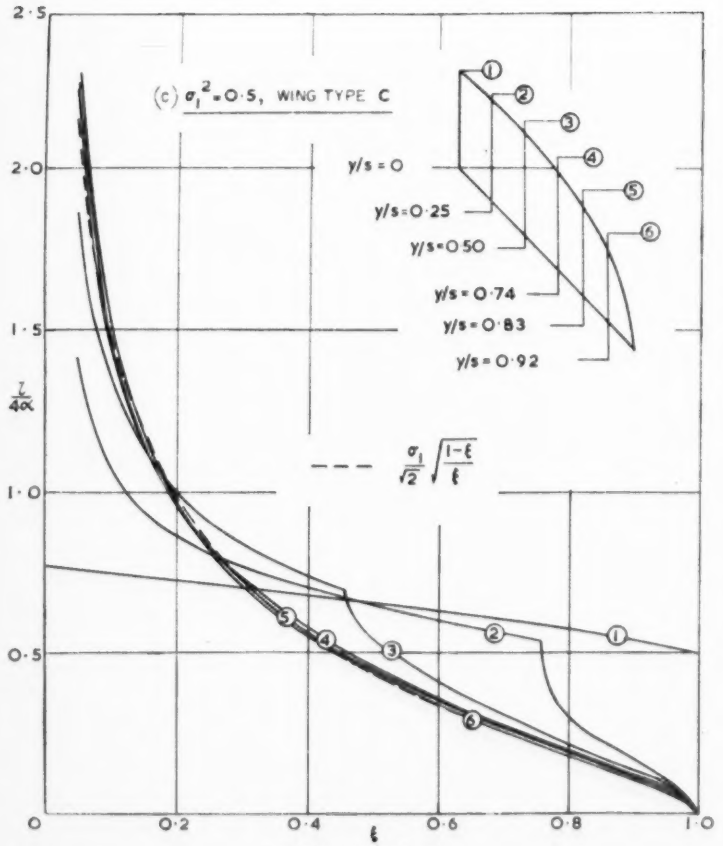

(c) Type C, $\sigma_1^2 = \frac{1}{2}$.

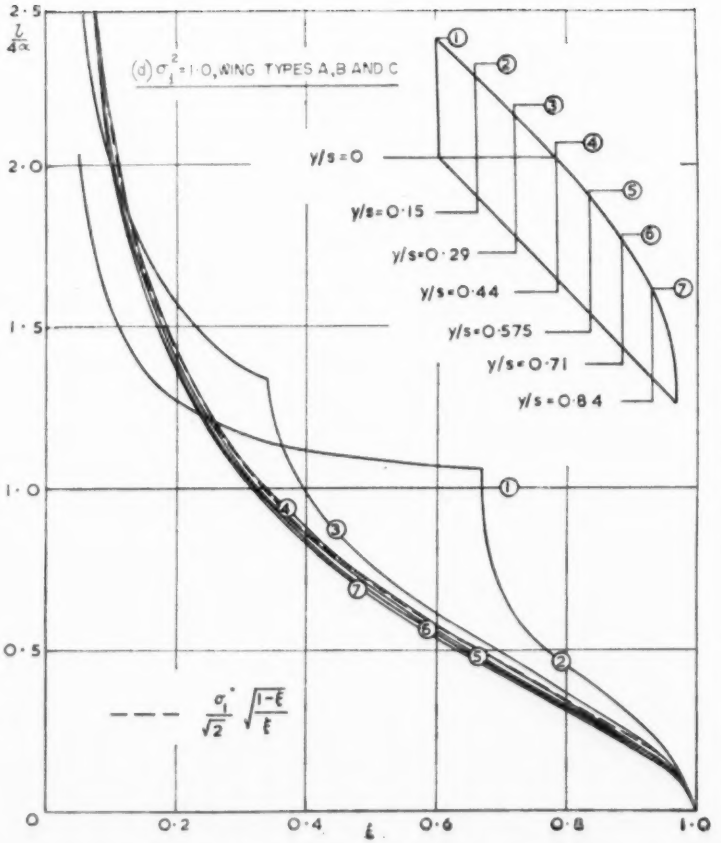

(d) Types A, B and C, $\sigma_1^2 = 1$.

FIGURE 8. Chordwise loading curves.

3.1. Chordwise Loading Curves

For a plane wing of given plan form, the wing loading coefficient l (the difference between the pressure coefficients on the upper and lower surfaces) can be found at any point by means of equations (3) (for $x < 1$) and (4) (for $x > 1$). For plan forms conforming to the design method of Section 2.3, the "unknown" function H in equation (4) has been shown to be given with sufficient accuracy by equation (19); H depends only on k, the ratio of the ordinate of the trailing edge to that of the leading edge at the particular value of x under consideration, and on the parameter σ_1, which represents the strength of the leading-edge singularity and is a constant for any one of these plan forms.

The loading distribution at several spanwise stations has been calculated in this way for all the examples mentioned in the previous section. Some results are shown in Fig. 8, which gives the chordwise loading curves for the three wings (Types A, B and C) having $\sigma_1^2 = \frac{1}{2}$ and for the wing with $\sigma_1 = 1$. The most noteworthy feature of all these results is that in the tip region (outboard of the station $\eta = \eta_1$), the chordwise load distribution, when plotted against $\xi = (x - x_l)/c$, is almost independent of spanwise position. This phenomenon could in fact have been anticipated; it is known (*see* Ref. 1) that, for plane wings in supersonic flow, the load distribution outboard of the station at which the Mach line from the root trailing edge crosses the leading edge is similar to the "flat-plate" loading $l \propto \sqrt{[(1-\xi)/\xi]}$ (cf. Fig. 8) and can be obtained approximately from it provided that the factor of proportionality is known. This factor clearly depends only on the strength σ of the inverse square root singularity at the leading edge so that, if σ is held constant, then the loading curves will not alter appreciably across the span. Wings designed in this way should thus possess the desirable feature that the loading remains constant as the tip is approached along lines of constant chordwise position; this is illustrated in Fig. 5 which shows the lines of constant loading for all the plan forms downstream of the line $x = 1$.

3.2. Spanwise Variation of Local Lift Coefficient

A similar feature is present in the curves of local lift coefficient against spanwise position, shown in Fig. 9. In all the examples considered, the lift coefficient is nearly constant over the outer half of the wing span; in most cases there is in fact a very small decrease in C_L as the tip is approached. There is, however, a noticeable difference in the behaviour of the three types of plan form over the inner part of the span. The wings which have straight tapered leading edges for $x \leqslant 1$ (Type A, Section 2.4.1) show an appreciable *increase* in C_L in the spanwise direction, and for the smaller values of σ_1^2 (or aspect ratio), when the initial taper is large, this increase is sufficiently marked to form an undesirable feature unless other steps are taken to counteract it. The wings which are initially untapered (Type B, Section 2.4.2), on the other hand, all show a definite *decrease* in C_L (after a very small initial increase), the overall variation in C_L is less than for a corresponding wing of Type A. The third type of plan form (Type C, Section 2.4.3), which has a completely curved leading edge and is, in all respects, intermediate between Types A and B, turns out

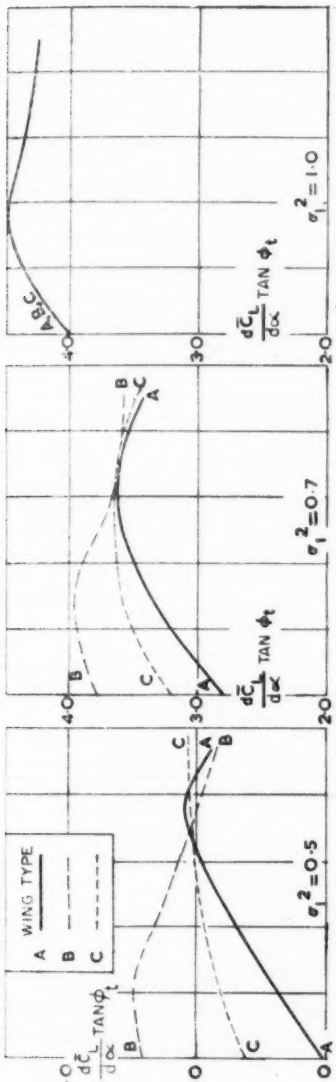

FIGURE 9. Spanwise variation of local lift coefficient.

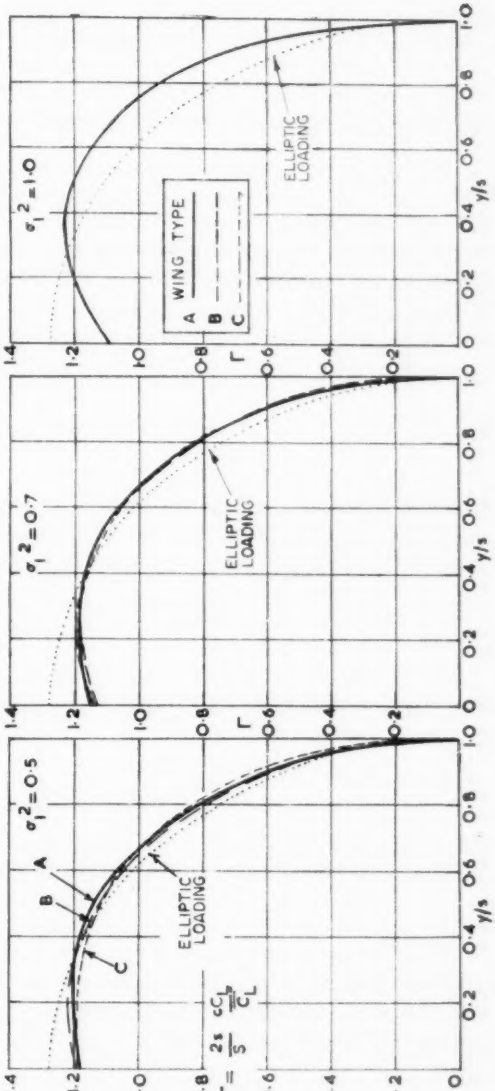

FIGURE 10. Spanwise loading curves.

to be quite a good approximation to a "constant C_L" plan form (cf. Brebner[3]); the overall variation in C_L is in no case greater than ± 5 per cent of the mean value.

3.3. Spanwise Loading and Induced Drag

The corresponding spanwise loading curves are shown in Fig. 10, in which the ratio $\Gamma = (2sc/S)\ (C_L/\overline{C}_L)$ (where $\overline{C}_L$ is the overall lift coefficient) is plotted against spanwise position y/s. It can be seen that the shape of the loading curve depends very little on the type of plan form chosen. For the smaller aspect ratios (with $\sigma_1^2 = \frac{1}{2}$) the loading is nearly elliptic, and even for the highest aspect ratio considered ($A \tan \phi_t = 5{\cdot}08$), where the loading at the root is about 12 per cent less than its maximum value, the effect on the vortex drag is not serious. This can be seen from Fig. 11, where the values of the vortex drag factor K, defined by

$$\frac{C_{D_V}}{\overline{C}_L^2} = \frac{K}{\pi A} \quad . \quad . \quad . \quad . \quad . \quad . \quad . \quad (28)$$

are plotted against $A \tan \phi_t$ for all the examples considered. These factors have been calculated from the loading curves by the standard method of Fournier analysis. The results show a certain amount of scatter, presumably due to errors in the numerical

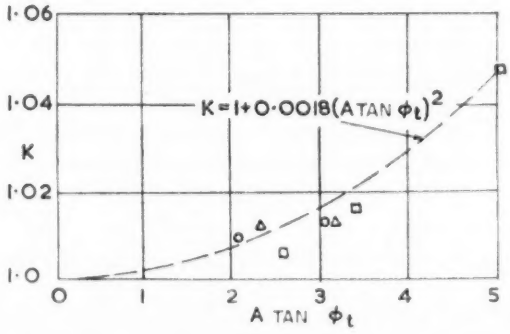

FIGURE 11. Vortex drag factors.

evaluation of the local lift coefficients, but the resulting errors in K should not exceed $\frac{1}{2}$ per cent. Within this accuracy there is no significant difference between the three types of plan form, and all the results may be approximated by the common formula

$$K = 1 + 0{\cdot}0018\,(A \tan \phi_t)^2. \quad . \quad . \quad . \quad . \quad (29)$$

Thus, over a wide range of aspect ratios of practical interest ($0 \leqslant A \tan \phi_t \leqslant 5$), the vortex drag factor does not exceed 1·05. It seems therefore that all the plan forms developed here are good approximations to theoretical "minimum vortex drag" plan forms, particularly for the smaller values of $A \tan \phi_t$, and it would seem pointless to seek any closer approximations to this ideal. A much more important question is, whether these low values of K would be obtained in practice. This is a

point which can only be settled by experiment, but it seems probable that wings which are designed, either by choice of plan form or other methods, to have constant pressure along lines of constant chordwise position will be more satisfactory in this respect than more conventional sweptback wings, where the high suction peaks near the wing tips are a major factor in causing early boundary layer thickening and separation in the tip regions.

3.4. Overall Lift and Centre of Pressure

The overall lift coefficient C_L may be obtained either by numerical integration of the spanwise loading curves or, more accurately, in the following way.

Mangler[2] has shown that the integral of the local loading coefficient l over a strip in the spanwise direction is

$$\int_{-y_t}^{y_t} l\,dy = 4\pi\alpha H y_t \frac{dy_t}{dx}(1-\kappa) \quad . \quad . \quad . \quad . \quad (30)$$

(note that $H(1-\kappa) \equiv 1$ for $x \leqslant 1$).

Hence
$$\frac{d\bar{C}_L}{d\alpha} = \frac{\pi A}{s^2}\int_0^s H(1-\kappa)\,y\,dy \quad . \quad . \quad . \quad . \quad . \quad (31)$$

or
$$\tan\phi_t \frac{d\bar{C}_L}{d\alpha} = \frac{\pi A}{s^2 \tan\phi_t}\left[\tfrac{1}{2}\eta_1^2 + \int_0^1 H(1-\kappa)\,\eta_t \frac{d\eta_t}{dk}\,dk\right] \quad . \quad . \quad (32)$$

This can be written in the form

$$\frac{d\bar{C}_L}{d\alpha} = \tfrac{1}{2}\pi A\left(\frac{y_1}{s}\right)^2\left[1 + 2\sigma_1^2\int_0^1 H(1-\kappa)\left(\frac{\eta_t}{\eta_1}\right)^2 \frac{(1-k)}{G-\sigma_1^2 k(1-k)}\,dk\right], \quad (33)$$

where η_t/η_1 is given by equation (16) or Table II. Since both η_t/η_1 and s/y_1 depend only on σ_1, it follows that $(d\bar{C}_L/d\alpha)/(\frac{1}{2}\pi A)$ is also a function of σ_1 only. Further, for any wing of a given type, σ_1 determines the value of $A\tan\phi_t$, so that $(dC_L/d\alpha)\tan\phi_t$ is a function of $A\tan\phi_t$, as indeed could be deduced from similarity considerations.

The values of $(dC_L/d\alpha)\tan\phi_t$ are given in Table IV and are plotted against $A\tan\phi_t$ in Fig. 12, while the common values of $(d\bar{C}_L/d\alpha)/(\frac{1}{2}\pi A)$ are plotted against σ_1 in Fig. 13. In both these figures the left hand (small aspect ratio) portions of the curves have been estimated in the following way. In the limit as σ_1^2 (or $A\tan\phi_t$) approaches zero, it may be shown that the integral in equation (33) approaches the value

$$\int_0^1 (1-K)\sqrt{\left(\frac{1-k}{1+k}\right)}\,dk \simeq 0{\cdot}30.$$

to be quite a good approximation to a "constant C_L" plan form (cf. Brebner[5]); the overall variation in C_L is in no case greater than ± 5 per cent of the mean value.

3.3. Spanwise Loading and Induced Drag

The corresponding spanwise loading curves are shown in Fig. 10, in which the ratio $\Gamma = (2sc/S)(C_L/\overline{C}_L)$ (where $\overline{C}_L$ is the overall lift coefficient) is plotted against spanwise position y/s. It can be seen that the shape of the loading curve depends very little on the type of plan form chosen. For the smaller aspect ratios (with $\sigma_1^2 = \frac{1}{2}$) the loading is nearly elliptic, and even for the highest aspect ratio considered ($A \tan \phi_t = 5{\cdot}08$), where the loading at the root is about 12 per cent less than its maximum value, the effect on the vortex drag is not serious. This can be seen from Fig. 11, where the values of the vortex drag factor K, defined by

$$\frac{C_{D_V}}{\overline{C}_L^2} = \frac{K}{\pi A} \quad . \quad . \quad . \quad . \quad . \quad . \quad . \quad (28)$$

are plotted against $A \tan \phi_t$ for all the examples considered. These factors have been calculated from the loading curves by the standard method of Fournier analysis. The results show a certain amount of scatter, presumably due to errors in the numerical

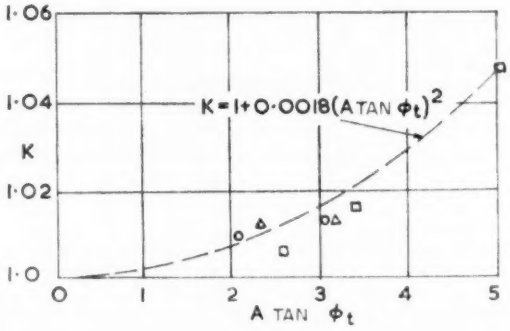

FIGURE 11. Vortex drag factors.

evaluation of the local lift coefficients, but the resulting errors in K should not exceed $\frac{1}{2}$ per cent. Within this accuracy there is no significant difference between the three types of plan form, and all the results may be approximated by the common formula

$$K = 1 + 0{\cdot}0018 (A \tan \phi_t)^2. \quad . \quad . \quad . \quad . \quad (29)$$

Thus, over a wide range of aspect ratios of practical interest ($0 \leq A \tan \phi_t \leq 5$), the vortex drag factor does not exceed 1·05. It seems therefore that all the plan forms developed here are good approximations to theoretical "minimum vortex drag" plan forms, particularly for the smaller values of $A \tan \phi_t$, and it would seem pointless to seek any closer approximations to this ideal. A much more important question is, whether these low values of K would be obtained in practice. This is a

point which can only be settled by experiment, but it seems probable that wings which are designed, either by choice of plan form or other methods, to have constant pressure along lines of constant chordwise position will be more satisfactory in this respect than more conventional sweptback wings, where the high suction peaks near the wing tips are a major factor in causing early boundary layer thickening and separation in the tip regions.

3.4. Overall Lift and Centre of Pressure

The overall lift coefficient C_L may be obtained either by numerical integration of the spanwise loading curves or, more accurately, in the following way.

Mangler[2] has shown that the integral of the local loading coefficient l over a strip in the spanwise direction is

$$\int_{-y_t}^{y_t} l\,dy = 4\pi z H y_t \frac{dy_t}{dx}(1-\kappa) \quad . \quad . \quad . \quad . \quad (30)$$

(note that $H(1-\kappa) \equiv 1$ for $x \leqslant 1$).

Hence
$$\frac{d\bar{C}_L}{d\alpha} = \frac{\pi A}{s^2}\int_0^s H(1-\kappa)\, y\, dy \quad . \quad . \quad . \quad . \quad . \quad (31)$$

or
$$\tan\phi_t \frac{d\bar{C}_L}{d\alpha} = \frac{\pi A}{s^2 \tan\phi_t}\left[\tfrac{1}{2}\eta_1^2 + \int_0^1 H(1-\kappa)\,\eta_t \frac{d\eta_t}{dk}\,dk\right] \quad . \quad . \quad (32)$$

This can be written in the form

$$\frac{d\bar{C}_L}{d\alpha} = \tfrac{1}{2}\pi A\left(\frac{y_t}{s}\right)^2\left[1 + 2\sigma_1^2\int_0^1 H(1-\kappa)\left(\frac{\eta_t}{\eta_1}\right)^2 \frac{(1-k)}{G-\sigma_1^2 k(1-k)}\,dk\right], \quad (33)$$

where η_t/η_1 is given by equation (16) or Table II. Since both η_t/η_1 and s/y_1 depend only on σ_1, it follows that $(d\bar{C}_L/d\alpha)/(\frac{1}{2}\pi A)$ is also a function of σ_1 only. Further, for any wing of a given type, σ_1 determines the value of $A\tan\phi_t$, so that $(dC_L/d\alpha)\tan\phi_t$ is a function of $A\tan\phi_t$, as indeed could be deduced from similarity considerations.

The values of $(dC_L/d\alpha)\tan\phi_t$ are given in Table IV and are plotted against $A\tan\phi_t$ in Fig. 12, while the common values of $(d\bar{C}_L/d\alpha)/(\frac{1}{2}\pi A)$ are plotted against σ_1 in Fig. 13. In both these figures the left hand (small aspect ratio) portions of the curves have been estimated in the following way. In the limit as σ_1^2 (or $A\tan\phi_t$) approaches zero, it may be shown that the integral in equation (33) approaches the value

$$\int_0^1 (1-K)\sqrt{\left(\frac{1-k}{1+k}\right)}\,dk \simeq 0{\cdot}30.$$

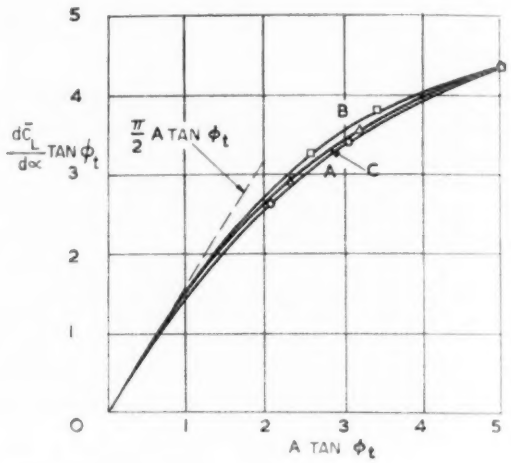

FIGURE 12. Lift curve slopes as functions of aspect ratio.

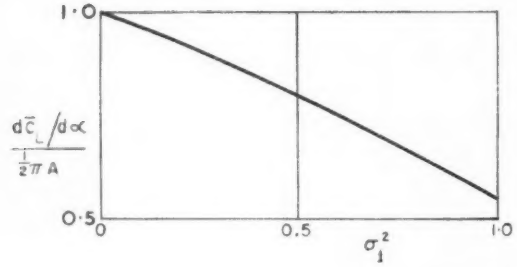

FIGURE 13. Lift curve slopes as functions of σ_1^2.

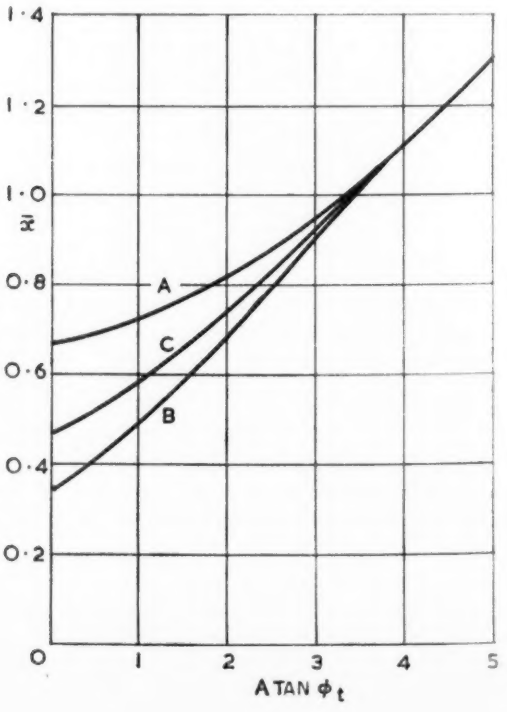

FIGURE 14. Centre of pressure positions.

Also, as σ_1^2 approaches zero, $\left(\frac{y_1}{s}\right)^2 \simeq 1-\sigma_1^2$,

so that equation (34) takes the approximate form

$$\frac{d\bar{C}_L}{d\alpha} \simeq \tfrac{1}{2}\pi A\,[1-0{\cdot}40\sigma_1^2 + O(\sigma_1^4)]. \quad . \quad . \quad . \quad (34)$$

The relationship between σ_1^2 and the aspect ratio A, when both are small, may be found by consideration of the limiting shapes taken by the three types of plan form. These are, respectively, a standard delta (Type A), for which

$$A\tan\phi_t \simeq 4\sigma_1^2, \quad . \quad . \quad . \quad . \quad . \quad . \quad (35)$$

a half ellipse (Type B), for which

$$A\tan\phi_t \simeq \frac{8}{\pi}\sigma_1, \quad . \quad . \quad . \quad . \quad . \quad . \quad (36)$$

and a parabolic "Gothic" delta (Type C), for which

$$A\tan\phi_t \simeq \frac{3}{\sqrt{2}}\sigma_1. \quad . \quad . \quad . \quad . \quad . \quad . \quad (37)$$

Substituting these results into equation (34), we obtain the following approximations, when $A\tan\phi_t$ is small, for the lift curve slopes of the three types of wings:—

Type A: $$\frac{d\bar{C}_L}{d\alpha} \simeq \tfrac{1}{2}\pi A\,(1-0{\cdot}10\,A\tan\phi_t) \quad . \quad . \quad . \quad (38)$$

Type B: $$\frac{d\bar{C}_L}{d\alpha} \simeq \tfrac{1}{2}\pi A\,(1-0{\cdot}062\,A^2\tan^2\phi_t) \quad . \quad . \quad (39)$$

Type C: $$\frac{d\bar{C}_L}{d\alpha} \simeq \tfrac{1}{2}\pi A\,(1-0{\cdot}067\,A^2\tan^2\phi_t) \quad . \quad . \quad . \quad (40)$$

These expressions appear to be valid for $A\tan\phi_t < 1$.

The position of the *centre of pressure* can be found in a similar way. Measuring the pitching moment about the apex ($x=0$) and taking the *root* chord as the standard length, we have

$$-\frac{dC_M}{d\alpha} = \frac{\pi A}{(s\tan\phi_t)^2}\left[\int_0^{\eta_t} x_t\eta\,d\eta + \int_0^1 x_t H(1-\kappa)\,\eta_t\frac{d\eta_t}{dk}\,dk\right]. \quad . \quad (41)$$

Then $\bar{x} = -(dC_M/d\bar{C}_L)$ gives the theoretical distance of the centre of pressure (or aerodynamic centre) downstream from the apex as a fraction of the root chord. Values of $\bar{x}$ are given in Table IV and are plotted against $A\tan\phi_t$ in Fig. 14. The

values shown for $A \tan \phi_t = 0$ depend only on the limiting shapes to which the three types of plan form tend as the aspect ratio or trailing-edge sweep approaches zero. Thus for wings of Type A (standard delta) the limiting value of $\bar{x}$ is 2/3; for Type B (half ellipse) it is 1/3; and for Type C (parabolic Gothic delta) it is 7/15.

4. Discussion

The method suggested in the present paper enables a wing plan form to be designed to have any desired variation in the strength of the singularity in the load distribution along the leading edge, for a flat wing at $M = 1$. Outboard of the point at which the Mach line from the root trailing edge meets the leading edge, the load distribution in a chordwise direction is everywhere similar to a two-dimensional "flat plate" distribution, so that spanwise control of the leading-edge singularity also controls the loading behind it. In particular, when the leading-edge singularity is held constant the chordwise loading also becomes independent of spanwise position. This property has been used in the design of three families of wings, in each of which the aspect ratio is varied by altering the value of the constant singularity strength in the tip region. The three families differ chiefly in their shape and aerodynamic behaviour over the inner part of the span.

Wings of Type A (Section 2.4.1) have straight tapered leading edges up to the point ($x = 1$) at which the Mach line from the root trailing edge meets the leading edge; they show a tendency for the local lift coefficient to increase over the inner part of the span, which may be undesirable if it becomes too large, as is the case when the initial taper is high and the aspect ratio (or more precisely $A \tan \phi_t$) is low. Wings of Type B (Section 2.4.2) are initially untapered, and the leading-edge singularity is held constant from a point P_0 that is farther forward than for Type A. As a result, the load distribution is more favourable and in particular the local lift coefficient decreases slightly over most of the span but, for the smaller aspect ratios, the plan forms show a marked change in leading-edge curvature at P_0, and this may be undesirable at low speeds and high incidences because of the tendency for a vortex to form at P_0. Wings of Type C (Section 2.4.3), which have fully curved leading edges, are in every sense intermediate between those of Types A and B and may be preferable in some respects, apart from the additional geometrical complication of the plan form shape.

The differences noted between the three types of plan form are only significant when the aspect ratios are small, and in fact they disappear altogether in the case of the highest aspect ratio here considered ($A \tan \phi_t = 5{\cdot}08$). In Section 2.4.2 a more general type of plan form, combining the properties of Types A and B, was also discussed, though not investigated in detail. Here the leading edge is initially straight and tapered (as for Type A), while the singularity is held constant from an arbitrary point P_0 (as for Type B); such a plan form might be useful in a case where one of the simpler types was found unsuitable.

All the calculations described here have been for plane wings alone. The question naturally arises: What will be the effect of mounting these wings on a fuselage? When the fuselage is slender and of circular cross section, Mirels[3] has

shown how to find the interference effects by means of a Joukowski transformation in the cross-flow planes; this reduces the problem to that of calculating the loading on a wing alone of distorted plan form. Although this is a comparatively straightforward matter, it is not possible to use any of the results of the present paper directly; but it is clear that, if the fuselage radius is small compared with the wing semi-span, then the load distribution in the tip regions will not be greatly altered by the presence of the fuselage, so that the principal features of the plan forms designed here should not be seriously affected.

The entire design method is limited by the use of linearised lifting-surface theory, which neglects any interaction between thickness and incidence and ignores the effect of viscosity. Apart from these limitations there is no particular reason to suspect the use of the simplified (sonic) form of the theory, particularly if the wing design is successful in eliminating some of the shock waves which might otherwise occur. The whole matter is clearly in need of experimental verification, and a programme of tests with this object, among others, in view is in progress at the N.P.L. The wing chosen has the plan form described in Section 2.4.1, and shown in Fig. 5, having $\sigma_1^2 = 1$, $A \tan \phi_t = 5{\cdot}08$, with $\phi_t = 55°$, and will be tested with and without a fuselage over a Mach number range from 0·8 to 1·2. As well as providing a useful experimental check on the correctness of the theory and design method, these tests should also help to determine how far on either side of the design Mach number ($M = 1{\cdot}0$) it is possible to extend the basic theoretical results.

Acknowledgment

The work described in this paper was done as part of the research programme of the Aerodynamics Division, National Physical Laboratory, and is published by permission of the Director of the Laboratory.

Acknowledgments are due to Mr. S. C. Metcalf for his valuable assistance with the computational work involved.

References

1. Jones, R. T. and Cohen, Doris. Aerodynamic Components of Aircraft at High Speeds: Section A, Chapters 2 and 3. (Vol. VII of *High Speed Aerodynamics and Jet Propulsion*, edited by A. F. Donovan and H. R. Lawrence). Princeton, 1957.

2. Mangler, K. W. Calculation of the Pressure Distribution over a Wing at Sonic Speeds. R. & M. 2888, 1951.

3. Mirels, H. Aerodynamics of Slender Wings and Wing-Body Combinations having Swept Trailing Edges. N.A.C.A. T.N. 3105, 1954.

4. Hall, I. M. and Rogers, E. W. E. Experiments on a Tapered Swept-Back Wing (Warren 12) at Mach Numbers between 0·6 and 1·6. A.R.C. 22,050. To be published in the R. & M. series.

5. Brebner, G. G. The Design of Swept Wing Plan Forms to Improve Tip Stalling Characteristics. A.R.C. 17,264, July 1954.

Review

Turbulent Flows and Heat Transfer. Volume V of *High Speed Aerodynamics and Jet Propulsion*. Edited by C. C. Lin. Oxford University Press, London, 1960. 550 pp. Illustrated. £5 5s. 0d.

It is difficult to avoid the irreverent reflection, when reading this volume, that the Princeton series on *High Speed Aerodynamics and Jet Propulsion* has got slightly out of hand. One of the title pages records the toll of general editors during the 12 years since the project was begun, and some of the changes of plan are apparent from a comparison of the two lists of titles and editors of the separate volumes, one on a title page and one on the dust-jacket. The majestic comprehensiveness of the series, which must have seemed a noble and inspiring goal in 1949, now begins to look a little like a millstone, as contributions written promptly become obscelescent while waiting on slower contributors to the same volume and as the master-plan suffers more modification. Four more volumes remain to be published.

The present volume has not escaped the penalties associated with the series. It is a heterogeneous mixture of contributions on a variety of topics, with very little unity of purpose, subject matter or style; some of the articles look a little out of touch with current work, and there are some omissions which, for a book published in 1959, seem to be serious. (For instance, the important and interesting problem of generation of noise by turbulent flows—the inclusion of which would have helped to give the book contact with "high speed aerodynamics and jet propulsion"—is hardly mentioned.) Some of the contributions are useful surveys (especially useful are those that gather together and collate large numbers of experimental observations), and these undoubtedly give the book value; however, they vary considerably in scope and quality and a thorough review would need to analyse them one by one in more detail than is appropriate here. All that I propose to do is to list the titles and authors of the separate articles, and to point out to a prospective purchaser that these articles have the general character to be expected of a brief review of the named subject by the named author, that they can be read as entirely self-contained reviews, and that the whole volume does not provide a complete picture of anything in particular.

The nine sections of the book are as follows:—

A. Transition from Laminar to Turbulent Flow, by H. L. Dryden (72 pages)

B. Turbulent Flow, by G. L. Schubauer and C. M. Tchen (121 pages)

C. Statistical Theories of Turbulence, by C. C. Lin (58 pages)

D. Conduction of Heat, by M. Yachter and E. Mayer (34 pages)

E. Convective Heat Transfer and Friction in Flow of Liquids, by R. G. Deissler and R. H. Sabersky (51 pages)

F. Convective Heat Transfer in Gases, by E. R. van Driest (89 pages)

G. Cooling by Protective Fluid Films, by S. W. Yuan (61 pages)

H. Physical Basis of Thermal Radiation, by S. S. Penner (13 pages)

I. Engineering Calculations of Radiant Heat Exchange, by H. C. Hottel (39 pages)

G. K. BATCHELOR.

World Leaders
in Civil
and Military Aviation . . .

HAWKER SIDDELEY
AVIATION

HAWKER SIDDELEY AVIATION LTD

32 Duke Street St James's London SW1

BS
AERO POWER

LIFT and THRUST from ONE ENGINE— the revolutionary BS 53 turbofan

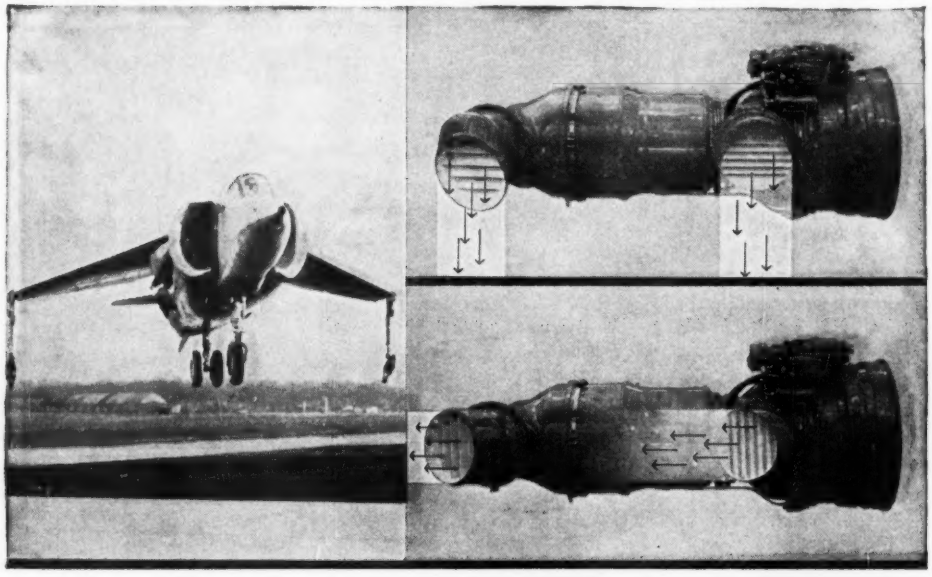

The new Bristol Siddeley BS 53 high-ratio turbofan represents a major engineering breakthrough in the field of aircraft propulsion. Because the BS 53 can be fitted with movable nozzles evenly disposed around the centre of gravity which give directional control to its total thrust, this remarkably versatile engine provides the airframe designer with *a single power source for all conditions of flight.*

VTOL, STOL and normal take-off capability in the same aircraft. Suitable for subsonic or supersonic applications.

High cold-flow ratio gives high thrust for low weight, low fuel consumption and low noise level.

Conventional installation. Operational simplicity. Independent of all fixed ground installations.

Problems of ground erosion, recirculation and ingestion of debris reduced to a minimum.

The Bristol Siddeley BS 53 has already been selected for, and is now undergoing trials in the Hawker P 1127 VTOL light strike fighter and is supported by the Mutual Weapons Development Programme for NATO.

BRISTOL SIDDELEY ENGINES LIMITED

TURBOJETS—TURBOFANS—TURBOPROPS—RAMJETS—ROCKET ENGINES—MARINE AND INDUSTRIAL GAS TURBINES—MARINE, RAIL AND INDUSTRIAL DIESEL ENGINES—PISTON ENGINES—PRECISION ENGINEERING PRODUCTS.

NOTICE TO CONTRIBUTORS

1. All communications should be addressed to the Editor, The Aeronautical Quarterly, 4 Hamilton Place, London, W.1.

2. Papers for consideration should be typewritten with double spacing and be accompanied by a summary of not more than 250-300 words. *Papers must be as short as possible*, otherwise considerable delay in publication will result, and in any case they should not be longer than twenty foolscap pages. Full descriptions and complete results of work, as written for an internal report, are not suitable for publication in *The Aeronautical Quarterly*, and such reports need to be rewritten in concise form. Only necessary equations should be included in the text; routine mathematics should be omitted or given as an Appendix to the paper. Illustrations should be reduced to a minimum. The titles of papers should be kept short—with sub-titles if necessary.

3. Only simple symbols and formulae should be typewritten. All others should be written clearly in ink. Greek letters should be indicated and a clear distinction drawn between capital and small letters. Particular attention should be paid to the use of alpha and *a*, kappa and *k*, mu and *u*, nu and *v*, eta and *n*. The letter *l* must be distinguished from the numeral 1, and the letter *O* from the zero 0.

   The use of dots, bars, and so on, over letters, or the use of dots as multiplication signs and bars for brackets should be avoided as far as possible.

   Suffixes and prefixes must be indicated clearly and complicated suffixes and prefixes should be avoided.

4. A list of *all* symbols used, both in the illustrations and text, *must* be given whether they are standard or not.

5. *Clear* diagrams or sketches must be submitted for redrawing by the Society's draughtsman.

   Photographs must be not less than half plate size and must be clear black and white glossy prints.

6. References should be given in the form:—
   WARD, G. N. Calculation of Downwash Behind a Supersonic Wing. *The Aeronautical Quarterly*, Vol. I, p. 35, May 1949.

7. The copyright of every paper printed in *The Aeronautical Quarterly* is the property of The Royal Aeronautical Society. Permission to reprint or to use any paper will not be unreasonably refused.

8. It is a condition of publication that the author shall have obtained consent where necessary to use any material in his paper which is copyright or the property of any other person or his employers.

9. Authors will be entitled to 20 reprints of their papers free of charge. This number will be shared between joint authors.

The Aeronautical Quarterly is published at the Offices of The Royal Aeronautical Society, 4 Hamilton Place, Piccadilly, London, W.1, at 15s. 0d. net for a single number to non-members and 7s. 6d. net for a single number to members of The Royal Aeronautical Society. Instructions for Contributors are given above. None of the papers must be taken as expressing the opinion of the Council of The Royal Aeronautical Society unless such is definitely stated to be the case. All communications for publication or advertisement in The Quarterly should be addressed to—The Editor, The Aeronautical Quarterly, 4 Hamilton Place, W.1.

Telephone: Grosvenor 3515. Telegraphic Address: Didaskalos, Audley, London.

THE AERONAUTICAL QUARTERLY

It is the aim of *The Aeronautical Quarterly* to attract not only original papers contributing to aeronautical science and engineering, and papers developing new or improved methods of analysis and experimental techniques, but also papers on allied sciences which have a bearing on aeronautical problems. *The Aeronautical Quarterly* is open to authors of any nationality and is not restricted to members of the Society.

Most papers can be published within nine months of receipt. Short papers, of not more than 2,000 words, are published much more quickly.

A selection of the more specialised papers read before the Society during the current lecture session will be published in *The Aeronautical Quarterly*.

VOLUME XII

Volume XII of *The Aeronautical Quarterly* will be published in four parts, in February, May, August and November 1961. The prices, *including postage and packing*, are:—

	To Members of the Society		*To Non-Members*	
	£ s. d.		£ s. d.	
Per Part	8 0	($1.15)	15 6	($2.20)
Subscription (4 parts)	1 12 0	($4.50)	3 2 0	($8.70)

PRINTED BY THE LEWES PRESS WIGHTMAN & CO. LTD., LEWES, SUSSEX, ENGLAND, AND PUBLISHED BY THE ROYAL AERONAUTICAL SOCIETY, 4 HAMILTON PLACE, LONDON W.1, ENGLAND.